



**MODELING ACOUSTIC EFFECTS ON SHEAR-COAXIAL JET FLOW
UTILIZING MOLECULAR DYNAMIC SIMULATION**

THESIS

Jermaine S. Sailsman, Captain, USAF

AFIT/GA/ENY/07-M16

**DEPARTMENT OF THE AIR FORCE
AIR UNIVERSITY**

AIR FORCE INSTITUTE OF TECHNOLOGY

Wright-Patterson Air Force Base, Ohio

APPROVED FOR PUBLIC RELEASE; DISTRIBUTION UNLIMITED

The views expressed in this thesis are those of the author and do not reflect the official policy or position of the United States Air Force, Department of Defense, or the U.S. Government.

AFIT/GA/ENY/07-M16

**MODELING ACOUSTIC EFFECTS ON SHEAR-COAXIAL JET FLOW
UTILIZING MOLECULAR DYNAMIC SIMULATION**

THESIS

Presented to the Faculty

Department of Aeronautics and Astronautics

Graduate School of Engineering and Management

Air Force Institute of Technology

Air University

Air Education and Training Command

In Partial Fulfillment of the Requirements for the
Degree of Master of Science in Astronautical Engineering

Jermaine S. Sailsman, BS, MBA

Captain, USAF

March 2007

APPROVED FOR PUBLIC RELEASE; DISTRIBUTION UNLIMITED

**MODELING ACOUSTIC EFFECTS ON SHEAR-COAXIAL JET FLOW
UTILIZING MOLECULAR DYNAMIC SIMULATION**

Jermaine S. Sailsman, BS, MBA

Captain, USAF

Approved:


Richard D. Branam, Maj, USAF (Chairman)


Dr. Robert B. Greendyke (Member)


Raymond C. Maple, Lt Col, USAF (Member)

9 Mar 07
Date

3/2/07
Date

12 Apr 07
Date

Abstract

The purpose of this research is to determine if acoustical effects on a coaxial shear injection jet flow can be modeled utilizing molecular dynamic simulation. Molecular dynamic simulations model flows as a group of interacting particles. The flow in this research was simulated using nitrogen molecules. The initial task involved achieving effective geometry for a simulated coaxial jet. The coaxial jet geometry was driven by the desire for simulations to operate in the continuum regime, which requires very low Knudsen numbers. Three outer to inner jet ratios of 0.0, 1.0, and 6.0 were examined with the inner jet velocity maintained constant at 50 m/s.

Velocity profiles in the injector need to be controlled in order to validate the continuum flow. Acoustic interference is introduced into the simulation, and mixing and density profiles provide valuable information into the how the flow is affected by the acoustic interference. Radial density profiles also provide information about the shape of the jet with and without acoustic interference as it exits the injector. The effects of acoustic interference for most cases showed good agreement with previous experimental data. Results showed good validation of the simulation and warrants more in-depth study.

*To my beautiful wife,
Thanks for being so loving, understanding, and supportive
throughout my time at AFIT.*

Acknowledgments

I would like to express the utmost appreciation to my faculty advisor, Maj. Richard Branam, for his tremendous guidance and support throughout the course of this thesis effort. This effort would not have been possible without the hard work placed into the molecular dynamics code. Your guidance has been more of a help than you may ever know. I would also like to thank my sponsor, Mr. Mitat Birkan, from AFRL Air Force Office of Scientific Research.

I would also like to thank David Doak and the other AFIT network professionals for their aid in providing great support with the computer networks vital to this research effort.

Jermaine S. Sailsman

Table of Contents

	Page
Abstract	iv
Acknowledgments	vi
Table of Contents	vii
List of Figures	ix
List of Symbols	xiii
 I. Background.....	 1
Chapter Overview	1
Problem Description	1
Objectives of Research	2
Thesis Scope	4
 II. Literature Review	 5
Chapter Overview	5
Narrow Axisymmetric Jets	5
Laminar and Turbulent Jets	7
Coaxial Jets	9
Acoustic Standing Waves	12
Nanoflows	16
 III. Methodology	 18
Chapter Overview	18
Molecular Dynamics	18
Molecular Dynamics Simulation Development.....	25
Molecular Dynamic Simulation Set-up	26
Flow Parameters	27
Equations of State	28
Reynolds and Knudsen Number	28
Coaxial Jet Sizing	29
Chamber Methodology	33
Wall Methodology	34
Acoustics Set-Up	35
Parallel Computing	37
 IV. Results.....	 39

	Page
Chapter Overview	39
Matching Theoretical Velocity Profile	39
Velocity Profile.....	42
Acoustic Model Validation.....	48
Centerline Flow Development.....	52
Radial Density Profile.....	64
V. Conclusions and Recommendations	91
Conclusions.....	91
Recommendations for Future Research.....	92
Bibliography	94
Vita.....	97

List of Figures

	Page
Figure 1. Problem Description.....	3
Figure 2. Round Jet, Free Shear Flow (Wilcox, 2006:60).....	6
Figure 3. Characterization of Coaxial Jet Flow Field (Branam,2005).....	10
Figure 4. Application of periodic boundary conditions in two dimensions for simple cubic cells. As an atom leaves the primary cell, one can be seen entering the primary cell from the opposite face. The mirror cells mimic the atom movements taking place in the primary cell. (Haile, 1992).....	24
Figure 5. Close-up image of the coaxial injector tip area, the dimensions of the injector are: $R_1 = 0.25$ mm, $R_2 = 0.79$ mm, $R_3 = 1.21$ mm and $R_4 = 1.59$ mm. (Davis and Chehroudi,2006)	30
Figure 6. Pictorial representation of the coaxial injector tip area, the dimensions of the injector are: $R_1 = 65\text{\AA}$, $R_2 = 205.4\text{\AA}$, $R_3 = 314.6\text{\AA}$	31
Figure 7. Pictorial representation of the coaxial injector tip area, the dimensions of the injector are: $R_1 = 65\text{\AA}$, $R_2 = 205.4\text{\AA}$, $R_3 = 260\text{\AA}$	32
Figure 8. Three-Zone Wall Model (Branam, 2005:46).....	35
Figure 9. Radial Velocity Profile, $r_{\text{tube}} = 20\text{\AA}$, $L/D = 1$	41
Figure 10. Radial Velocity Profile, $r_{\text{tube}} = 20\text{\AA}$, $L/D = 10$	41
Figure 11. Radial Velocity Profile, $r_{\text{tube}} = 20\text{\AA}$, $L/D = 5$	42
Figure 12. Radial Velocity Profile for $U_o = 0$ m/s, $U_i = 50$ m/s	43
Figure 13. Radial Velocity Profile for $U_o = 50$ m/s, $U_i = 50$ m/s	44
Figure 14. Radial Velocity Profile for $U_o = 300$ m/s, $U_i = 50$ m/s	45
Figure 15. Coaxial Velocity Profile for $U_o = 50$ m/s, $U_i = 50$ m/s	46
Figure 16. Coaxial Velocity Profile for $U_o = 300$ m/s, $U_i = 50$ m/s	47
Figure 17. Centerline Mixing Comparison at 0.25 ns, $U_o = 300$ m/s, $U_i = 50$ m/s.....	49
Figure 18. Centerline Mixing Comparison at 0.75 ns, $U_o = 300$ m/s, $U_i = 50$ m/s.....	50

	Page
Figure 19. Centerline Mixing Comparison at 0.25 ns, $U_o = 50$ m/s, $U_i = 50$ m/s.....	51
Figure 20. Centerline Mixing Comparison at 1.0 ns, $U_o = 50$ m/s, $U_i = 50$ m/s.....	51
Figure 21. Mixing Along Centerline , $U_o = 0$ m/s, Acoustic Free Model.....	53
Figure 22. Mixing Along Centerline , $U_o = 0$ m/s, Acoustic Interference Model	54
Figure 23. Mixing Along Centerline, Comparison of Acoustic Free Model vs. Acoustic Interference Model for $U_o = 0$ m/s.....	54
Figure 24. Mixing Along Centerline, $U_o = 50$ m/s, Acoustic Free Model.....	55
Figure 25. Mixing Along Centerline, $U_o = 50$ m/s, Acoustic Interference Model	56
Figure 26. Mixing Along Centerline, Comparison of Acoustic Free Model vs. Acoustic Interference Model for $U_o = 50$ m/s.....	56
Figure 27. Mixing Along Centerline, $U_o = 300$ m/s, Acoustic Free Model.....	58
Figure 28. Mixing Along Centerline, $U_o = 300$ m/s, Acoustic Interference Model	58
Figure 29. Mixing Along Centerline, Comparison of Acoustic Free Model vs. Acoustic Interference Model for $U_o = 300$ ms.....	59
Figure 30. Mixing Along Centerline, Comparison at 1.0 ns for Acoustic Free Model ...	60
Figure 31. Mixing Along Centerline, Comparison at 2.0 ns for Acoustic Free Model ...	61
Figure 32. Mixing Along Centerline, Comparison at 3.0 ns for Acoustic Free Model ...	61
Figure 33. Mixing Along Centerline, Comparison at 1.0 ns for Acoustic Interference Model	62
Figure 34. Mixing Along Centerline, Comparison at 2.0 ns for Acoustic Interference Model	63
Figure 35. Mixing Along Centerline, Comparison at 3.0 ns for Acoustic Interference Model	63
Figure 36. Radial Density Profile at 1.0 ns without Scaling, $U_o = 0$ m/s, Acoustic Free Model	65
Figure 37. Radial Density Profile at 1.0 ns, $U_o = 0$ m/s, Acoustic Free Model.....	66

	Page
Figure 38. Radial Density Profile at 2.0 ns, $U_o = 0$ m/s, Acoustic Free Model.....	66
Figure 39. Radial Density Profile at 3.0 ns, $U_o = 0$ m/s, Acoustic Free Model.....	67
Figure 40. Radial Density Profile at $z/d = 0$, $U_o = 0$ m/s, Acoustic Free Model.....	68
Figure 41. Radial Density Profile at $z/d = 1$, $U_o = 0$ m/s, Acoustic Free Model	68
Figure 42. Radial Density Profile at $z/d = 2$, $U_o = 0$ m/s, Acoustic Free Model	69
Figure 43. Radial Density Profile at 1.0 ns, $U_o = 0$ m/s, Acoustic Interference Model...	70
Figure 44. Radial Density Profile at 2.0 ns, $U_o = 0$ m/s, Acoustic Interference Model...	70
Figure 45. Radial Density Profile at 3.0 ns, $U_o = 0$ m/s, Acoustic Interference Model...	71
Figure 46. Radial Density Profile at $z/d=0$, $U_o = 0$ m/s, Acoustic Interference Model ...	71
Figure 47. Radial Density Profile at $z/d=3$, $U_o = 0$ m/s, Acoustic Interference Model ...	72
Figure 48. Radial Density Profile Comparison, $U_o = 0$ m/s, 1.0 ns, Acoustic Free (AF) Model and Acoustic Interference Model	73
Figure 49. Radial Density Profile Comparison, $U_o = 0$ m/s, 2.0 ns, Acoustic Free (AF) Model and Acoustic Interference Model	74
Figure 50. Radial Density Profile Comparison, $U_o = 0$ m/s, 3.0 ns, Acoustic Free (AF) Model and Acoustic Interference Model	74
Figure 51. Shadowgraph images of coaxial jet at subcritical chamber pressure (~ 1.5 MPa) and at the high outer-jet temperature (~ 190 K) corresponding to cases 1 – 4 ($U_o/U_i = \sim 1$, ~ 2.5 , ~ 5 , and ~ 6.5). The acoustic driver is off for images in the top row and on for the bottom row at ~ 3 KHz. The velocity ratio is the same for each column and increases from left to right. (Davis, 2006:94).....	75
Figure 52. Radial Density Profile, 1.0 ns, $U_o = 50$ m/s, Acoustic Free Model.....	76
Figure 53. Radial Density Profile, 1.0 ns, $U_o = 50$ m/s, Acoustic Interference Model....	77
Figure 54. Radial Density Profile, 2.0 ns, $U_o = 50$ m/s, Acoustic Interference Model....	78
Figure 55. Radial Density Profile, $z/d=0$, $U_o = 50$ m/s, Acoustic Interference Model	79
Figure 56. Radial Density Profile, $z/d=1$, $U_o = 50$ m/s, Acoustic Interference Model	79

	Page
Figure 57. Radial Density Profile, $z/d=2$, $U_o = 50$ m/s, Acoustic Interference Model....	80
Figure 58. Radial Density Profile Comparison, $U_o = 50$ m/s, 1.0 ns, Acoustic Free (AF) Model and Acoustic Interference Model	80
Figure 59. Radial Density Profile at 1.0 ns, $U_o = 300$ m/s, Acoustic Free Model.....	82
Figure 60. Radial Density Profile at 2.0 ns, $U_o = 300$ m/s, Acoustic Free Model.....	82
Figure 61. Radial Density Profile at 3.0 ns, $U_o = 300$ m/s, Acoustic Free Model.....	83
Figure 62. Radial Density Profile at $z/d=1$, $U_o=300$ m/s, Acoustic Free Case	83
Figure 63. Radial Density Profile at $z/d=2$, $U_o=300$ m/s, Acoustic Free Case	84
Figure 64. Radial Density Profile at $z/d=4$, $U_o=300$ m/s, Acoustic Free Case	84
Figure 65. Radial Density Profile at 1.0 ns, $U_o = 300$ m/s, Acoustic Interference Model	85
Figure 66. Radial Density Profile at 2.0 ns, $U_o = 300$ m/s, Acoustic Interference Model	85
Figure 67. Radial Density Profile at 3.0 ns, $U_o = 300$ m/s, Acoustic Interference Model	86
Figure 68. Radial Density Profile at $z/d=1$, $U_o=300$ m/s, Acoustic Interference Model .	86
Figure 69. Radial Density Profile at $z/d=2$, $U_o=300$ m/s, Acoustic Interference Model .	87
Figure 70. Radial Density Profile at $z/d=4$, $U_o=300$ m/s, Acoustic Interference Model .	87
Figure 71. Radial Density Comparison, $U_o = 300$ m/s, 1.0 ns, Acoustic Free (AF) Model and Acoustic Interference Model.....	88
Figure 72. Radial Density Comparison, $U_o = 300$ m/s, 2.0 ns, Acoustic Free (AF) Model and Acoustic Interference Model.....	88
Figure 73. Radial Density Comparison, $U_o = 300$ m/s, 3.0 ns, Acoustic Free (AF) Model and Acoustic Interference Model.....	89
Figure 74. Shadowgraph images of coaxial jet at nearcritical chamber pressure (~ 3.5 MPa) and at the high outer-jet temperature (~ 190 K) corresponding to cases 5–8 ($U_o/U_i = \sim 2.5, \sim 7, \sim 11$, and ~ 13.5). The acoustic driver is off for images in the top row and on for the bottom row at ~ 3 KHz. The velocity ratio increases from left to right. (Davis, 2006:96)	90

List of Symbols

Roman

$\bar{a}(t)$	Acceleration
A_i	Inner jet area
A_o	Outer jet area
b	General slip coefficient
c	Propagation speed
D_i	Inner jet diameter
D_o	Outer jet diameter
f	Frequency, force
$F(r)$	Force
J	Jet momentum
k	Wave number
L	Wavelength
L/D	Tube length/tube diameter
m	Mass of one molecule
M	Mach number, Momentum flux ratio of outer to inner jet
M_R	Momentum ratio of outer to inner jet
p	Pressure
$\vec{r}(t)$	Position
$u(r)$	Lennard-Jones potential
u_x, u_y, u_z	Mean values of molecular velocity
U, V, W	Free stream velocity components
U_i	Inner jet velocity
U_o	Outer jet velocity
U_s	Non-dimensionalized reference slip velocity
U_w	Non-dimensionalized reference wall velocity
v_s	Speed of sound in air
$\vec{v}(t)$	Velocity
x, y, z	Cartesian coordinates

Greek

α	Wave number, cell transition vector
ε	Minimum energy well
λ	Mean free path
μ	Viscosity
σ	Location of well between two particles, Surface tension
γ	Ratio of specific heats
$\sigma_x, \sigma_y, \sigma_z$	Variances of molecular velocity
ρ	Density
ν	Kinematic viscosity, small disturbance
ω	Angular frequency

MODELING ACOUSTIC EFFECTS ON SHEAR COAXIAL JET FLOW UTILIZING MOLECULAR DYNAMIC SIMULATION

I. Background

Chapter Overview

This chapter presents a brief look into the motivation for this research. A description of the problem of acoustic interference on coaxial jet flow is discussed along with some effects of the acoustic interference. The research objectives are also reviewed. These objectives will provide guidelines for a successful research effort. The results presented later in the document also reflect the objectives, and provide an answer to some of the problems presented in our problem description.

Problem Description

Jet flow has been a topic of research for decades. Coaxial jet flows adds a higher level of complexity to jet study. Adding the study of acoustic effects brings an even greater level of complexity to jet flow research. Historically, research involving coaxial jets and acoustic effects has taken place in a physical laboratory with expensive equipment and computational tools used to capture the desired relationships between a coaxial jet's core and outer flows. Similar tools can be used to measure the inherent acoustics present in operating engines, and the effects of these acoustics on the flow issuing out from the jet. This experimentation can become costly especially when the need for multiple test conditions exists. One solution points to the possibility of modeling these same jet flows using a computer simulation.

Previous research has seen molecular dynamics used to simulate supercritical fluid flow (Branam, 2005). The first challenge becomes adding a coaxial component to the simulation. Once the coaxial flow is modeled accurately, an operating geometry must be determined to minimize the computationally intensive workload. The ideal ratio of outer to inner jet area needs to be determined for the molecular dynamic simulation.

Once the molecular dynamic simulation is capable of both coaxial flow and acoustic interference, certain criteria must be met to determine if the molecular dynamic simulation may be used to accurately model the problem of acoustic interference in a coaxial injection jet.

Objectives of Research

Utilizing molecular dynamics to model the acoustic effects on a shear-coaxial jet flow requires some initial work and experimentation. The velocity profile for our inner and outer tubes needs to be controllable. The minimum ratio of tube length to tube diameter necessary to achieve the predetermined theoretical velocity profile for the simulations must be found. There is a range of tube length to diameter ratios providing the desired velocity profile but due to computational and memory restrictions, the minimum tube length to diameter ratio providing the required velocity curve is preferable.

Adding shear-coaxial jet flow and acoustic interference capabilities to the molecular dynamics tool allows this research to achieve its objectives. Shear-coaxial jet flow requires new geometry considerations and increases the needed computing power. The acoustic interference models are to be verified by examining the effects of jet mixing

with the interference turned on and off. Adding acoustic interference should increase mixing once the jet injects into the quiescent chamber.

Once the coaxial and acoustic capabilities are available, the objective becomes comparing flow fields with and without acoustic interference. Density profiles, which give insight to the shape of a jet, are examined. Jets without acoustic interference will show steeper density curves along with higher densities in the center of the jet. Once acoustic interference is added, the jet is expected to have a flatter density profile while becoming more diffuse and dissipating quicker.

The simulation explores a range of outer to inner jet velocities. The velocity profiles for the inner and outer jets will provide data that will aid in validating the flow issuing into the chamber. Figure 1 gives a graphical representation of the problem description.

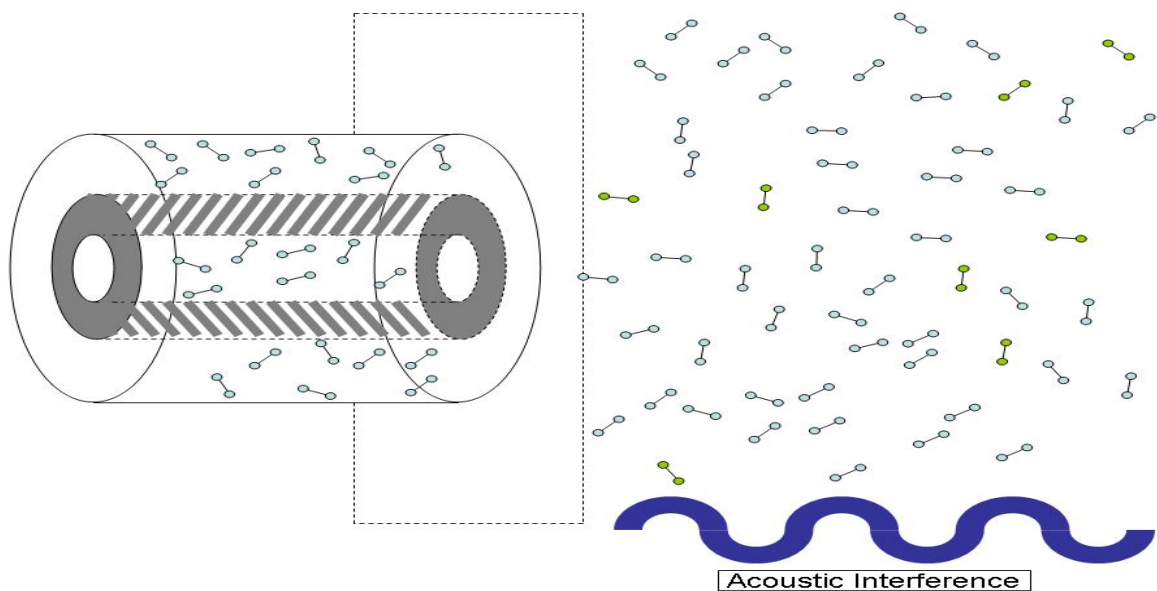


Figure 1. Problem Description

Thesis Scope

This document contains four main chapters. Chapter two presents the literature review including the theory behind the multiple disciplines taken into account for the research. The chapter looks into coaxial jet theory, including velocity and diameter differentials between the inner and outer jets. Acoustic interference is discussed as it relates to jet streams. A discussion of molecular level acoustic scaling and nanoflows is also necessary and is included in this chapter.

Chapter three covers the research methodology, discussing molecular dynamic simulation in detail, considering this technique is the backbone of the research. The chapter reviews force potential models, wall modeling, and numerical integration techniques. Techniques aiding in decreasing computation times such as parallel computing are also discussed. The method used to size the coaxial jet presents itself here as well. The chapter also looks at the various simulated cases studied for this research, such as test cases flowing with and without a chamber. The research shows comparisons for coaxial jets with varying velocity differences between the inner and outer jets. The research highlights the effects of acoustics on these cases.

Chapter four presents the results of the research while chapter five brings conclusions and recommendations for bettering and continuing the research effort.

II. Literature Review

Chapter Overview

This chapter includes a review of the many disciplines incorporated into this research effort. The literature review begins with a simple discussion of narrow axisymmetric jets followed by a discussion of laminar and turbulent jets and transition theory. Section three delves into coaxial jet theory. A coaxial flow field is broken down to increase understanding of the effects of a coaxial jet on the flow cone especially with respect to the mixing of the flow and regions of change in the flow. The effects of coaxial jet geometry on a flow is reviewed, along with previous research relating the effects of velocity differences between the inner and outer jet flow. A review of work with varied coaxial jet velocity ratios is also highlighted. Section four reviews acoustic theory and focuses mainly on plane waves. This section will also develop general building blocks of acoustics and sound wave theory equations needed to develop acoustic interference on a molecular scale. Plane waves create the acoustic interference in the molecular simulations. A brief discussion of nanoflow theory appears at the close of the chapter.

Narrow Axisymmetric Jets

If a round, narrow jet issues from a small injector with sufficient momentum, it will remain narrow and grow slowly (White, 1974:350). The jet changes longitudinally as $\partial/\partial x$ and radially as $\partial/\partial r$, the larger of the changes. Figure 2 represents the round, narrow jet issuing from an injector.

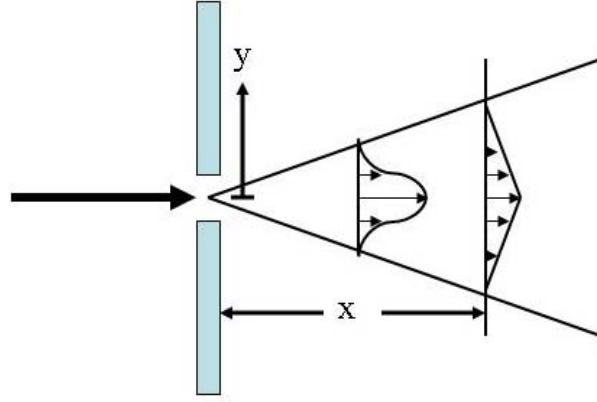


Figure 2. Round Jet, Free Shear Flow (Wilcox, 2006:60)

Squire discovered an exact solution for this case. Squire's stream function solution for small θ reduces to

$$\lim_{\theta \rightarrow 0} f(\theta) = \lim_{\theta \rightarrow 0} \frac{2 \sin^2 \theta}{1 + a - \cos \theta} = \frac{\xi^2}{1 + \xi^2 / 4} \quad \text{where } \xi^2 = \frac{2\theta^2}{a} \quad (1)$$

Equation 2 shows the boundary layer solution for the narrow jet with the origin existing at the jet exit.

$$\theta = \tan^{-1}(y/x) \ll 1 \quad (2)$$

For the reduced stream function, $\theta = y/x$ and a is a constant less than 0.05 and is directly related to the dimensionless jet momentum. The longitudinal velocity follows from the definition of the stream function (equation 3) where J is the jet momentum.

$$u(\xi) = \frac{3J}{8\pi\mu x} \left(1 + \frac{\xi^2}{4} \right)^{-2} \quad (3)$$

The term inside of the parentheses in the longitudinal velocity equation represents the shape of the jet while the jet momentum affects the jet width. This term also represents

the shape of a turbulent round jet. Equation 4 shows mass rate of flow across any section of the flow (\dot{m}) increases linearly.

$$\dot{m} = \rho \int_0^{\infty} u 2\pi y dy = 8\pi\mu x \quad (4)$$

Laminar and Turbulent Jets

Laminar flow has a very low resistance to high Re (White,1974:385). The critical Re is defined as the Re where a laminar flow becomes turbulent. This number exists on the order of 1,000 for tube flow, not a large value. Due to this low critical Re, a laminar flow is the exception to the rule and is rarely seen. Due to its low resistance to Re, a laminar flow is in essence an unstable flow, which with small disturbances moves into the turbulent regime. The same results are clearly apparent in physical experimentation (White, 1974:385-387). If laminar flow is the exception, then turbulence must exist for the majority of flows. A shear laminar jet with no wall or pressure gradients can be considered relatively unstable. Most boundary-layer flows are stable for very small disturbances but a larger disturbance drives the flow towards instability. This transition from laminar to turbulent is explained using small-disturbance stability theory (White,1974:387). Small-disturbance theory analysis begins with a set of governing equations with a known solution. A small disturbance is added to this solution. After some algebra, the small disturbance terms encapsulate the original solutions and become the only terms left. The solution is simplified by assuming that the flow is in one direction. The simplification reduces the equations to a set of ordinary homogeneous differential equations for the small variation.

Following the small-disturbance stability theory by considering the Navier-Stokes equations for two variables, the two initial equations become

$$\nabla \cdot V = 0 \quad (5)$$

$$\frac{DV}{Dt} = -\frac{1}{\rho} \nabla p + \nu \nabla^2 V \quad (6)$$

A solution for laminar flow is set as $V_o = (U, V, W) = V_o(x, t)$ and $p_o(x, t)$ and the small disturbance is defined as $v(x, t) = (\hat{u}, \hat{v}, \hat{w})$ and $\hat{p}(x, t)$. “All disturbances have a wave number α , a propagation speed c , and a frequency $\omega = \alpha c$ (White, 1974:392).” Assuming that the flow is in one-direction helps decrease the number of ordinary differential equations to one. The result is the Orr-Sommerfeld relation found in equation 7, a fourth order linear homogeneous equation which holds the key to infinitesimal laminar-flow stability (White:1974:396).

$$(U - c)(v'' - \alpha^2 v) - U''v + \frac{i\nu}{\alpha}(v'''' - 2\alpha^2 v'' + \alpha^4 v) = 0 \quad (7)$$

The boundary conditions for the Orr-Sommerfeld relationship have the small disturbances vanishing at infinity and at any walls representing a no slip condition. The boundary conditions that apply to our simulations are those for the free shear flow, which are

$$v(\pm\infty) = v'(\pm\infty) = 0 \quad (8)$$

Due to the order and type of relationship, the Orr-Sommerfeld relationship can be approached as an eigen function and eigen value problem. Orr-Sommerfeld simply aids in determining the stability of any parallel flow along a single direction which can be

found from a two-dimensional analysis for the effective basic flow $U_o(y)$ in that direction (White,1974:396).

Coaxial Jets

“There is a frequent need to realize a uniform mixture from two initially segregated streams in many practical instances (Villermaux, 1998:807).” A coaxial jet is one of the solutions to the problem of mixing two streams. Coaxial jet flow can occur in one of two ways. First, the injector may itself be three-dimensional as in a rectangular or elliptical shape. There could also be multiple injectors exhausting parallel to the main flow field operating closely enough so their mixing zones interfere (Schetz, 1980:137). The second definition of a coaxial jet is the one that is of importance for this research effort and will be the focus of the research work. The coaxial jet studied has an injector surrounded by a solid tube with another circular injector surrounding the solid tube. The coaxial jet will inject into a quiescent chamber.

The coaxial jet flow field is characterized by three zones, the potential core (PC) region, the characteristic decay (CD) region and the axisymmetric decay (AD) region. The PC region is where “the mixing initiated at the boundaries has not yet permeated through the entire flow field leaving a region of uniform velocity close to the jet exit velocity (Schetz, 1980:137).” The potential core region contains two potential cores and two distinct mixing regions. The two potential cores correspond to the inner and outer cores issuing into the flow stream. The first mixing region occurs between the boundary of the inner stream and the outer stream. The second mixing region occurs between the outer stream and the ambient atmosphere into which the stream issues. The CD region, which is the

scales of the velocity and the length are defined as $U_{ref} D_o (x - x_h)^{-1}$ and $(x - x_h)$, where x_h is the distance of the virtual origin from the nozzle exit plane. Reference velocity U_{ref} can be calculated using total jet momentum flux. For a flow ratio U_o/U_i up to 10, U_{ref} can be defined as follows, where J_T is the total jet momentum:

$$U_{ref} = \left(\frac{J_T}{\rho A_T} \right)^{\frac{1}{2}} = \left(\frac{U_o^2 A_o + U_i^2 A_i}{A_o + A_i} \right)^{\frac{1}{2}} \quad (9)$$

The mean velocity and turbulent intensity are respectively as follows:

$$\frac{U}{U_{ref}} = \frac{D_o}{x - x_o} f \left(\frac{y}{x} - x_o \right) \quad (10)$$

$$\frac{\overline{u^2}}{U_{ref}^2} = \frac{D_o^2}{(x - x_o)^2} g_1 \left(\frac{y}{x} - x_o \right) \quad (11)$$

For cases where $U_o = U_i$ or $U_o = 0$, the mean velocity and the turbulent intensity can be simplified. For U_o/U_i ranging from 0.0 to 1.0, the inner core length will be somewhat longer, possibly resulting in a lower shear between inner and outer jets. As U_o/U_i increases, the inner potential core decreases. Larger U_o/U_i values also lead to higher turbulent intensities in the initial regions of the flow (Champagne and Wygnanski, 1971:1452).

As the flow issues from the coaxial jet, changes to the mean velocity ratio do not affect the outer potential core length. The outer potential core length is in essence a constant, feeling little to no effect from changes to the inner jet velocity (Ko and Au, 1985:211-232; Au and Ko, 1987:427-443). Experimental research has shown the width of each core decreases as the flow moves downstream (Champagne and Wygnanski, 1971:1445-

1464). The ratio of annular to core area affects the pressure differential bending the jet inward or outward, in effect shortening or lengthening the inner core.

Acoustic Standing Waves

When discussing acoustics in a traditional sense, the focus moves towards treating fluid flow as a continuum using macroscopic quantities such as density, velocity and pressure as dependent variables (Danforth-Hanford, O'Connor, Long, and Anderson, 2005). A major decision must be made between two methods when choosing to simulate acoustics in a flow field. The deciding factor has been shown to be the Knudsen number (Kn), where Kn is defined as the mean free path divided by the wavelength.

$$Kn = \frac{\lambda}{L} \quad (12)$$

There are separate considerations for low versus high Kn. Sound propagation at low Kn relates to low frequencies and atmospheric conditions while sound propagation for high Kn relates to higher frequencies and more dilute gases (Danforth-Hanford, et. al, 2005). Danforth and Long (2004:1948-1955) have shown absorption and speed of sound relies heavily on Kn. The continuum model of fluid flow utilizes the Navier-Stokes or Euler equations and is a more traditional method for simulating fluid but it is not very useful for $Kn > 0.1$. The particle method, while more complex, provides a wider operating spectrum for Kn and offers the ability to work with a wider range of fluid flows. Particle methods are necessary for $Kn > 0.1$, which can occur during shockwaves, high frequencies, rarified gas or other flows (Danforth and Long, 2004:1948). Looking at acoustics in the audio spectrum, the smallest wavelength possible is approximately 2 cm (Ludwig, undated, A). A significantly smaller wavelength is needed

in order to bring the intended level of interference to our molecular simulation. A cube of air with a width approximately one thousand times smaller than the 2 cm wavelength can contain over 2×10^{11} molecules (Ludwig, undated, A). Following these assumptions, a cube with a width of approximately 200Å, which is in the realm of interest for molecular dynamic simulations, could contain over 2×10^7 molecules.

The molecular dynamic tool models the acoustic interference in the simulations in two ways. One of the methods will have the interference modeled as a pressure exerted by the gas molecules due to the collisions of these molecules against a surface. The “pressure is equal to the change in momentum caused by collisions, per unit time and per unit area (Ludwig, undated, A).” Total momentum flux results from the derivation of the momentum flux in a y-direction across the face of the cube parallel to the x-z plane.

Depending on the interaction of the acoustic pressure with the desired surface, the flow across the remaining four walls of the cube may need to be considered (most of the interference in the research simulations takes place against one plane of the chamber).

Equations 13 and 14 can be combined and divided through by ΔV to achieve equation 15 reflecting the law of conservation of momentum (Ludwig, undated, B).

$$-\frac{\partial}{\partial y} \left[\rho (\sigma^2 + u_x^2) \right] \Delta x \Delta y \Delta z \quad \left[kg - m - s^{-2} \right] \quad (13)$$

$$-\left[\frac{\partial}{\partial x} (\rho u_x u_y) + \frac{\partial}{\partial z} (\rho u_y u_z) \right] \Delta x \Delta y \Delta z \quad \left[kg - m - s^{-2} \right] \quad (14)$$

$$\frac{\partial}{\partial t} (\rho u) = -\nabla (\rho \sigma^2) - \rho u \nabla \cdot u - (u \cdot \nabla) (\rho u) \quad \left[kg - m - s^{-2} \right] \quad (15)$$

The pressure term in the preceding equations are the $\rho \sigma^2$ terms where $P = \rho \sigma^2$.

Equation 16 expresses the Euler equation, an expansion from the momentum equations.

The differential equation for pressure originates from the energy flux equations (equation 17).

$$\frac{\partial \vec{u}}{\partial t} = -\frac{1}{\rho} \nabla (\rho \sigma^2) - (\vec{u} \cdot \nabla) \vec{u} \quad [m - s^{-2}] \quad (16)$$

$$\frac{\partial (\rho \sigma^2)}{\partial t} = -\frac{7}{5} \rho \sigma^2 \nabla \cdot \vec{u} - \vec{u} \cdot \nabla (\rho \sigma^2) \quad [kg - m^{-1} - s^{-3}] \quad (17)$$

The pressure differential equations and the Euler equations can be broken into two main terms. The first is the drift velocities reflecting the first-order changes directly caused by the average molecular velocity \vec{u} . The second part can be referred to as the diffusion terms, which reflect the effects of molecular diffusion (Ludwig, undated, C). For almost all cases, the diffusion term is much larger than the drift velocity term. Therefore, the drift velocity term drops out of the Euler and pressure equations leaving the following equations (Ludwig, undated, C):

$$\frac{\partial \vec{u}}{\partial t} = -\frac{1}{\rho_o} \nabla p \quad [m - s^{-2}] \quad (18)$$

$$\frac{\partial p}{\partial t} = -\frac{7}{5} \rho_o \sigma_o^2 \nabla \cdot \vec{u} \quad [kg - m^{-1} - s^{-3}] \quad (19)$$

These approximated equations represent the acoustic equations.

The basis of acoustic interference still falls out from the simpler wave formulas. A review of the following equations aids in building towards acoustic pressure amplitude determination. The following are basic sound wave equations where f is frequency, T is the oscillatory period, and L is the wavelength.

$$\omega = 2\pi f = \frac{2\pi}{T} \quad (\text{angular frequency}) \quad (20)$$

$$k = \frac{2\pi}{L} \quad (\text{wave number}) \quad (21)$$

$$\frac{\omega}{k} = \frac{2\pi Lf}{2\pi} = Lf = v_s \quad (\text{speed of sound through medium}) \quad (22)$$

Calculating wave number and angular frequency leads into the pure sine wave equation

$$y = A \sin(kx - \omega t) \quad (23)$$

After attaining the wave attributes, the pressure amplitude of the wave is calculated using the following equation where ρ_o is the density of the medium the wave travels through.

$$p_o = \rho_o \omega v_s \mathcal{E}_o \quad (24)$$

The displacement amplitude (A) is directly determined from the specified decibel level by using equation 25 from kinetic theory and the definition of the speed of sound. In this expression, ω is the angular frequency and α is the speed of sound through the modeled medium.

$$A = \frac{P}{\rho \omega \alpha} \quad (25)$$

Quantifying the pressure amplitude of sound was necessary to create an acoustic sound wave for simulation. The pressure amplitude determines the size of the sound signal. Pressure amplitude is the measure of the size of the variation of atmospheric pressure caused by the sound, or to what level the sound pressure disturbs the surrounding quiescent air (“Decibel Scales”, undated). The units for pressure amplitude for sound are decibels. The equation for sound pressure level (SPL) is

$$L_p = 20 \log \left(\frac{P}{P_o} \right) \quad (26)$$

L_p represents the sound pressure level in dB, P represents the pressure amplitude of the sound disturbance, and P_o represents a reference pressure ($2 \times 10^{-5} \text{ N/m}^2$). It is important to note that for some of the loudest sound disturbances, air pressure varies less than 1%.

Nanoflows

Earlier, Knudsen number was defined as mean free path divided by wavelength, but Kn can also be equated to

$$Kn = \sqrt{\frac{\gamma \pi}{2}} \frac{M}{Re} \quad (27)$$

which represents a length over which very large variations of a macroscopic quantity can take place (Karniadakis, Beskok, and Aluru, 2005:51-166). For rarified gases, Kn plays a large role in the flow treatment. Kn in the ranges of 0.01 to 0.1 exhibit slip flow characteristics. Transition flow characteristics are exhibited when Kn spans the range of 0.1 to 10. The fluid can be considered a continuum flow for $Kn \leq 0.01$ (Karniadakis, Beskok, and Aluru, 2005:51-166). The molecular dynamic simulations will operate in the continuum flow regime.

Utilizing a tangential momentum flux relationship, the slip velocity is

$$u_s = \frac{1}{2} \left[u_\lambda + (1 - \sigma_v) u_\lambda + \sigma_v u_w \right] \quad (28)$$

Velocity profile boundary conditions for microflows can follow two models. Model A is a second order equation while Model B is a simpler first order equation with a general slip coefficient, b , included in the equation. Models A and B are both non-

dimensionalized with respect to length and velocity scale and are shown in equations 29 and 30 respectively (Karniadakis, et. al, 2005:51-166).

$$U_s - U_w = \frac{2 - \sigma_v}{\sigma_v} \left[Kn \left(\frac{\partial U}{\partial n} \right)_s + \frac{Kn^2}{2} \left(\frac{\partial^2 U}{\partial n^2} \right)_s \right] \quad (29)$$

$$U_s - U_w = \frac{2 - \sigma_v}{\sigma_v} \left[\frac{Kn}{1 - bKn} \left(\frac{\partial U}{\partial n} \right)_s \right] \quad (30)$$

For flows in a channel, model B will work well in the center of the channel but will give slight deviations near the walls. These observed deviations are at a maximum at the slip location. Model A will give larger errors towards the center of the channel. The velocity distribution can also be non-dimensionalized as

$$U^*(y, Kn) \equiv U(x, y) / \bar{U}(x) = \left[\frac{-\left(\frac{y}{h}\right)^2 + \frac{y}{h} + \frac{Kn}{1 - bKn}}{\frac{1}{6} + \frac{Kn}{1 - bKn}} \right] \quad (31)$$

where $b = 0$ represents the Maxwell equation of the first order and $b = -1$ represents the second order boundary condition within the slip regime only. The velocity boundary condition models and non-dimensionalized distribution will affect the Knudsen layer, a sub layer between the viscous boundary layer and the wall within approximately one mean free path.

III. Methodology

Chapter Overview

This chapter will focus on simulation set-up. The first section will take a detailed look at the molecular dynamic theory and inputs used for each simulation. Molecular dynamics topics include but are not limited to soft spheres, Leonard-Jones force potential, periodic boundary conditions and molecular wall conditions. The following section will provide a breakdown of the coaxial jet sizing and jet flow for the simulations. The last section will detail the acoustic methods used in the simulations to provide the necessary interference allowing for a comparison with the physical experimentation provided in previous research (Davis, 2006).

Molecular Dynamics

Molecular dynamics techniques numerically solve the N-body problem of classical mechanics (Haile, 1992:15). Simply put, molecular dynamics provides the techniques to solve the second-order equation of motion

$$m_i \ddot{\vec{r}}_i = \vec{f}_i \quad (32)$$

where m_i is the atom's mass (Allen and Tildesley, 1987:71). Molecular dynamic simulation offers the ability to look at single molecules and their interaction with larger scale phenomena. Molecular dynamic simulation can be used to understand the effects of molecule excitation and its effects on the flow around it or how individual molecules form in a turbulent flow. The simulation process on a molecular level can be broken into three steps. The first step requires the modeling of a single molecule specific to the type

of simulation and flow composition required. The second step requires the modeling of a flow consisting of many of the modeled molecules from step one. The final step moves to the analysis of the flow data.

Molecular dynamic particles are modeled in one of two ways. A simulation can contain atoms modeled as hard-spheres. In this instance, as molecules move around in the flow they begin to collide, reacting similar to the balls in a game of billiards. As the molecules hit, there is no deformation of the molecules and the collision provides an immediate repulsion of the molecules. Soft-sphere atoms move through the flow like hard spheres but the soft sphere atom interactions evolve differently. Soft-spheres are modeled using the Lennard-Jones potential and take into account the longer range, attractive dispersion forces along with the short range repulsive overlap forces maintaining the integrity of the molecules themselves (Haile, 1992:188-190). This simulation models molecules as soft-spheres using the Lennard-Jones potential.

Molecular dynamics depends on the interactions of N atoms in a flow, where N could be well over a million ($1E6$) atoms. The possibility of more than $(1E6)^2$ potential atom interactions would prove to be too computationally intensive and could cause simulations to run for months without completion. Instead, the interaction energy of N atoms is taken as “the sum of isolated two-body contributions” (Haile, 1992:188-210). Equations 33 and 34 respectively express the Lennard-Jones potential ($u(r)$) and force ($F(r)$) models using two body interactions for soft-spheres, where σ represents the distance to the zero in $u(r)$, and ε represents the energy at the minimum in $u(r)$.

$$u(r) = 4\varepsilon \left[\left(\frac{\sigma}{r} \right)^{12} - \left(\frac{\sigma}{r} \right)^6 \right] \quad (33)$$

$$F(r) = -\frac{du(r)}{dr} = 24 \frac{\varepsilon}{\sigma} \left[2 \left(\frac{\sigma}{r} \right)^{13} - \left(\frac{\sigma}{r} \right)^7 \right] \quad (34)$$

Limiting the interaction distances among the atoms decreases computational time further.

If an atom sits past a certain distance from another, the two atoms have no significant interaction. So in essence, a minimum distance is selected for interaction of atoms causing the Lennard-Jones potential equation to be expanded to equation 35 where r_c is the minimum interaction distance for the atoms:

$$u(r) = \begin{cases} 4\varepsilon \left[\left(\frac{\sigma}{r} \right)^{12} - \left(\frac{\sigma}{r} \right)^6 \right] & r \leq r_c \\ 0 & r > r_c \end{cases} \quad (35)$$

The simulation flow uses nitrogen as the modeled molecule. The wall fluid potential interaction (ε/k) for nitrogen is 36.5 K and the location of the well between two particles (σ) is 3.293 Å. These parameters are used in the Lennard-Jones force routine (Branam, 2005:25).

Verlet Algorithm and RATTLE Constraints

The Verlet algorithm solves the equations of motion for molecular dynamic simulation. The method is a direct solution of the second-order equations of motion shown in equation 32. The Verlet algorithm method maintains very good energy conservation properties for fairly long time steps and is easily programmable. The Verlet algorithm only needs to account for the position $\vec{r}(t)$, accelerations $\vec{a}(t)$, and the position of the previous time step $\vec{r}(t-\delta t)$ (Allen and Tildesley, 1982:78-82). The velocities themselves

are not present due to cancellations using Taylor expansions and are not necessary to solve for trajectories.

The Verlet algorithm requires two previous positions to estimate the present position.

The algorithm is not a self-starting system and requires more than just a starting position and velocity in order to proceed. Some backward method such as a backward Euler method must be used in order to get $\vec{r}(-\delta t)$ (Haile, 1992:158-159). The method begins with equations 36 and 37, which are added to produce the final Verlet algorithm for positions which is seen in equation 38.

$$\vec{r}(t + \delta t) = \vec{r}(t) + \delta t \cdot \vec{v}(t) + \frac{\delta t^2}{2} \cdot \vec{a}(t) + \dots \quad (36)$$

$$\vec{r}(t - \delta t) = \vec{r}(t) - \delta t \cdot \vec{v}(t) + \frac{\delta t^2}{2} \vec{a}(t) - \dots \quad (37)$$

$$\vec{r}(t + \delta t) = 2\vec{r}(t) - \vec{r}(t - \delta t) + \delta t^2 \cdot \vec{a}(t) + O(\delta t^4) \quad (38)$$

Even though it contains no third order term, the equation is of the third order. The final term in equation 38 expresses the local truncation error which is of the order $(\delta t)^4$ (Haile, 1992:158). Even though the velocity is not needed for the Verlet algorithm it can found by using equation 39.

$$\vec{v}(t) = \frac{\vec{r}(t + \delta t) - \vec{r}(t - \delta t)}{2\delta t}. \quad (39)$$

Choosing the correct step size is also important when using the Verlet algorithm. Using the simulation of liquid argon near the triple point as an example, RMS fluctuations were found to be on the order of 0.01 percent of potential well depth for a time step $\delta t \approx 10^{-14}$ seconds and the fluctuations increased to 0.2 percent for $\delta t \approx 4 \times 10^{-14}$ seconds (Allen and

Tildesley, 1987:79-80). The simulation time steps were kept at 10^{-14} seconds or 10 femtoseconds and checked for validity against analytical solutions.

The basic Verlet algorithm handles velocities in a very awkward manner. Numerical error can be introduced when the basic Verlet algorithm is utilized. The velocity Verlet algorithm provides solutions to the shortcomings of the basic Verlet algorithm. The velocity Verlet algorithm stores positions, velocities, and accelerations all at the same time t , which minimizes any errors due to round-off (Allen and Tildesley, 1987:81). The velocity Verlet algorithm is still a two step integration and only introduces truncation errors of the fourth order (Branam, 2005:25-26). First, equation 40 is used to calculate position at time $t+\delta t$. A mid-step velocity is calculated using equation 41. At this point, forces and accelerations are calculated at the next time step and the new velocity at step $t+\delta t$ is calculated from equation 42. The numerical stability, convenience, and simplicity of the velocity Verlet algorithm make it the best algorithm option presently available (Allen and Tildesley, 1987:82). Branam (2005:25-27) shows the velocity Verlet algorithm coupled with the Lennard-Jones potential provides more accuracy with respect to energy conservation when compared to other higher order integration techniques.

$$\vec{r}(t + \delta t) = \vec{r}(t) + \delta t \cdot \vec{v}(t) + \frac{\delta t^2}{2} \vec{a}(t) \quad (40)$$

$$\vec{v}\left(t + \frac{\delta t}{2}\right) = \vec{v}(t) + \frac{\delta t}{2} \vec{a}(t) \quad (41)$$

$$\vec{v}(t + \delta t) = \vec{v}\left(t + \frac{\delta t}{2}\right) + \frac{\delta t}{2} \vec{a}(t + \delta t) \quad (42)$$

Molecular dynamic simulations require constraints be applied to the system bonds or they can be modeled as discrete potentials separately. While many of an atom's degrees of freedom change under the molecular forces acting on the system, the simulation must maintain the integrity of an atom's bond. Algorithms exist to offer computationally efficient bond constraints. An approach to solving constraints involves a set of unknown multipliers representing the magnitude of forces along the bonds. These forces are required to keep the bond lengths constant. The equations of motion are then solved for one time step with no constraint forces present. The magnitude of the constraint forces can then be determined and used to correct the atomic positions (Allen and Tildesley, 1987:92-98). The RATTLE algorithm handles the equations of motion when internal constraints are present in the system. RATTLE can be considered a variation of the Verlet algorithm with internal constraints in which both the position and velocity at time step t are used to calculate the position and velocity at time step $t+\delta t$ (Andersen, 1983). RATTLE algorithm allows the simulation to constrain other lengths such as internal bond angles when the flow problem is not concerned with internal molecular modes (Branam, 2005:27).

Periodic Boundary Conditions and Neighbor List

Periodic boundary conditions model a repeating pattern in molecular dynamics to simulate infinite dimensions in a given direction when modeling small systems of atoms. A cell created that is smaller than the simulation volume and holds N number of atoms sets periodic boundary conditions. This cell becomes the primary cell and is considered a small portion of the full volume. Exact replica cells surround the primary cell. These cells are considered image cells, as they are in fact mirror images of the primary cell.

These image cells surround the primary cell and hold the same N number of atoms. The atoms in the image cells move as copies of the atoms in the primary cell. Atoms are free to pass from cell to cell through the boundaries but each cell maintains the same number of molecules because as a molecule leaves one cell, a similar atom is entering the cell from the opposite face. The computations are simplified, because the only molecules we need to track are the ones in the primary cell. Using the example of a simple cubic cell, all other molecule positions are a result from the position of an atom in the primary cell, length of the cell and cell transition vector α as seen in the following figure (Haile, 1992:81-86).

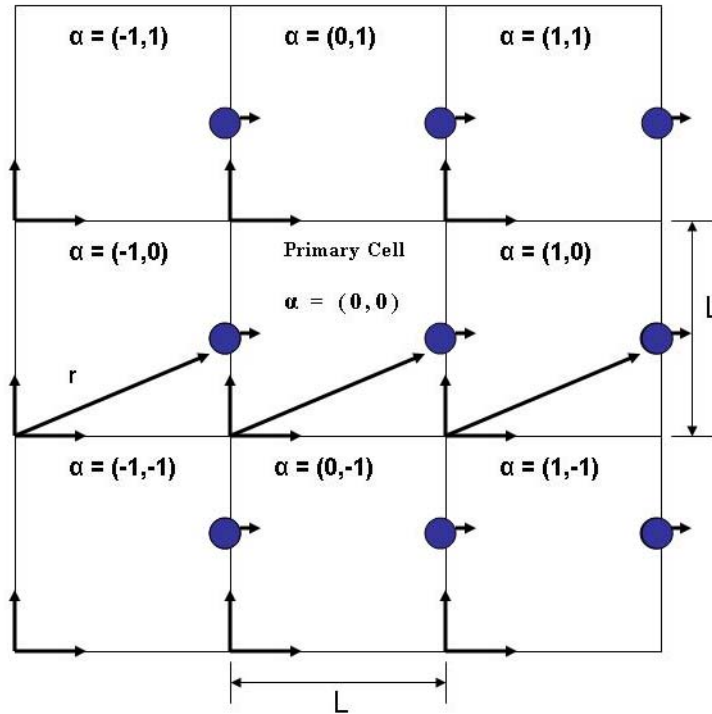


Figure 4. Application of periodic boundary conditions in two dimensions for simple cubic cells. As an atom leaves the primary cell, one can be seen entering the primary cell from the opposite face. The mirror cells mimic the atom movements taking place in the primary cell. (Haile, 1992)

Other molecules located within a certain range of the molecule affect the interactions of a single molecule inside a simulation. The molecules within this range are held in a variable called a neighbor list. The neighbor list is another mechanism used in molecular dynamics to decrease the computational time. A neighbor list limits the amount of reactions needing consideration by one molecule. Each molecule located inside the neighbor list affects the other molecules inside that list. The reactive or attractive force of any molecule outside of the neighbor list is ignored due to the low level of force potential. The list is not a stagnant input and requires updating in relation to the position change δr of the molecules. It is an inverse relationship, as δr increases the neighbor list refresh time decreases. Typically, neighbor lists will be updated every 10 – 20 time steps for a relatively small δr (Rapaport, 1995).

Molecular Dynamics Simulation Development

Branam (2005) created and first used the molecular dynamics computer simulation code used in this research. The code modeled supercritical fluids in a molecular dynamic setting. The original code examined the operation of a single jet. For this research, the code includes the option for studying a coaxial jet flow. The coaxial jet coding allows for varied geometries based on the needs of the user and the extent of the computer resources available. Coaxial velocities may also be varied as desired by the user. An acoustic interference element has been added to the code in order to study the effects on the jet flow. Both single jet and coaxial jet flow simulations can employ the acoustic interference effects. The acoustic interference approach appears later in this chapter.

Molecular Dynamic Simulation Set-up

The molecular dynamic simulation set-up consisted of concentric circular jets issuing into a rectangular box-shaped chamber (Figure 1). The initial research consideration was deciding the physical dimensions of the simulations along with inner and outer flow velocities. The theoretical flow velocity used for this effort was 50 m/s (Branam, 2005). The simulations were run using Poiseuille flow to force particles from the tube into the chamber at the desired speed. A theoretical velocity curve was determined for the pressure driven flow at the velocity of 50 m/s. The first step in the experimentation is to determine the minimum length over diameter, L/D for the tube in order to achieve the theoretical velocity curve previously determined. The minimum L/D will aid in keeping the processing time down while providing the necessary environment for valid molecular dynamic simulations. For this initial experimentation, the tube radius was set at 20\AA to keep the computation time to a minimum. The simulation was run neglecting the chamber for this case. The coaxial tube was modeled as an infinite tube in order to match the velocity profile. The three L/D values considered at this tube radius were 1, 5, and 10. The force multiplier gives the simulation the indication of how hard to push the flow. Using this information, two simulations were run for each of the three L/D values. Each L/D value was simulated with a negligible force multiplier and with the full force multiplier of 1. If any of the L/D values proved to be valid, the pair of velocity curves should straddle the theoretical velocity curve line. Once an L/D value was chosen, the next step in the simulation set-up could be determined.

The second step in the experimentation was to determine the desired force multiplier for our selected L/D , providing an experimental velocity curve capturing the physics of the

problem. Again using 50 m/s and a tube radius of 20Å, the desired force multiplier was experimentally found. The body force multiplier was varied from ~0 to 1 for the selected L/D. The resulting velocity curves were graphed against the theoretical curve and a visual comparison was made. Once the force multiplier was determined, the research effort moved into the next phase of simulations.

The next phase of simulations moved to simulating a coaxial flow with and without acoustic interference. When simulating the effects of acoustics versus the absence of acoustics, a separate simulation set-up was employed. The tube radius was increased to 65Å, which was determined to be the minimum radius possible based on Kn number for the purposes of the research. This radius allows the molecular dynamic simulation to adequately represent continuum solutions (Branam, 2005). Tube length was maintained at five times the tube diameter. The chamber width was also set at five times the tube diameter. The tube wall, chamber wall and coaxial wall temperatures were set at 120K, 300K and 300K respectively. The tube centerline velocity was maintained at 50 m/s while the coaxial jet velocity was varied in separate simulations at 0, 50 and 300 m/s. Later sections discuss the coaxial jet sizing in more detail.

Flow Parameters

Flow in a molecular dynamic simulation is modeled as individual interacting molecules. The flow in this research is modeled using nitrogen molecules. Nitrogen molecules are simple to model and they allow for the consideration of a rotating molecule in the flow field. The temperatures maintained inside the inner tube, outer tube, and chamber are 120 K, 300 K, and 300 K respectively. The densities maintained inside the inner tube,

outer tube, and chamber are 564.79 kg/m^3 , 45.087 kg/m^3 , and 45.087 kg/m^3 respectively. The pressure modeled in the flow is 4.0 MPa.

Equations of State

In molecular dynamics, the thermodynamic properties of a flow are not inputs but rather the results of the simulation. Due to the output of molecular dynamics, turbulent flow requires no special considerations, as Navier-Stokes models do. The velocity distribution becomes an important factor when comparing the results to the actual physics of a problem. The velocity distribution of the particles agrees with the Maxwell/Boltzman distribution at equilibrium (Branam, 2005:15).

Molecular dynamics establishes the temperature, density, and volume for a desired pressure. The temperature at any given time in the simulation is very important for the understanding the results of the simulation. The relationship for absolute temperature is a direct product of kinetic theory (Branam, 2005:22).

Reynolds and Knudsen Number

Reynolds number and Knudsen number ranges play a large part in getting the correct scaling for the simulations in order to provide results comparable to experimental research. The small size of the simulations requires some scaling, while flow conditions along with molecular dynamic considerations drive other variables.

The simulated flow begins in the tube as a laminar flow. As the flow moves into the chamber, a turbulent flow field is expected due to flow instabilities. Reynolds numbers for experimental turbulent tube flows in these conditions are usually between 10,000 and 100,000. These high Re are the calling card of turbulent flows. The limits on the number

of particles molecular dynamic simulations can model forces Re for this research effort to be closer to 1.0. The low Re is the largest indicator of uncertainty when modeling flow fields in this manner. Regardless, previous work has shown good agreement with experimental results (Branam, 2005).

Knudsen number plays a larger part in the description of the flow as well as the acoustic interference. For a slip condition, the Kn will be in the range of 0.01 and 0.1. The simulations presently are operating in the no-slip regime and require a $Kn < 0.01$.

Coaxial Jet Sizing

The coaxial jet experimentation was to be compared to the previous dissertation work of Davis (2006). While Davis' work was qualitative, this research will be both a quantitative and qualitative effort. To get the best research comparisons for the coaxial jet flow, the molecular dynamic model needed to be scaled similarly in order to show comparisons to the dimensions of the physical model in Davis' work. The physical model appears in Figure 5. The inner jet diameter was 0.5 mm while the outer jet diameter was 2.42 mm. The coaxial jet outer to inner diameter ratio D_o/D_i was 4.84. The thickness between the inner and outer core was give as 0.54 mm.

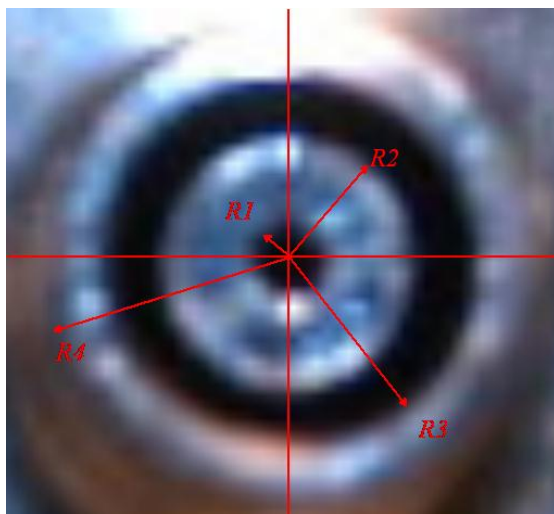


Figure 5. Close-up image of the coaxial injector tip area, the dimensions of the injector are: $R_1 = 0.25$ mm, $R_2 = 0.79$ mm, $R_3 = 1.21$ mm and $R_4 = 1.59$ mm. (Davis and Chehroudi, 2006)

Molecular dynamic simulation is limited to nanometers as opposed to mm. The coaxial tube needs to be scaled while maintaining the geometry of the physical model as much as possible. In order to achieve a valid molecular simulation, the inner tube diameter needed to be 65\AA . Using this initial dimension as a base, the ratios of the physical model determined the remaining geometry of the coaxial jet. The resulting geometry gave an inner diameter of 65\AA , an outer diameter of 314.6\AA and 140.4\AA spacing between the inner and outer jets. This geometry maintained the D_o/D_i at 4.84. Figure 6 provides a pictorial representation of the molecular dynamic simulation of the coaxial jet.

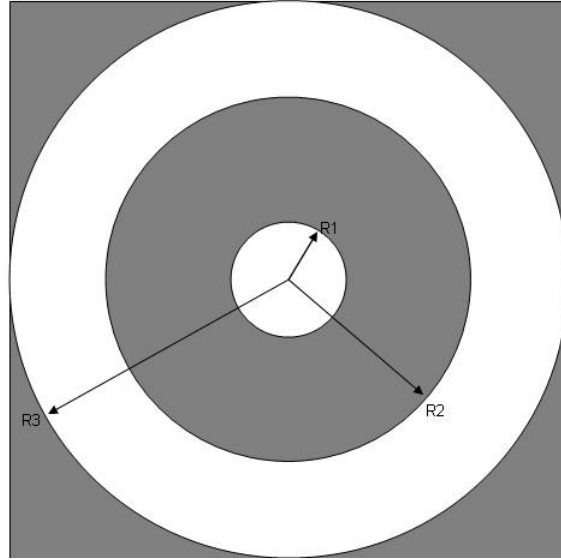


Figure 6. Pictorial representation of the coaxial injector tip area, the dimensions of the injector are: $R_1 = 65\text{\AA}$, $R_2 = 205.4\text{\AA}$, $R_3 = 314.6\text{\AA}$.

After running multiple simulations using the new geometry, the scaling of the coaxial jet needed to be changed. The ratio of the jet's outer to inner diameter caused problems as the calculations exceeded the available resources available for the simulation. The coaxial jet would need to be smaller to fit the capabilities of the available computing facilities. The ratio of outer to inner diameter D_o/D_i for the physical model of the coaxial jet started at 4.84 but needed to be decreased to 4.0. D_o/D_i was the only ratio change made to the simulated coaxial jet. The inner jet diameter was maintained at 65\AA and the spacing between the outer and inner jet was maintained. In essence, the outer jet area was decreased to fit computing capabilities. Figure 7 provides a pictorial representation of the new simulated coaxial jet. The decrease in the outer jet area is clearly visible as the outer jet thickness is halved from 109.2\AA to 54.6\AA .

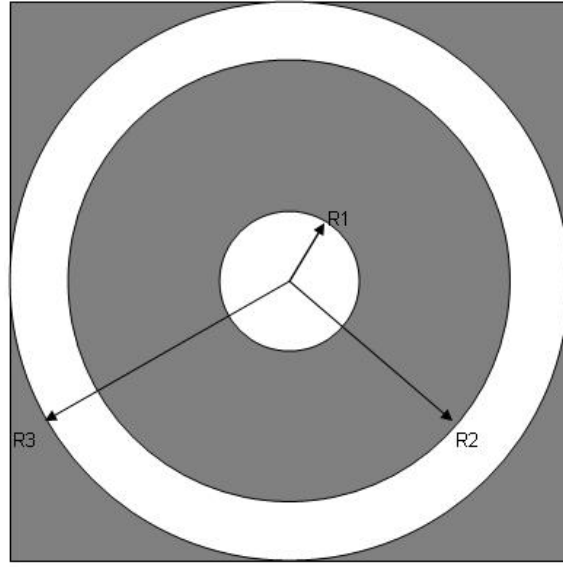


Figure 7. Pictorial representation of the coaxial injector tip area, the dimensions of the injector are: $R_1 = 65\text{\AA}$, $R_2 = 205.4\text{\AA}$, $R_3 = 260\text{\AA}$.

While the coaxial jet geometry and inner jet velocity will not change throughout the several planned simulations, the same can not be said for the outer jet velocity. While the inner jet velocity was 50 m/s, the outer jet velocity will be varied to provide a wide range for U_o/U_i . Due to the present simulation run times, the research will initially look at three outer jet velocities. The outer jet velocities will be 0, 50 and 300 m/s providing a U_o/U_i of 0, 1, and 6 respectively.

Weber number (We) is a dimensionless ratio of momentum force to surface tension force, which helps describe shear flow. Weber number for a single jet is expressed in equation 43.

$$We = \frac{\rho U^2 d}{\sigma} \quad (43)$$

When calculating We for a coaxial flow, the difference between inner and outer jets must be accounted for and the equation is expanded to

$$We = \frac{\rho(U_o^2 - U_i^2)d}{\sigma} \quad (44)$$

where d is the inner tube diameter and σ is the surface tension. The simulation does not employ a two-phase flow, so surface tension is not a significant factor. Momentum ratios and momentum flux ratios provide similar information about jets without taking into account surface tension. There is no momentum ratio or momentum flux of outer to inner jet (equations 45 and 46 respectively) for the single jet case.

$$M_R = (\rho_o U_o^2 A_o) / (\rho_i U_i^2 A_i) \quad (45)$$

$$M = (\rho_o U_o^2) / (\rho_i U_i^2) \quad (46)$$

Momentum flux ratio is a key quantity for near-field geometry of a coaxial configuration (Villermaux, 1998:807). Momentum flux ratio highly affects jet shapes and spray angles. The inner potential core length over inner diameter ratio shares a strong relationship with M . For single-phase flow, which is the focus of this research, the two are inversely related with inner core length over inner diameter ratio $\sim M^{1/2}$. Due to this inverse relationship, very low momentum ratios ($M < 1$) cause the inner jet to destabilize very slowly, increasing the inner potential core length to inner diameter ratio (Villermaux, 1998:811). The momentum ratios for $U_o/U_i = 1$ and 6 are 0.798 and 2.874, respectively. While the jet velocity ratio provides information about the flow, momentum ratio encompasses the flow and shape of the jet issuing into the chamber.

Chamber Methodology

After the flow exits the tube, it is issued into a chamber having many of its attributes defined by the molecular dynamic simulation. The chamber is a box with the size

determined by the user with fail-safe mechanisms correcting the sizing if it is out-of bounds of the physical requirements. The chamber utilizes periodic boundary conditions. For data analysis purposes, the chamber is separated into eleven segments. Each of the segments averages the properties of the flow field within that segment and outputs data accordingly. The data profiles are displayed radially to best represent the axisymmetric nature of this flow problem.

Wall Methodology

The walls of the tube are an important aspect of the molecular dynamic simulation. The molecular dynamic simulation code is set-up to handle multiple wall conditions. Branam (2005:39-48) has done work to compare the modeling of walls as a system of particles. The models were compared to a diffusively reflecting wall model. The diffusely reflecting wall represents the simplest of the wall models. The model uses a Maxwell-Boltzmann distribution to determine the velocity and magnitude of the particles reflecting from the wall. The one zone wall utilizes springs to anchor the wall particles to the lattice site and includes a stochastic zone. “The stochastic zone acts like a thermal reservoir to dissipate energy transferred to the wall from the fluid (Branam, 2005:41).” The two-zone wall allows the wall particles to vibrate around their lattice sites while continuing to absorb energy from the fluid. The three-zone wall includes a reaction zone directly interacting with the fluid particles. It also includes a stochastic zone and a layer of stationary particles. This research relied on the three-zone wall due to its demonstrated ability to best capture the physics of the simulations. The three-zone wall is the most complex of the three wall models and does increase computing times. Figure

8 shows the geometry of the three-zone wall. The three-zone wall uses the Lennard-Jones potential to determine the intermolecular forces within the wall, as well as to govern the interactions between wall and flow particles (Branam, 2005:41-46).

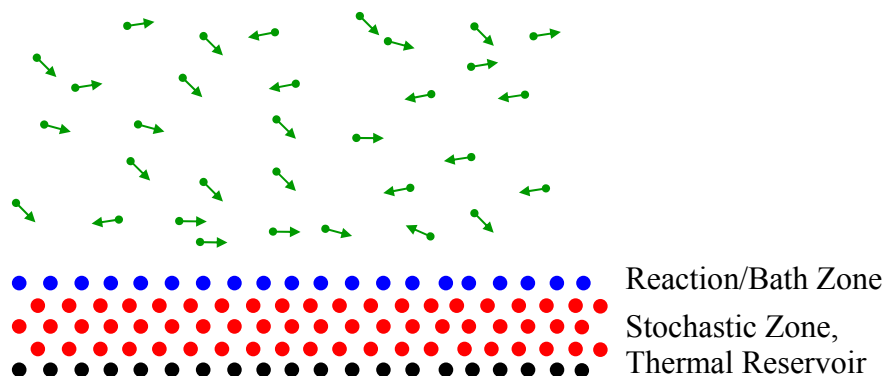


Figure 8. Three-Zone Wall Model (Branam, 2005:46)

Acoustics Set-Up

Acoustic interference is simulated in two manners for this effort. The first method will simulate the wall as a row of modeled particles applying pressure against a chamber wall. The second method will model the acoustic interference using a force model representing discrete wall particles. The entire molecular dynamics system is modeled as particles, including walls and coaxial structures. Particle modeling was the inspiration behind the first method of acoustic interference. Rows of particles were used to model the interference along a face of the chamber. The molecules were given amplitude and frequency in order to mimic the desired acoustic set-up. The acoustic interference was modeled for an SPL of 90 dB and for a range of frequencies between 10 and 12 kHz. The frequency scaling required to affect the simulations is discussed later in the section. An acoustic frequency was selected to provide comparable results to previous experimental research efforts. The frequency is used in the wave equation to give the

wave displacement amplitude (“Decibel Scales”, undated). The pressure amplitude is then calculated and compared to atmospheric pressure using the SPL equation producing a decibel level. The acoustic molecules were modeled using SPL. The acoustic molecules were arranged in three rows and placed against the y-axis of the chamber. The molecules could then affect the chamber particles by moving with the desired displacement creating a force against the chamber particles.

This research also explored a mathematical acoustic interference model. If the acoustic pressure necessary to provide the desired displacement could be decided upon, then it would be possible to calculate the desired force from the definition of pressure.

Similarly, acoustic pressure can be added to the force calculations based on the definition of pressure felt between interacting molecules. The pressure is calculated from the virial work term.

Considering a virial term for acoustic pressure analogous to the term used to define pressure, an acoustic force factor (ff_{acous}) results. The pressure term as determined from a Lennard-Jones potential is

$$P_{LJ} = \frac{8\varepsilon}{Vol} \left(\frac{\sigma^{12}}{r^{12}} - \frac{\sigma^6}{2r^6} \right) = \frac{ff_{LJ} r}{6Vol} \quad (47)$$

Substituting an acoustic pressure into this expression and solving for an acoustic force factor yields

$$ff_{acous} = \frac{P_{acous} (6 \cdot Vol)}{r} \quad (48)$$

This method due to its inverse relationship with distance between interacting molecules requires the placement of a phantom line in between the acoustic particles and the

chamber particles to capture the true physics of the problem and provide a computational limiter. Once an acoustic force is calculated, it needs to be given a sinusoidal component. The sinusoidal wave representing the acoustic force then becomes

$$f_{acous} = ff_{acous} \sin(\omega t - \phi) \quad (49)$$

The operating frequency modeled by the acoustic interference is in the range of 10.0 – 12.0 kHz. These frequencies do not affect the model in their present state due to the size of the simulations. Frequency scaling is needed in order to achieve the proper interference. Frequencies are scaled higher to affect the simulation. A reference tube radius of 1 cm is used for scaling purposes. The operating frequency range is equated to operating on the reference tube radius. The frequency is then scaled higher using equation 50.

$$\omega = \omega_o \frac{r_a}{r} \quad (50)$$

Parallel Computing

Due to the computationally intensive calculations required for molecular dynamic simulations, steps are taken to make the process work more efficiently. Running the simulation on multiple processors leads to shortened simulation completion times. The computing resources consisted of a cluster of networked servers. Sixty-four nodes existed offering 128 2.2 GHz Opteron 248 CPUs. Each node provides 4 GB of memory with 54 GB of local work partition per node. The nodes were also capable of 1 MB of secondary cache per processor. The parallelization scheme employed Message Passing Interface (MPI) in the code to take advantage of the available computer resources.

Increasing the number of processors used to run a simulation in general will decrease the wall calculation times but increases the overall CPU hours. Branam (2005) found as the number of processes used increases the communication time also increases and a breakeven point is eventually reached. The best parallel processing compromise for the simulations in this research was 8 nodes with two processes per node. Branam (2005) also showed the utilization of the velocity Verlet algorithm and RATTLE constraints required one major communication per time step. For small simulations using argon and nitrogen communication times equated to 50% of the simulation run time on 16 processes.

The code's parallelization technique used particle decomposition. The technique balances calculations between processors improving efficiencies. With particle decomposition, each processor is responsible for the calculations of a set of particles rather than passing particles between processors. Each processor will be aware of all the particles but will only be responsible for the force calculations of their specific particles. This method is a fairly efficient technique used to balance force and neighbor calculations but it reaches an upper limit near two million particles when 2.0 GB per process of memory is available.

IV. Results

Chapter Overview

This chapter presents the results of the research. The first section looks at the initial steps taken to match the theoretical radial velocity profile in the tube. The variation of the tube length over tube diameter is discussed along with the force factor variations made to match the theoretical curve. This section also shows the actual velocity profiles for the tube and coax produced during the simulations. The simulated velocity curves are compared with the theoretical curves and conclusions are drawn. The next section delves into the acoustic models used in this research. The two acoustic interference models are compared to cases with the acoustics turned off in order to validate each of the models. Next, mixing along the centerline of the chamber is investigated. The effects of acoustic interference on mixing are discussed for all three cases. The effects of different velocity ratios on the mixing are also investigated. The radial density profiles for each case are examined in the final section. The density profile provides valuable information about the shape of the jets issuing into the chamber.

Matching Theoretical Velocity Profile

The initial experimentation used to determine the minimum tube length necessary to get a valid flow profile was completed using an earlier and simpler molecular dynamic simulation tool. In order to determine the valid velocity profile matching the theoretical flow profile, the simulation ran multiple times varying both the ratio of tube length to tube diameter, L/D and the force factor used to create the Poiseuille flow conditions throughout the tube and chamber. The injector simulation was set to an initial velocity of

50 m/s. For a fixed diameter size of 20 Å, injection was simulated for L/D values of 1, 5 and 10. Each L/D value was also simulated for a force factor of approximately 0 and 1. The ideal case would find the theoretical flow profile line straddled by the experimental flow profiles for a force factor of ~0 and 1. Figures 9, 10 and 11 show the flow profiles of L/D = 1, 10 and 5 respectively as they are compared to the same theoretical velocity profile. Velocity profile charts do not represent velocity as it flows through the tube. The x-axis, r/r_{tube} , of the velocity profile is representative of the change from 0.0, which represents the centerline of the inner tube to 1.0, which represents the wall of the inner tube.

Analytical flow profiles for L/D = 1 at force factors of ~0 and 1 did not surround the theoretical flow profile and were discarded as a potential flow geometry. Flow profiles for L/D = 5 and 10 both fit the criteria for possibly matching the theoretical flow profile. For these two geometries, the theoretical flow profile sits between the force factor profiles. Since both are feasible geometries, L/D = 5 was selected to minimize computational run time.

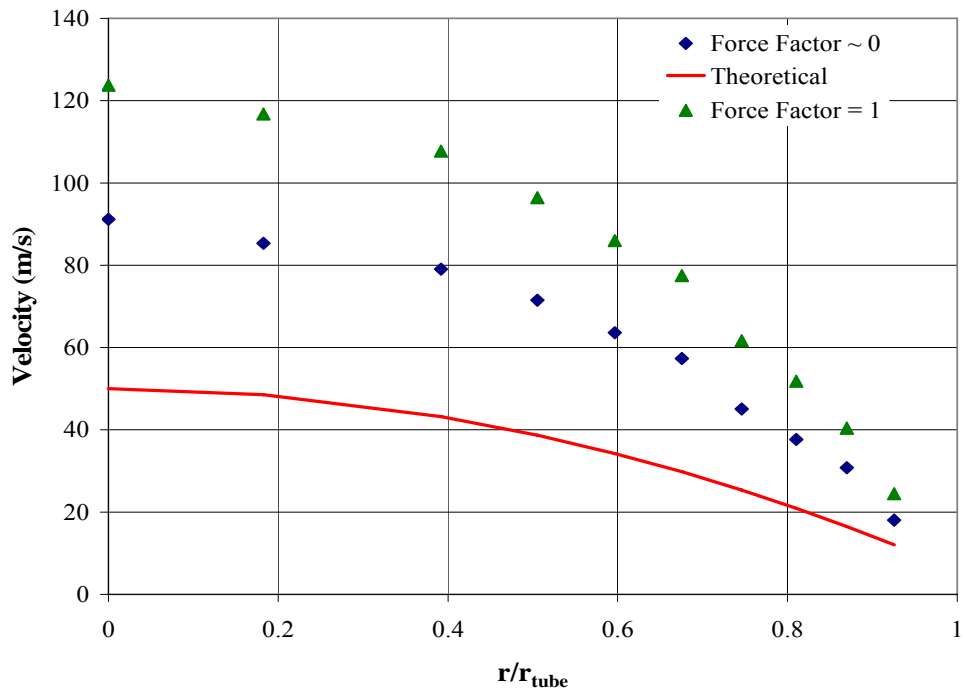


Figure 9. Radial Velocity Profile, $r_{\text{tube}} = 20\text{\AA}$, $L/D = 1$

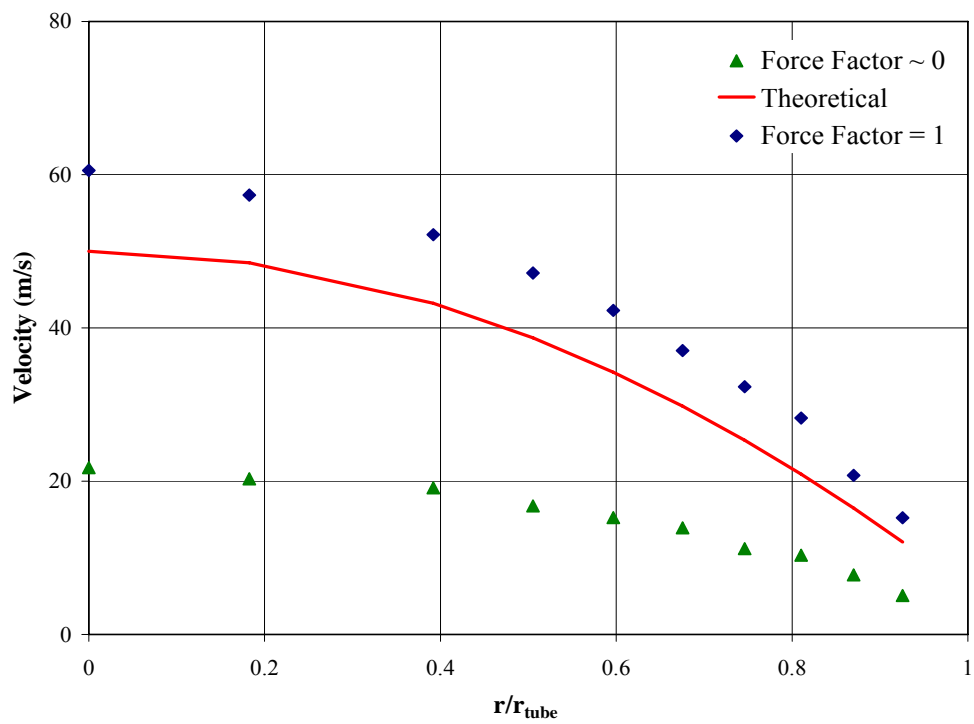


Figure 10. Radial Velocity Profile, $r_{\text{tube}} = 20\text{\AA}$, $L/D = 10$

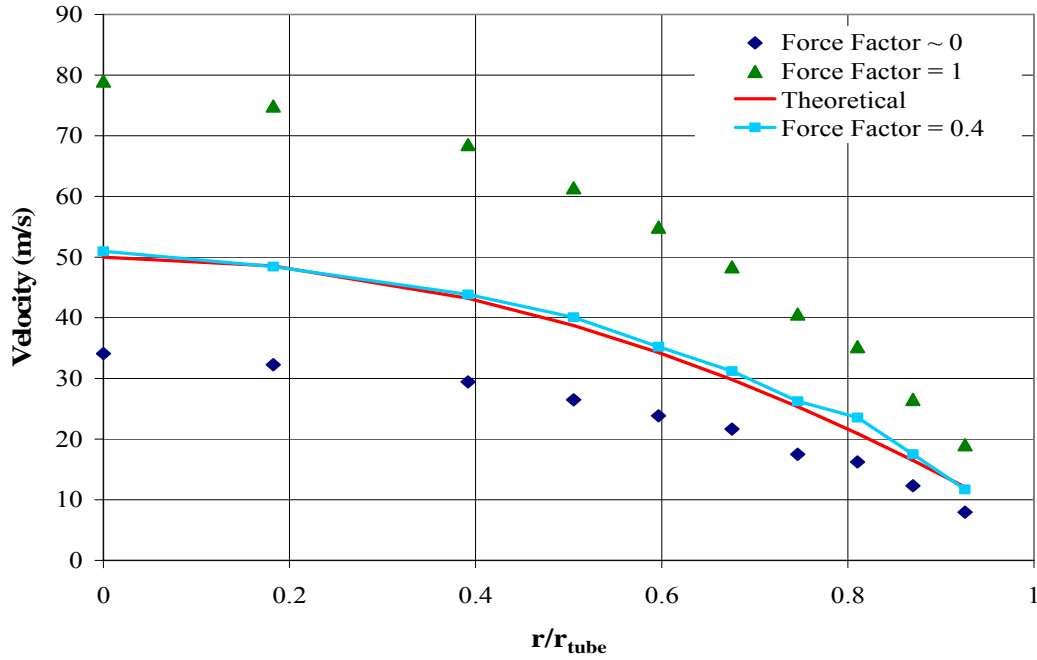


Figure 11. Radial Velocity Profile, $r_{\text{tube}} = 20\text{\AA}$, $L/D = 5$

A force factor of ~ 0 provided a flow profile below the desired initial speed of 50 m/s while a force factor of 1 produced an initial flow velocity almost twice the theoretical value. The force factor was then adjusted by 0.05 from 0.05 to 1 until the analytical profile matched closely the theoretical profile. The curve alignment occurred at a force factor of 0.4 (Figure 11). The final geometry chosen was $L/D = 5$ with a force factor of 0.4. This geometry and the force factor were maintained throughout the rest of the simulations.

Velocity Profile

Figure 12 shows the velocity profile for the single jet flow. The velocity profile error bars represent a spatial resolution that captures the values and trends of the data. The velocity curve for acoustic free and acoustic interference models show acceleration in the tube after the simulation is first begun. This same trend appears later in the other simulation

cases. The transience caused by starting the jet to issue into the chamber causes the acceleration of the tube flow. The flow of molecules appears to rush into the chamber but as the simulation moves towards the tube walls, the velocity decreases until it converges closely to the expected value. The single jet was previously studied and matching the theoretical curve has been accomplished but more may need to be done to ensure the coaxial flow field can be controlled similarly.

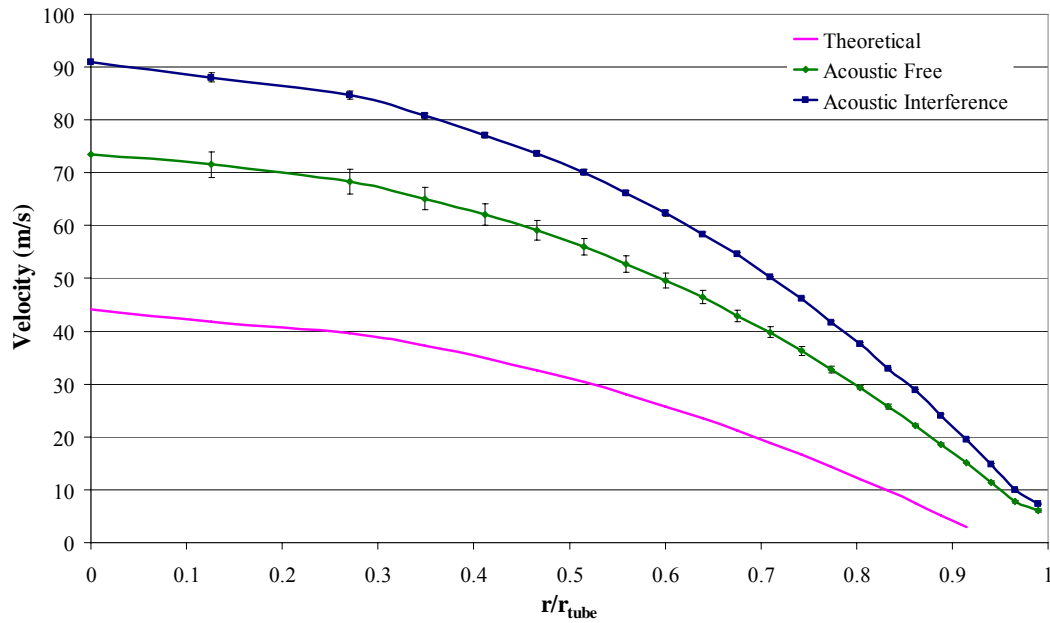


Figure 12. Radial Velocity Profile for $U_o = 0$ m/s, $U_i = 50$ m/s

Figures 13 and 14 show the trends of both the acoustic free and acoustic interference models for $U_o/U_i = 1$ and 6 respectively. The addition of the coaxial component to the flow creates some interesting results. For $U_o/U_i = 1$ and 6, similar results can be seen. The theoretical curve for the inner tube remains unchanged but the acoustic free velocity curves for each show increased initial velocity. The two acoustic free velocity curves for $U_o/U_i = 1$ and 6 show an increased initial velocity in the tube. The acoustic interference curve shows acceleration in both coaxial cases. In Figure 13, the acoustic free model for

$U_o/U_i = 1$ shows smaller levels of acceleration when compared to the other cases. The probable reason is the level of data collected for this case is small when compared to other cases. Acceleration is to be expected in the acoustic free case for $U_o/U_i = 1$ once more data is collected. The acoustic free and acoustic interference models for the $U_o/U_i = 6$ case have a very similar centerline velocity, leading to the conclusion the acoustic interference is not the leading effect in starting the tube flow. The addition of the coaxial jet affects the pressure for flow issuing out of the tube centerline.

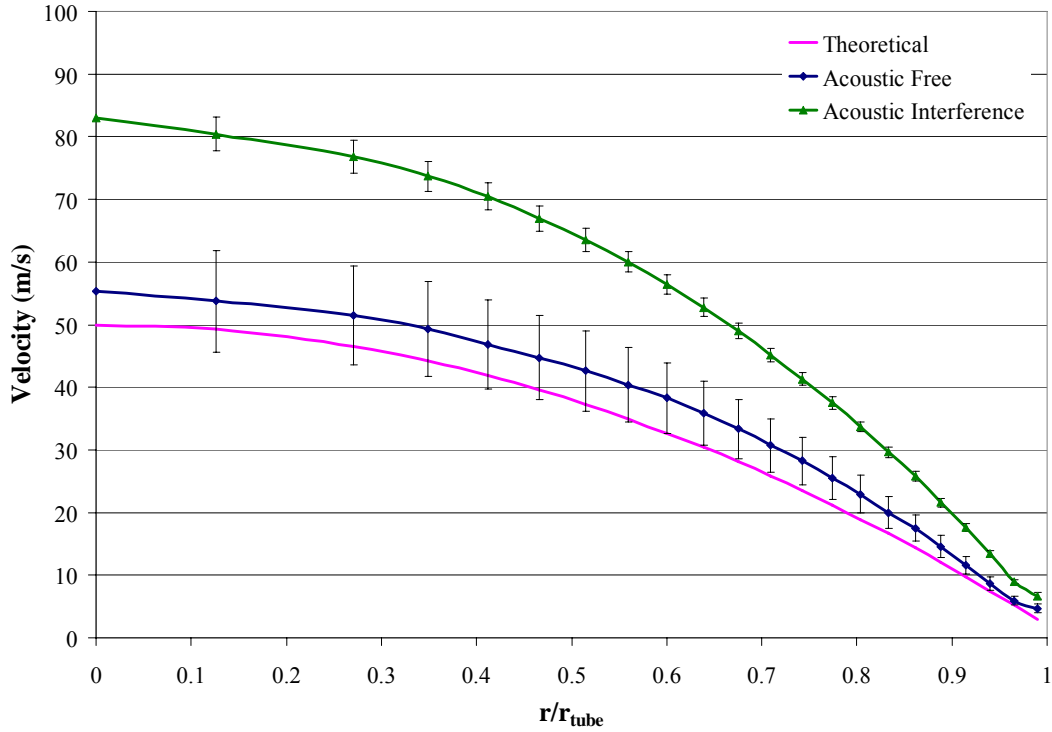


Figure 13. Radial Velocity Profile for $U_o = 50$ m/s, $U_i = 50$ m/s

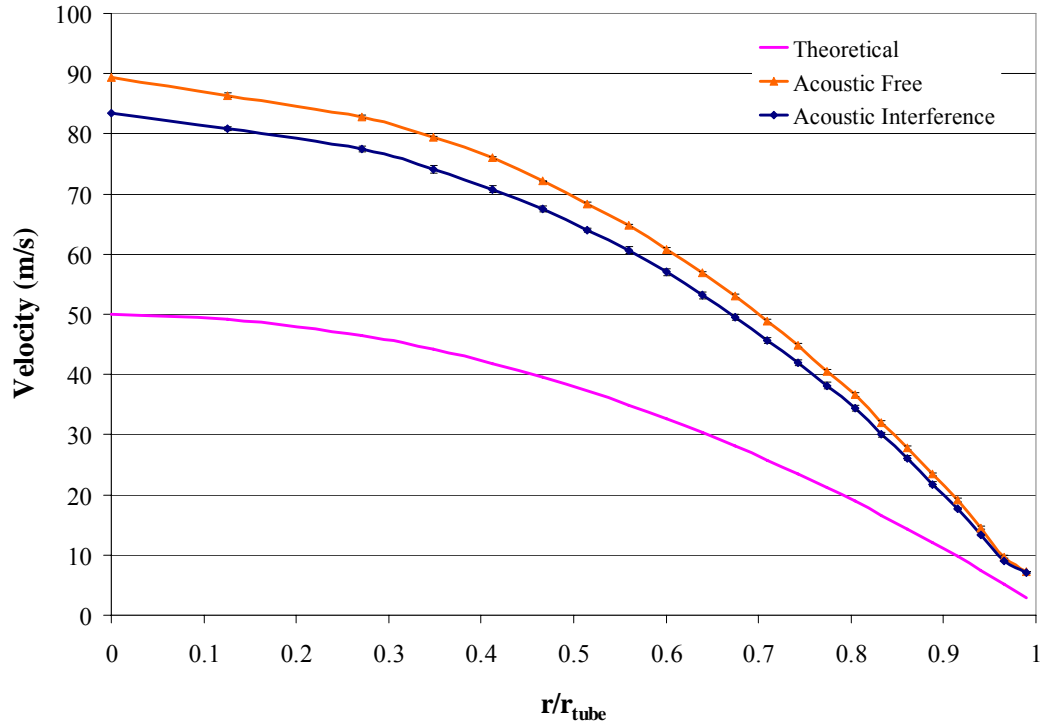


Figure 14. Radial Velocity Profile for $U_o = 300$ m/s, $U_i = 50$ m/s

A theoretical velocity profile for the outer tube was calculated for comparison to the simulated coaxial profiles. The velocity profile charts for the outer tube differ from the velocity profile charts for the inner tube. The y-axis still represents velocity while the x-axis still represents a radius ratio. The x-axis, $r/(r_o - r_i)$, represents the inner wall of the outer tube at 0.0 to the outer wall of the outer tube at 1.0. Figures 15 and 16 show the theoretical coaxial velocity curves for $U_o = 50$ m/s and 300 m/s respectively. The theoretical coaxial velocity curve for both cases is plotted across the entire coaxial radius. The curve across the coaxial radius takes a parabolic shape peaking close to the centerline. The simulated coaxial curves do not in any way follow the trend of the theoretical curve. The curves for the acoustic free and acoustic interference models

follow similar trends especially in the $U_o/U_i = 6$ case. These results need further investigation.

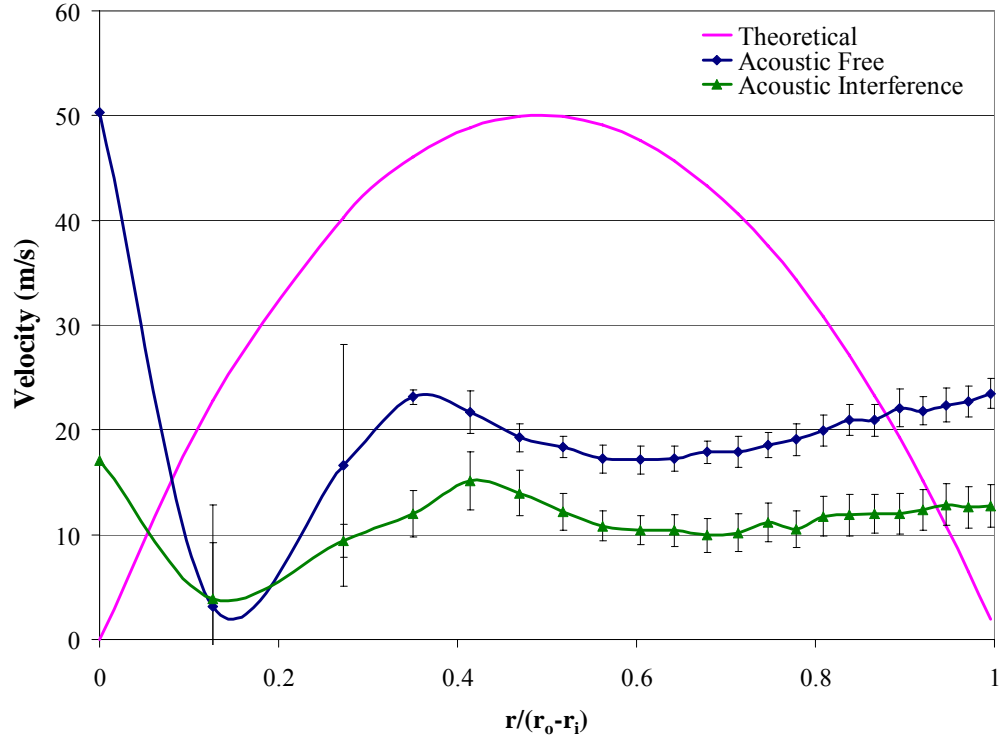


Figure 15. Coaxial Velocity Profile for $U_o = 50$ m/s, $U_i = 50$ m/s

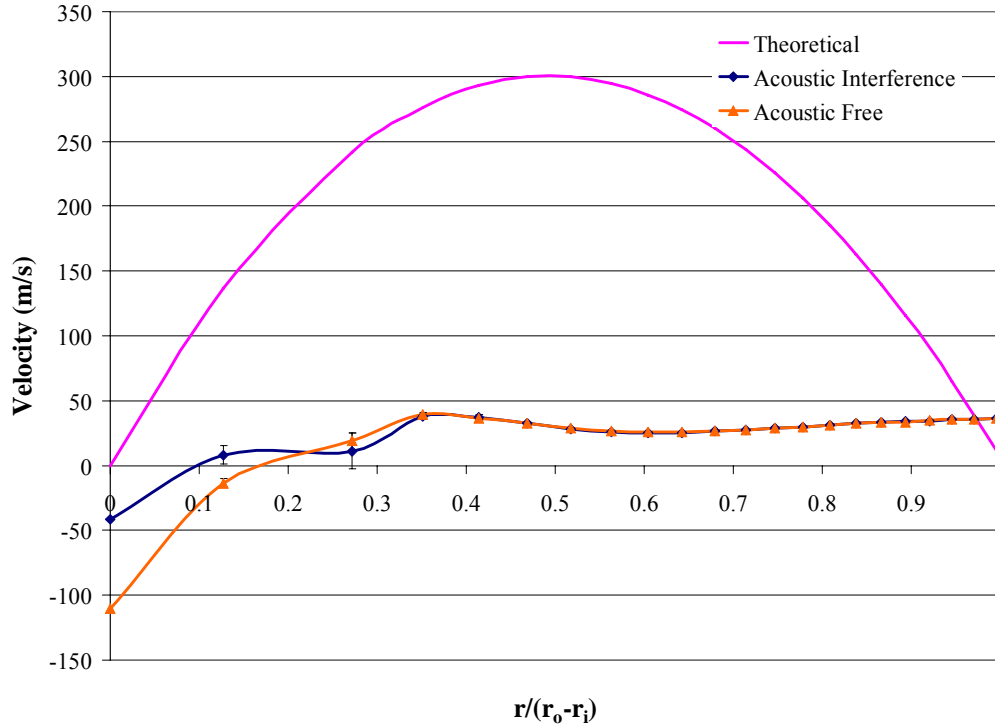


Figure 16. Coaxial Velocity Profile for $U_o = 300$ m/s, $U_i = 50$ m/s

The simulated coaxial curve for $U_o = 50$ m/s does initially begin at 50 m/s but shows a large drop-off in velocity before accelerating again only to decelerate further from the centerline with the curve ending in an acceleration. The shape of the curve resembles a decaying sinusoidal wave. The coaxial velocity profile for $U_o = 300$ m/s has a somewhat similar profile but initially the flow in this case is moving at a negative rate and begins to accelerate fluctuating until it balances towards the outer coaxial wall. As discussed earlier, the size of the coaxial component had to be decreased to stay within the computational limits of the computer network. The shape of the velocity profiles is most likely due to small gap width in the coaxial tube. As stated earlier, Kn for continuum flow should be less than 0.01. Kn reached 0.29 in the coaxial component which is well outside the limits of continuum flow. The decreased size of the coaxial jet may have

affected the simulation. The smaller size does not seem to be able to accurately capture the physics of the problem.

Acoustic Model Validation

Mass fraction charts represent the mixing of the atoms from the tube and coax with the chamber particles. Lower mass fractions represent higher mixing in the chamber. The mass fraction charts show mass fractions ranging from 0.0 to 1.0 on the y-axis. The x-axis, z/d , is the non-dimensionalized chamber length. It was stated earlier that the chamber is divided into 11 sections. The non-dimensionalized values of the x-axis represent the 11 chamber sections. Figure 17 shows the earliest captured mixing at $U_o/U_i = 6$ for all three models. Even at this early stage, there is much that can be drawn from the chart. The acoustic free model and discrete particle model produce very similar curves. The force model curve on the other hand shows increased mixing in the chamber. Observing the flow after half of a nanosecond provides similar results. The acoustic free model and the discrete particle model appear to lie on top of each other. The force model again shows increased mixing when compared to the acoustic free model as the flow develops. As the flow develops in time, the force model mixing seems to decrease and converge to the level of mixing in the acoustic free model. The force model then separates and produces lower mixing fractions than the acoustic free case. Even though Figures 17 and 18 represent flows that have not reached a steady state, from these figures, it is the discrete particle model of acoustic interference is not affecting the chamber as intended. The probable reason for the ineffectiveness of the model is the need for a larger system and more acoustic particles. The acoustic particles in the discrete particle

model presently operate at a 90dB SPL. At 90 dB, the Lennard-Jones forces for the acoustic atoms are negligible after 9.89 Å. The mean free path for our chamber is approximately 16 Å. Due to the size scale of the simulation, simply increasing the decibel level to 100 dB creates a 20 Å acoustic displacement, too big to affect any chamber particles. The present decibel level is limited to a regime unable to affect our chamber at the present sizes.

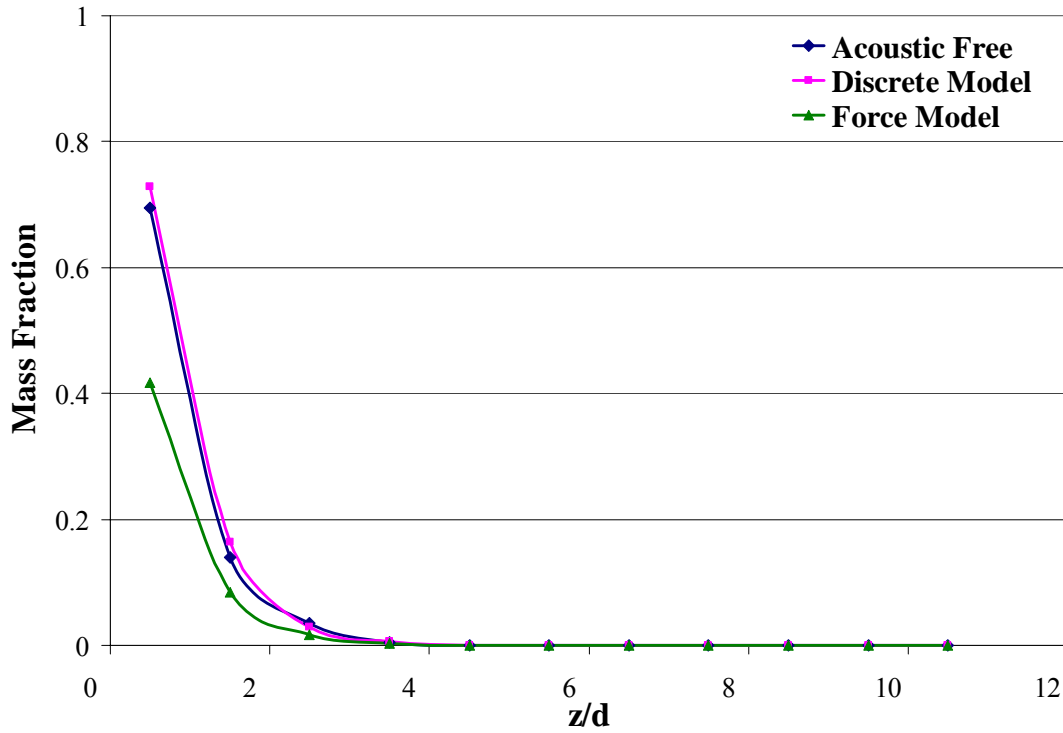


Figure 17. Centerline Mixing Comparison at 0.25 ns, $U_o = 300$ m/s, $U_i = 50$ m/s

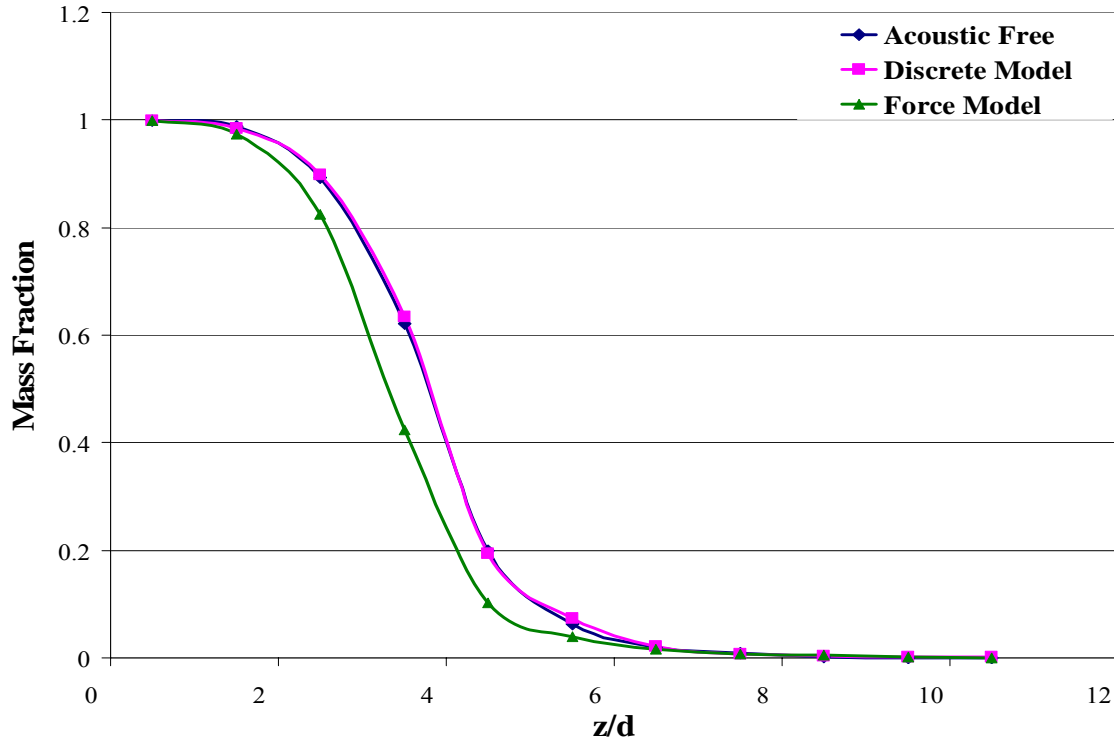


Figure 18. Centerline Mixing Comparison at 0.75 ns, $U_o = 300$ m/s, $U_i = 50$ m/s

Figures 19 and 20 show the acoustic free and force model cases for a coaxial velocity of 50 m/s. The acoustic discrete particle model is omitted from the graph since it does not capturing the physics of the problem. Figures 19 and 20 show similar mass fraction trends validating the force model of acoustic interference. Increased mixing is evident in the force model case in both charts. The acoustic free model does not exhibit mixing on the level seen for the acoustic interference model.

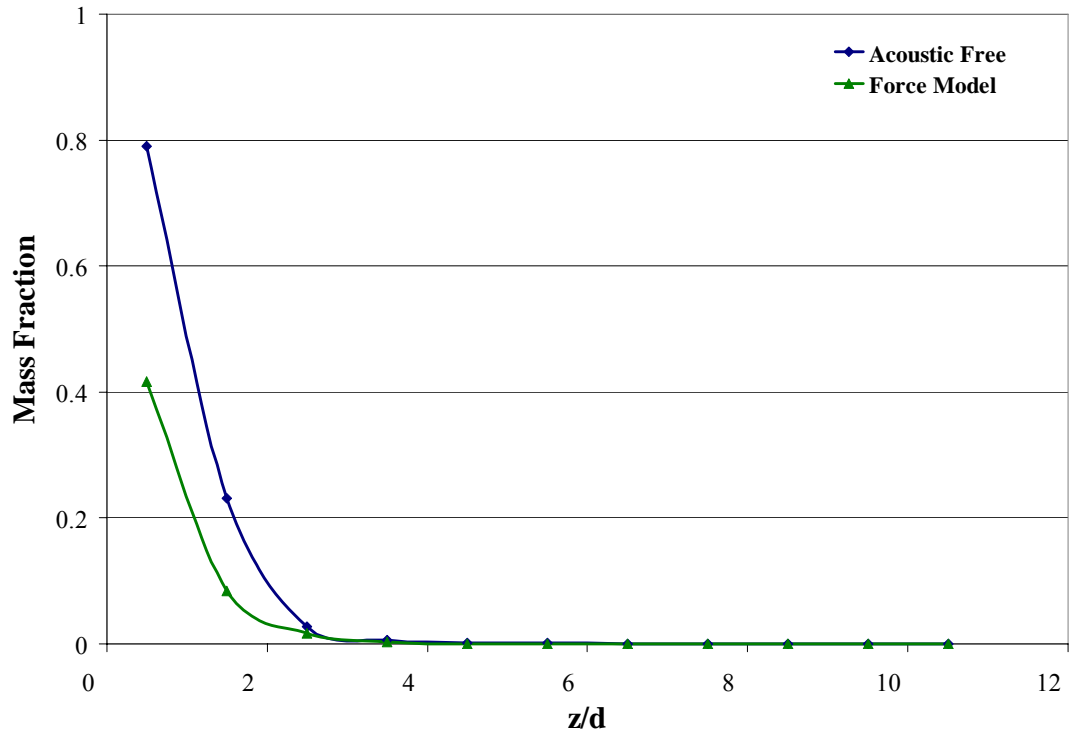


Figure 19. Centerline Mixing Comparison at 0.25 ns, $U_o = 50$ m/s, $U_i = 50$ m/s

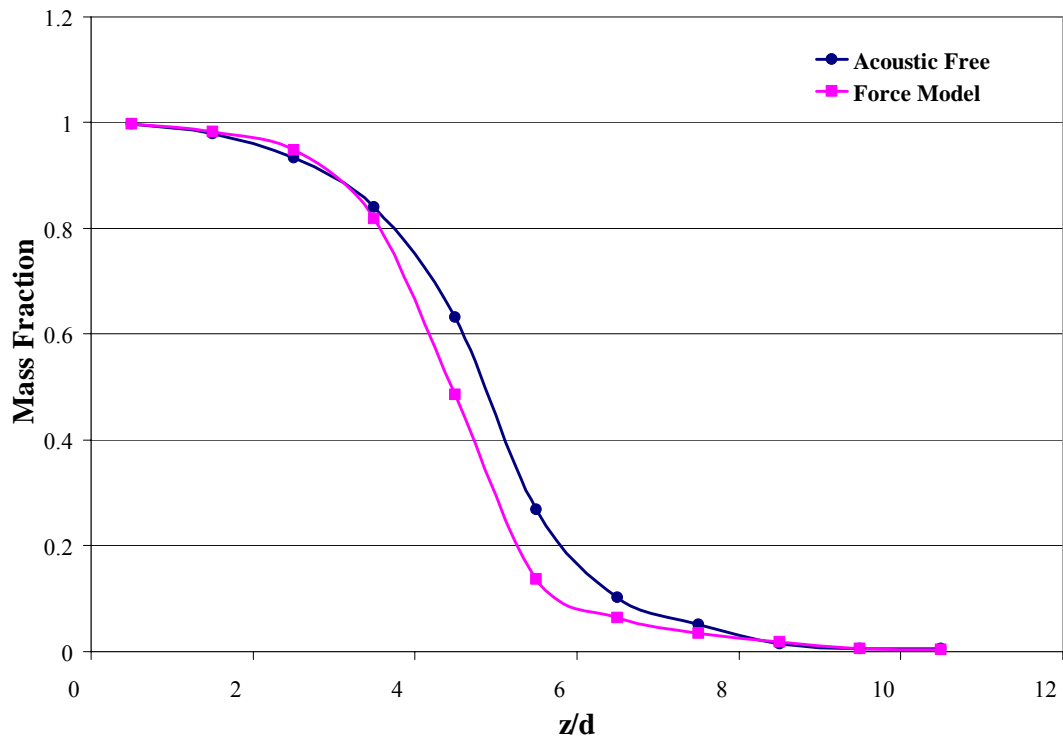


Figure 20. Centerline Mixing Comparison at 1.0 ns, $U_o = 50$ m/s, $U_i = 50$ m/s

Centerline Flow Development

The development of the flow in the chamber is an important aspect in verifying the simulation. Looking at the six cases and following the development of the flow through centerline mass fraction data provides a good look into how the flow is mixing throughout the chamber. The mass fraction is plotted against the non-dimensionalized axial chamber dimension. The mass fraction is the ratio of mass injected into the chamber over the mass at the specified location in the flow. Again, the mass fraction gives insight into the level of mixing in the chamber.

The first two cases to be discussed are $U_0 = 0$ m/s with and without acoustic interference. Figure 21 shows the development of the flow at the centerline for $U_0 = 0$ m/s for the acoustic free case. The flow develops as time progresses, steadily up to about 1.0 ns. As time continues past 1.0 ns, the flow mixing increases as the flow moves longitudinally towards the center of the chamber. The variations seen in mass fraction ratios results from the initial acceleration of the jet into the chamber. Mass fraction data at 2.0 and 3.0 ns shows decreased mixing when compared to the 1.0 ns curve but the data also shows the flow moving close to a steady state. As the flow moves further into the chamber, the flow exhibits a slight oscillatory nature. This oscillatory motion is apparent between 2.0 ns and 3.0 ns.

Figure 22 shows the effects of acoustic interference on the flow when $U_0 = 0$ m/s. The flow acts similar to the acoustic free flow. The mass fraction increases with time and reaches a point at approximately 2.0 ns where the flow mixing begins to converge.

Looking at 2.0 and 3.0 ns curves it appears the flow in the chamber near the injector has reached a steady state condition. Figure 23 shows a running comparison of the acoustic

free case with the acoustic interference case. At the early stages of the simulation, very little difference is observed between the acoustic free and acoustic interference cases. As the simulation time increases and the flow moves further into the chamber, the acoustic free model for $U_0 = 0$ m/s exhibits more mixing than the acoustic interference model. The acoustic free case mixes the injected mass much better throughout the chamber and shows much higher mass dissipation. The jet reaches as far as $z/d \sim 10$ as evidenced by the presence of mass injected into the chamber. The acoustic free model also seems to move closer to a steady state value at 3.0 ns. The mass fraction curves at 2.0 and 3.0 ns show little difference while the acoustic interference case needs longer simulation times to reach a steady condition.

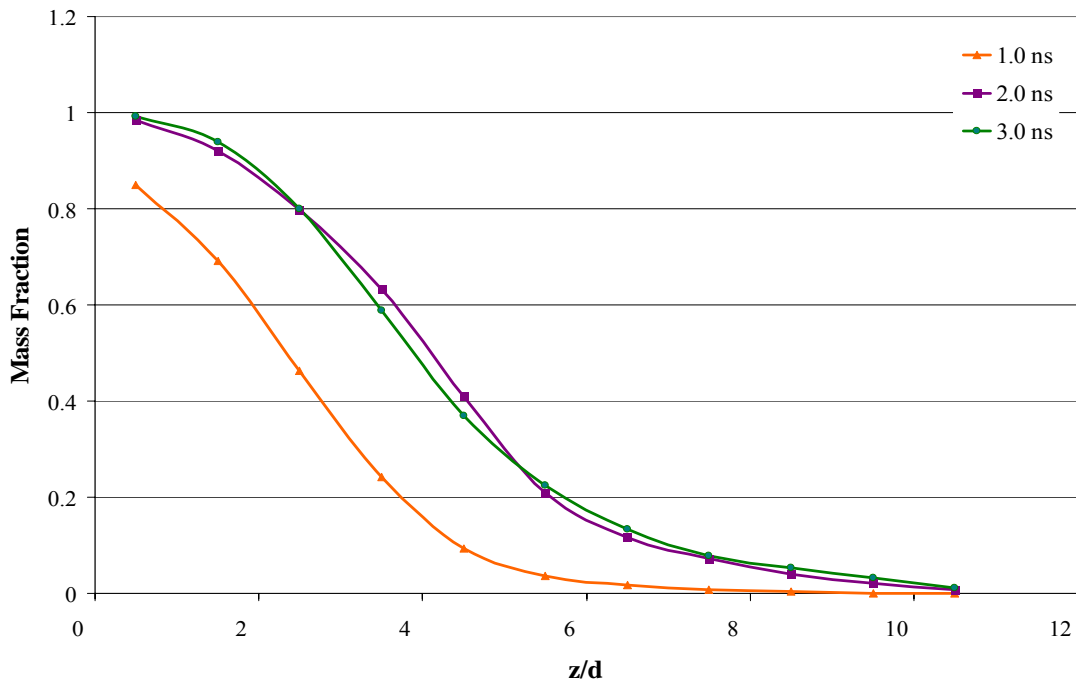


Figure 21. Mixing Along Centerline , $U_0 = 0$ m/s, Acoustic Free Model

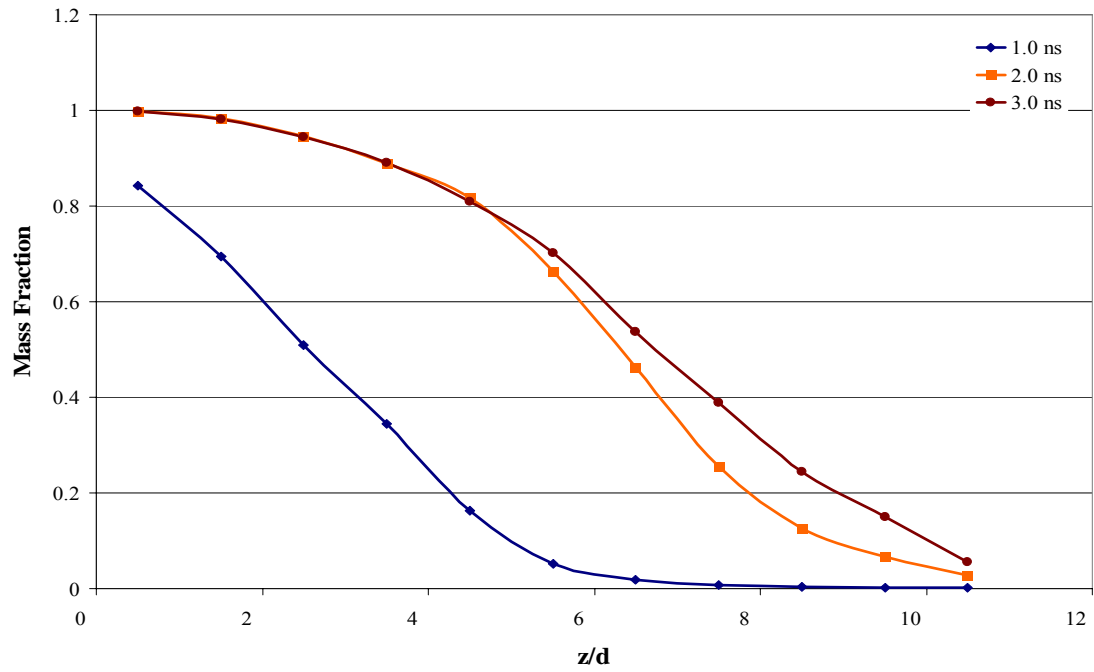


Figure 22. Mixing Along Centerline , $U_0=0$ m/s, Acoustic Interference Model

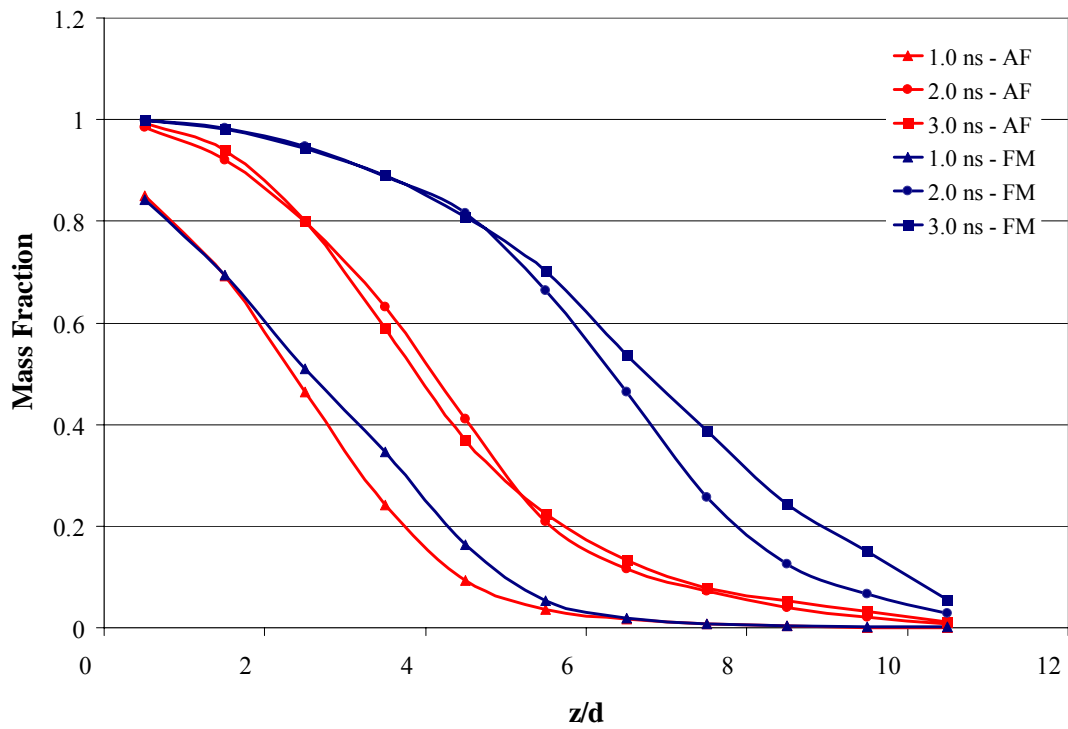


Figure 23. Mixing Along Centerline, Comparison of Acoustic Free Model vs. Acoustic Interference Model for $U_0=0$ m/s

Figure 24 shows the centerline mixing for the $U_o = 50$ m/s case at 1.0 ns for the acoustic free case. Presently, 1.0 ns is the extent of the data gathered for this case. This chart does not provide much data, but the data it does present is compared to other cases later in the section. Figure 25, which relates to the acoustic interference case for $U_o = 50$ m/s shows similar mixing as the flow develops over time. The mixing is again higher at 1.0 ns and decreases as it reaches 2.0 ns. This effect is attributed to the initial acceleration into the chamber. The flow develops as simulation time increases but the limited data shows the flow mixes better in the acoustic interference case than it does in the acoustic free case. The shape of the mixing curves in the acoustic free case through the chamber is similar to the acoustic interference but the mixing is definitely higher for the acoustic interference model. Figure 26 shows this comparison more clearly. For the earlier simulation times, it is clear the acoustic free mixing is lower.

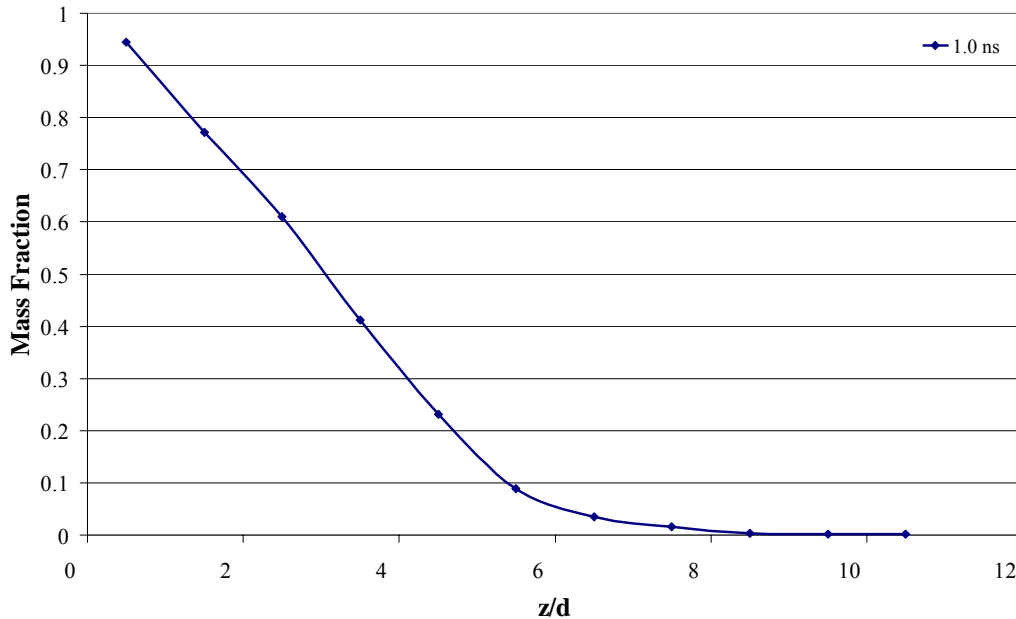


Figure 24. Mixing Along Centerline, $U_o=50$ m/s, Acoustic Free Model

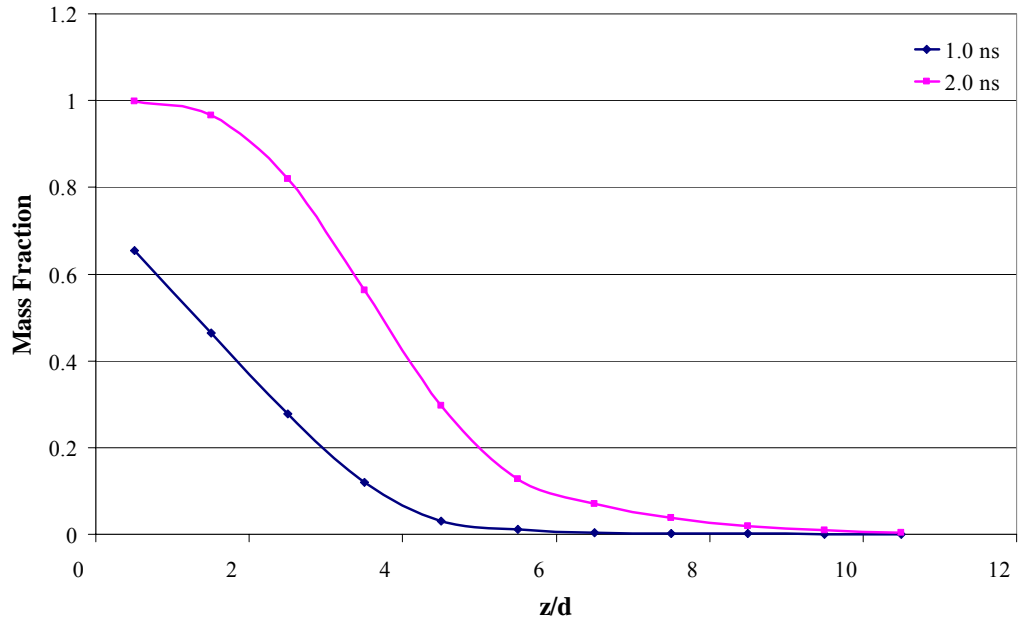


Figure 25. Mixing Along Centerline, $U_0=50$ m/s, Acoustic Interference Model

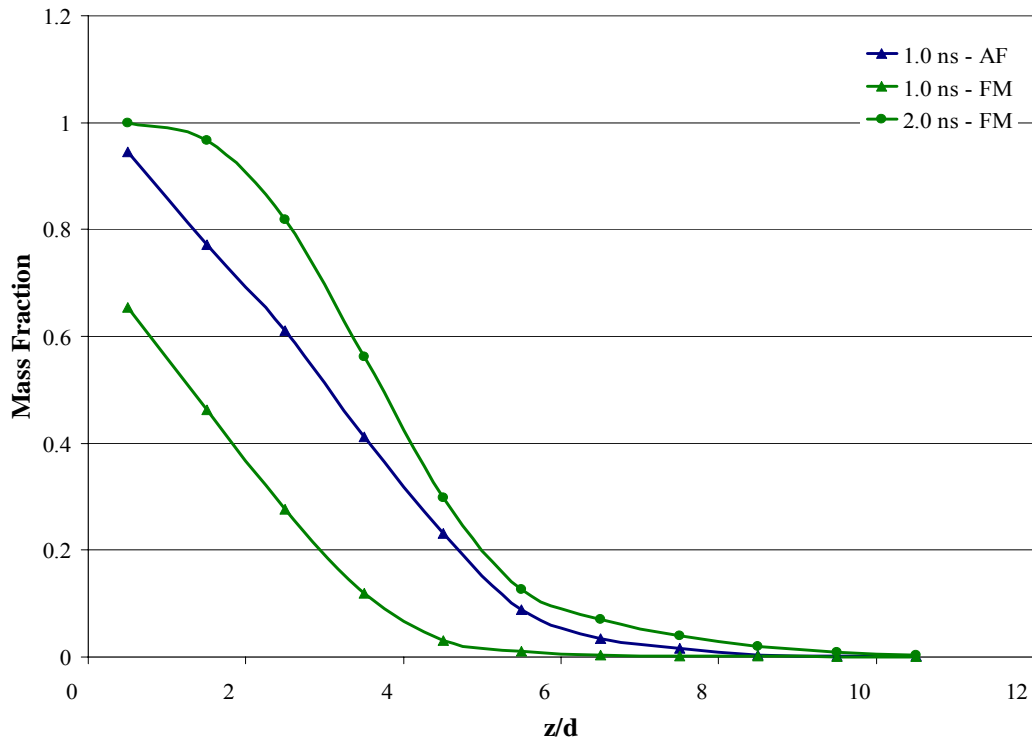


Figure 26. Mixing Along Centerline, Comparison of Acoustic Free Model vs. Acoustic Interference Model for $U_0=50$ m/s

Figures 27 to 29 relate to $U_o = 300$ m/s. The development of this flow closely resembles the development of the flow for $U_o = 50$ m/s. For the acoustic free case, the flow develops as expected with mass fraction increasing throughout the chamber as the simulation time increases. The acoustic interference case faces similar development. As the simulation time increases, mass fraction of the flow increases. The flow begins to exhibit some signs of possibly reaching a steady state flow as the simulation time moves into the 2.0 to 3.0 ns region. The mixing curves begin to level off and look very similar. The difference between the curves at this time may be due to the acoustic pressure wave being applied to the flow. This pressure could cause a continued fluctuation in mixing as the flow simulation time increases. Again, as in the $U_o = 50$ m/s case, the mass fraction in the acoustic free simulation is greater than seen in the acoustic interference case. Similar to what was observed for $U_o = 50$ m/s cases, as the simulation times increase the cases with and without acoustic interference show some correlation in mixing early in the chamber but seem to diverge as the flow moves further into the chamber, with the higher levels of mixing in the acoustic interference model.

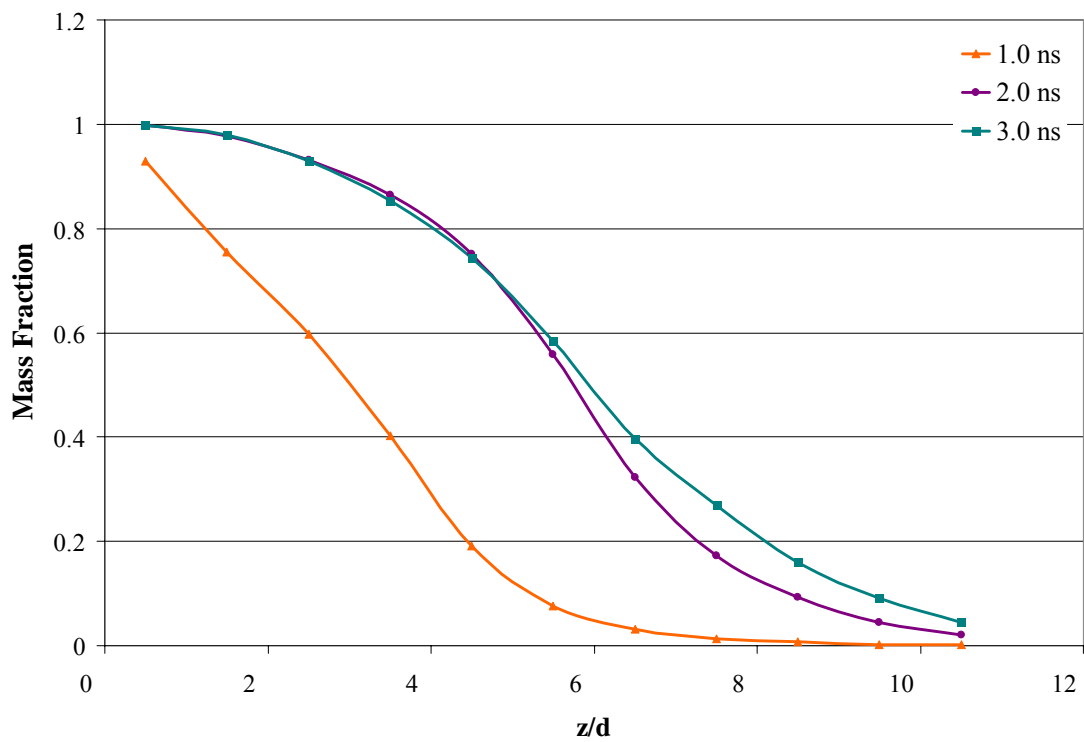


Figure 27. Mixing Along Centerline, $U_o=300$ m/s, Acoustic Free Model

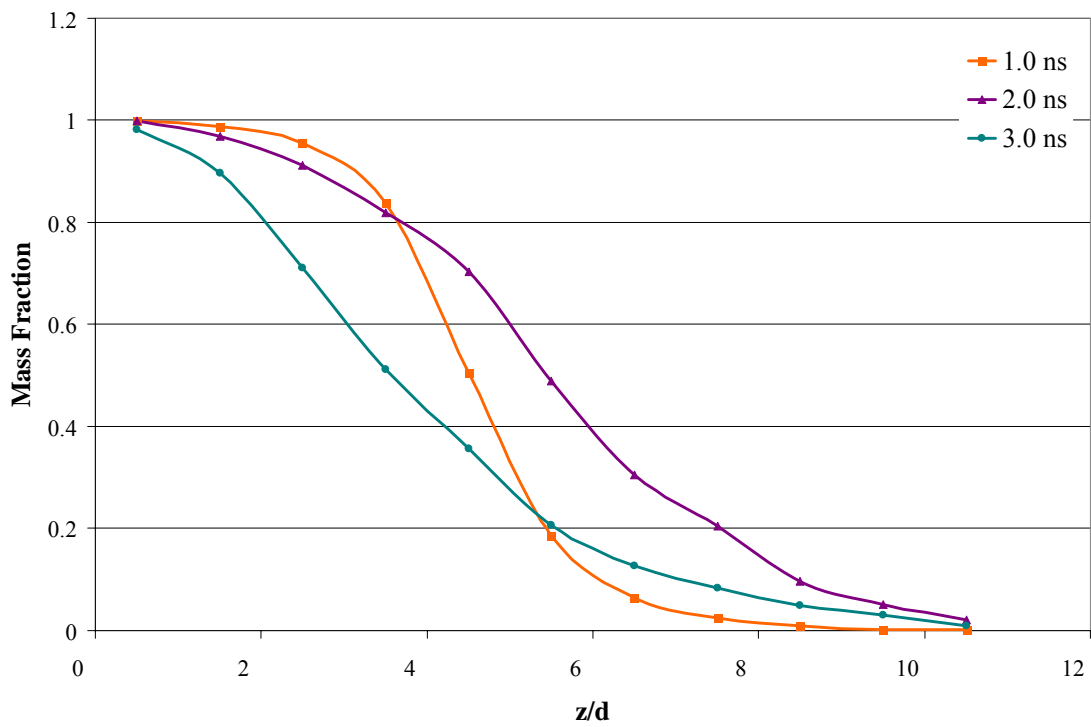


Figure 28. Mixing Along Centerline, $U_o=300$ m/s, Acoustic Interference Model

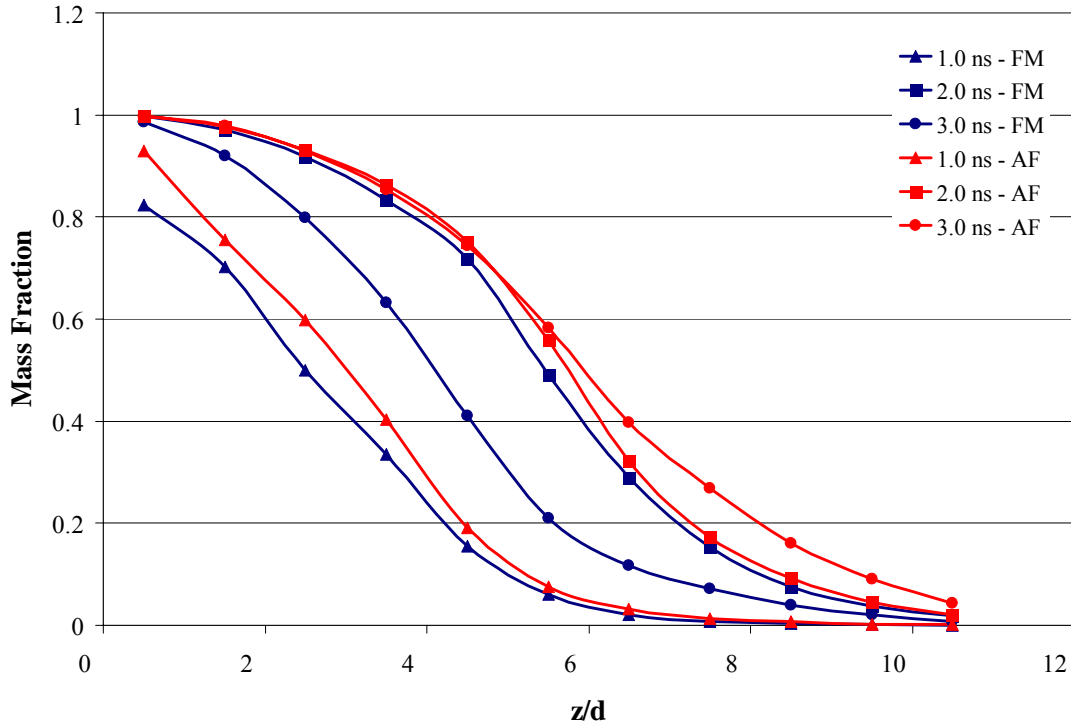


Figure 29. Mixing Along Centerline, Comparison of Acoustic Free Model vs. Acoustic Interference Model for $U_o=300$ ms

The following figures show comparisons of the different outer jet speeds and the effects of the speeds on the mixing in the flow. Figure 30 shows all three outer jet velocity cases at 1.0 ns for the acoustic free model. The first observation made is the $U_o = 50$ m/s and $U_o = 300$ m/s flows seem to exhibit very similar development at this time step as it will be seen throughout the entire simulation. The case of $U_o = 0$ m/s exhibits less injected mass in the acoustic free model. Looking at Figure 31, similar observations are expected once more data is collected. The $U_o = 50$ and 300 m/s cases should exhibit very close mass fractions. The additional mass being injected by the coaxial flow as well as the reduced shear forces on the jet should account for the higher mass fractions seen in the $U_o/U_i = 1$ and 6 cases.

Looking at the acoustic interference model, some interesting observations are made. For the flow at 1.0 ns seen in Figure 33, $U_o/U_i = 0$ and 6 cases appear to exhibit the same mixing in the chamber. The $U_o/U_i = 1$ case exhibits better mixing than the other two cases. At 2.0 ns (Figure 34), all cases begin to exhibit different levels of mixing throughout the chamber. Figure 35 shows as simulation time increases the mixing in the chamber for the $U_o = 0$ m/s and $U_o = 300$ m/s cases diverges even more. The mass fraction throughout the chamber at 3.0 ns is higher for $U_o = 0$ m/s than it is for $U_o = 300$ m/s, as one would expect, due to the higher shearing force the coaxial flow places on the core jet flow.

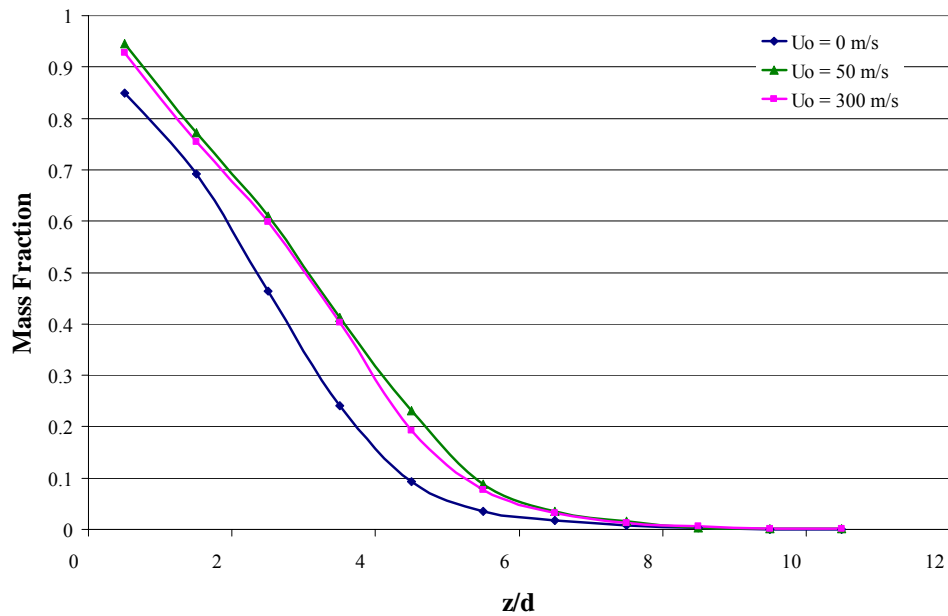


Figure 30. Mixing Along Centerline, Comparison at 1.0 ns for Acoustic Free Model

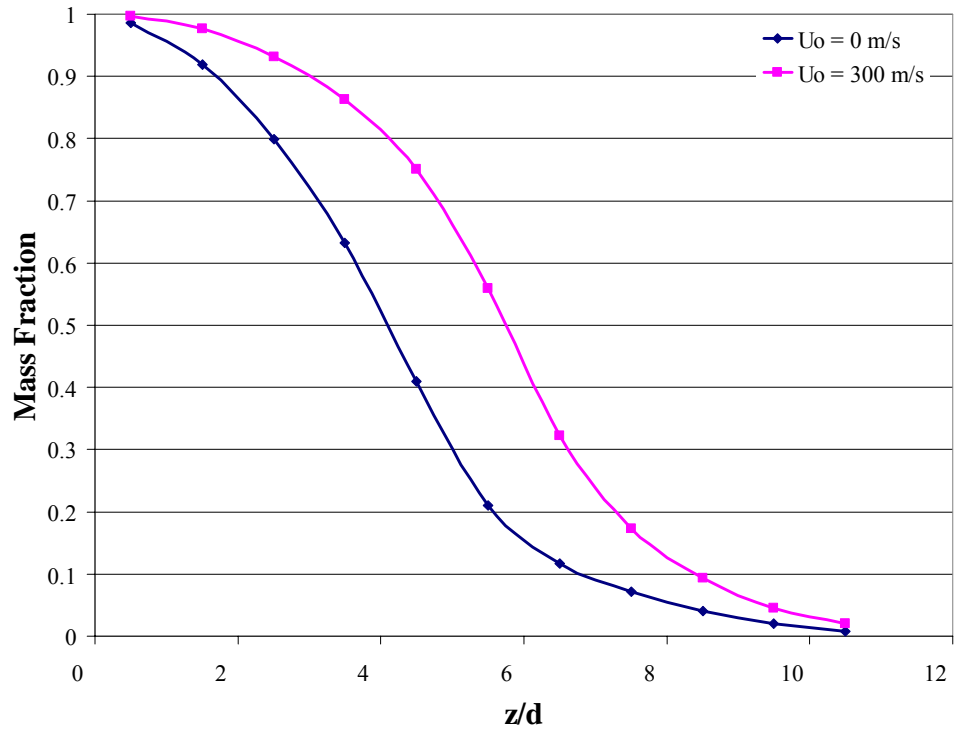


Figure 31. Mixing Along Centerline, Comparison at 2.0 ns for Acoustic Free Model

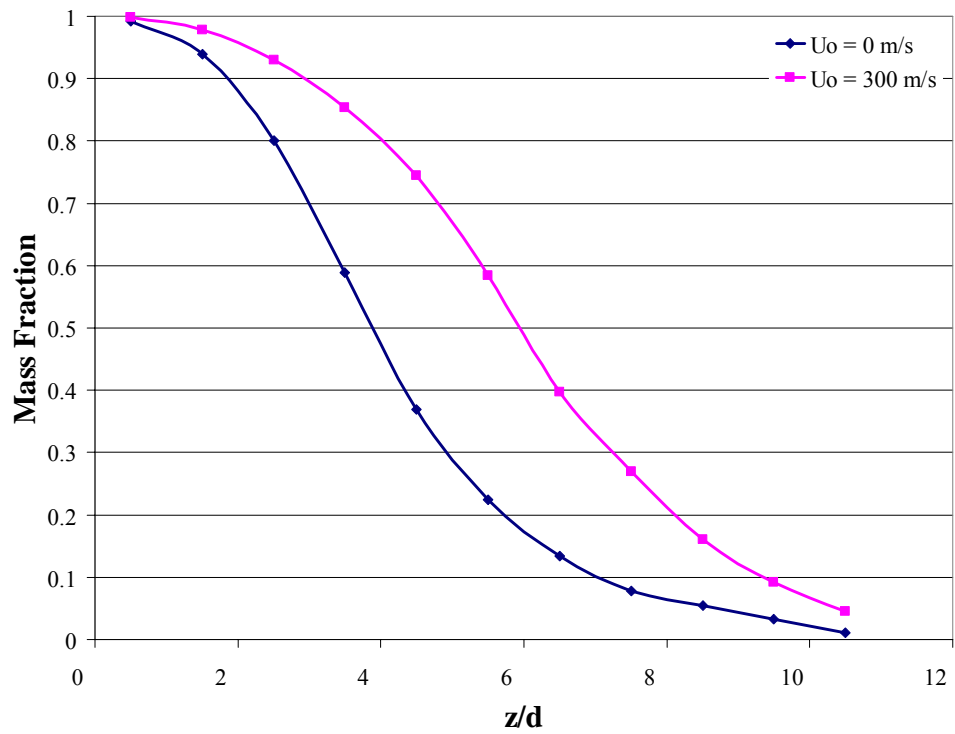


Figure 32. Mixing Along Centerline, Comparison at 3.0 ns for Acoustic Free Model

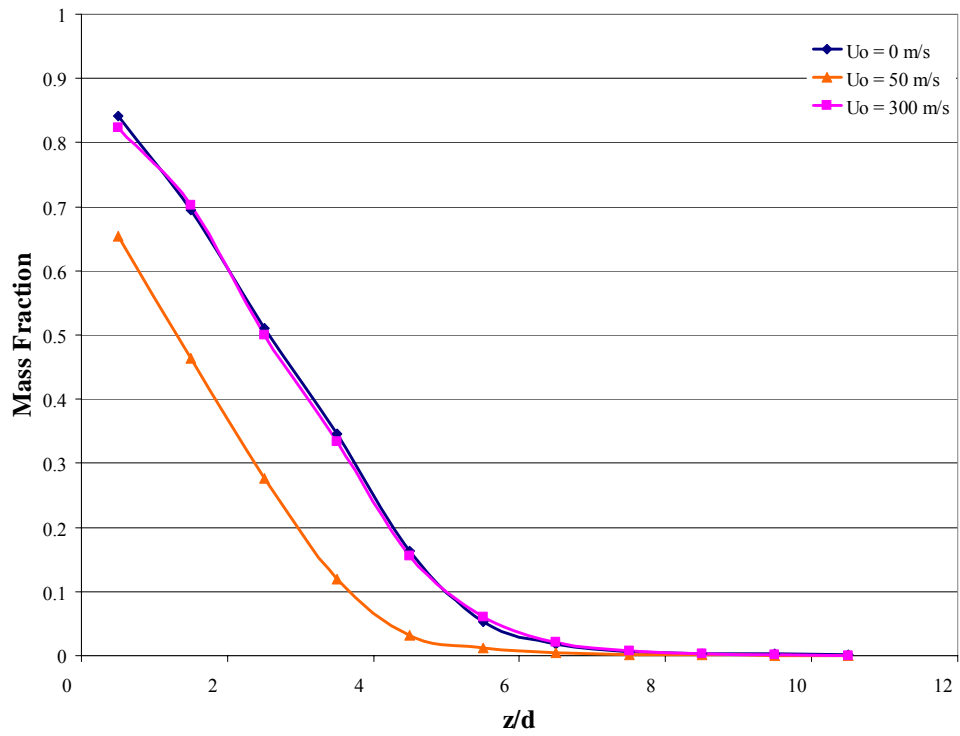


Figure 33. Mixing Along Centerline, Comparison at 1.0 ns for Acoustic Interference Model

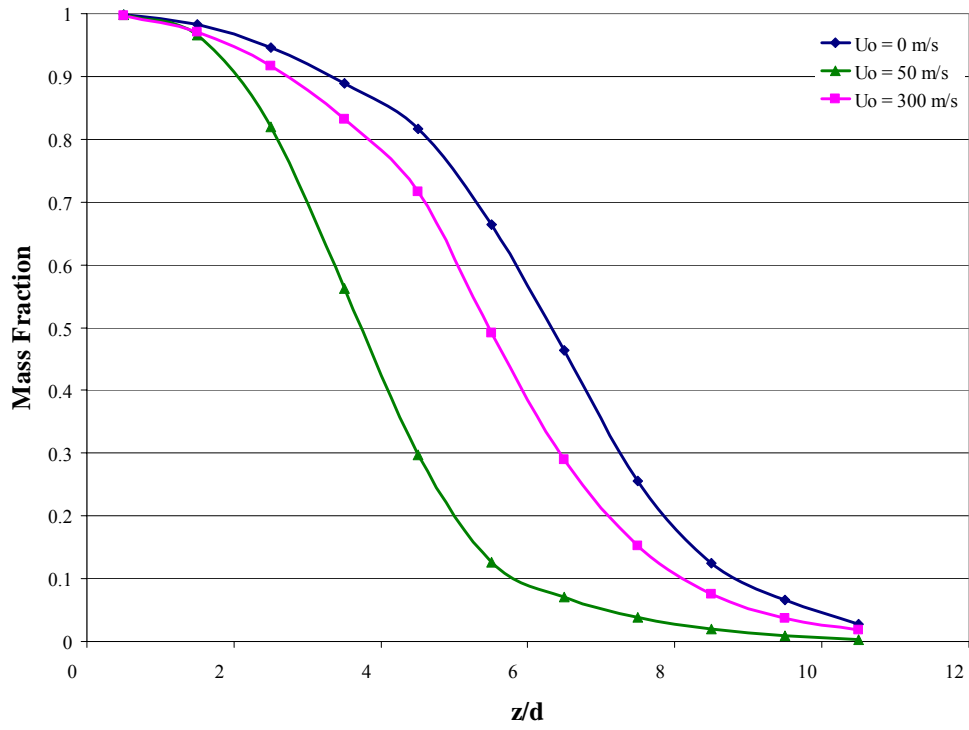


Figure 34. Mixing Along Centerline, Comparison at 2.0 ns for Acoustic Interference Model

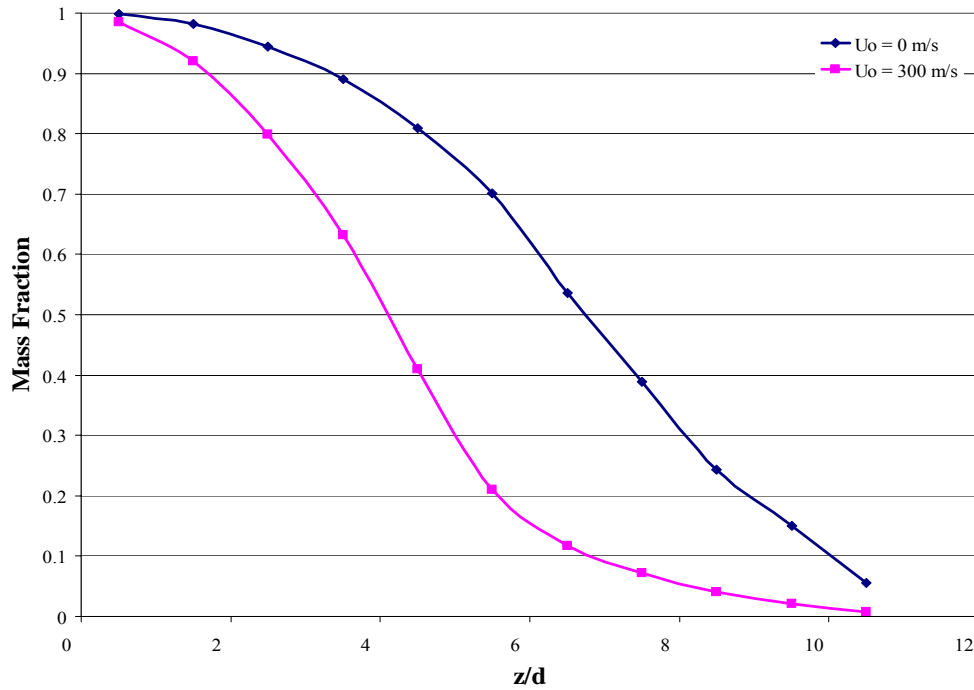


Figure 35. Mixing Along Centerline, Comparison at 3.0 ns for Acoustic Interference Model

Radial Density Profile

The radial density profile data provides some insight into the shape of the jet and its issuance into the chamber. This data is similar to that of a jet shadowgraph. The first simulation discussed is the single jet with no coaxial component. Again, the inner tube velocity for all cases is set at 50 m/s. Figure 37 shows the acoustic free model of the jet soon after it begins issuing into the chamber. The x-axis, labeled r/d , is a non-dimensionalized variable equal to the radial chamber position divided by the tube diameter. The y-axis represents a density ratio calculated as

$$\text{Density Ratio} = \frac{\rho_x - \rho_c}{\rho_t - \rho_c} \quad (51)$$

The t and c subscripts refer to tube and chamber, respectively.

At $z/d = 0$, jet exit plane, the first sign of tube particles issuing into the chamber can be seen. The density ratio is expected to be close to 1.0 but does not reach this level (Figure 36). The problem is most likely due to an error in the code. Particles are not being added to the flow at the expected levels, which is decreasing the density ratio seen in the chamber. In order to examine the radial density profiles the data needs to be scaled. All radial density curves are scaled to the first point near the exit plane. The scaling places the first data point at 1.0, and scales all other points in accordance. Figure 37 shows the scaled data that appeared in Figure 36. The first curve reaches unity as initially expected. Further into the chamber at $z/d = 1$, the presence of particles can be seen but not at the levels of the density seen at the jet exit. Moving further into the tube, there is a negligible density change. The density ratio is also largest at the center of the jet and decreases as it moves away from the center of the chamber as expected. Figure 38 shows the acoustic

free single jet flow 2.0 ns into the flow and 1.0 ns after the events in Figure 37. The jet is issuing further into the chamber as the density ratio further into the chamber has increased considerably. The expected jet growth is clearly apparent as time progresses. The density ratio steadily decreases and becomes negligible at $z/d = 4$. Due to the scaling, the density ratio at all sections of the chamber can be compared in a similar manner. The jet is changing significantly up to 2.0 ns. The difference in density ratios between 2.0 and 3.0 ns near the exit are quite small. Greater differences are seen in density ratio between $z/d = 2$ and $z/d = 4$. Though changes are taking place, the density ratios seem to be very comparable early in the jet and it leads to the conclusion the jet is moving towards steady state.

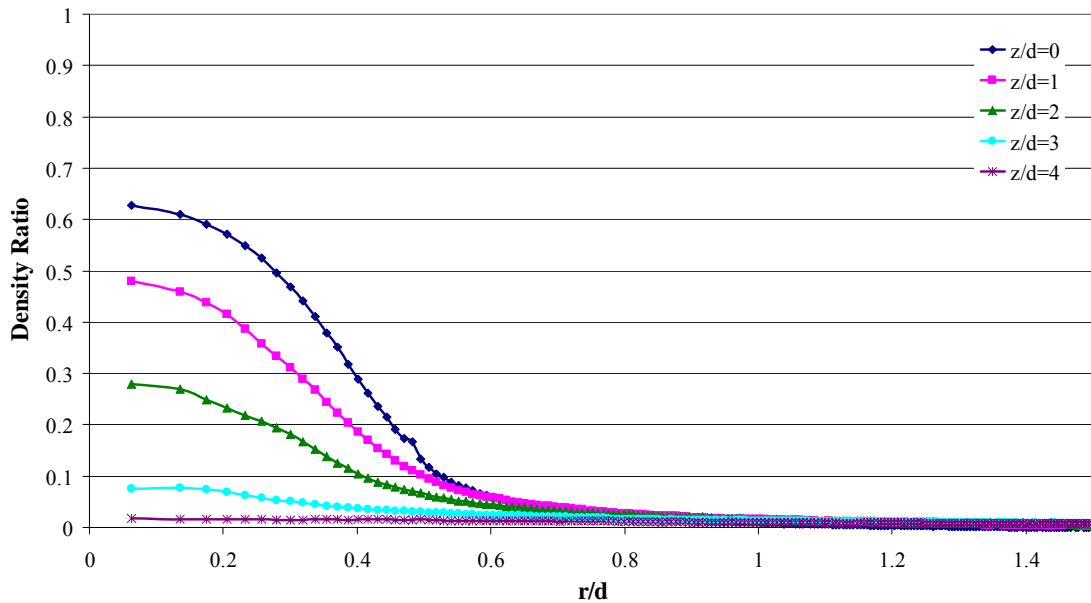


Figure 36. Radial Density Profile at 1.0 ns without Scaling, $U_o = 0$ m/s, Acoustic Free Model

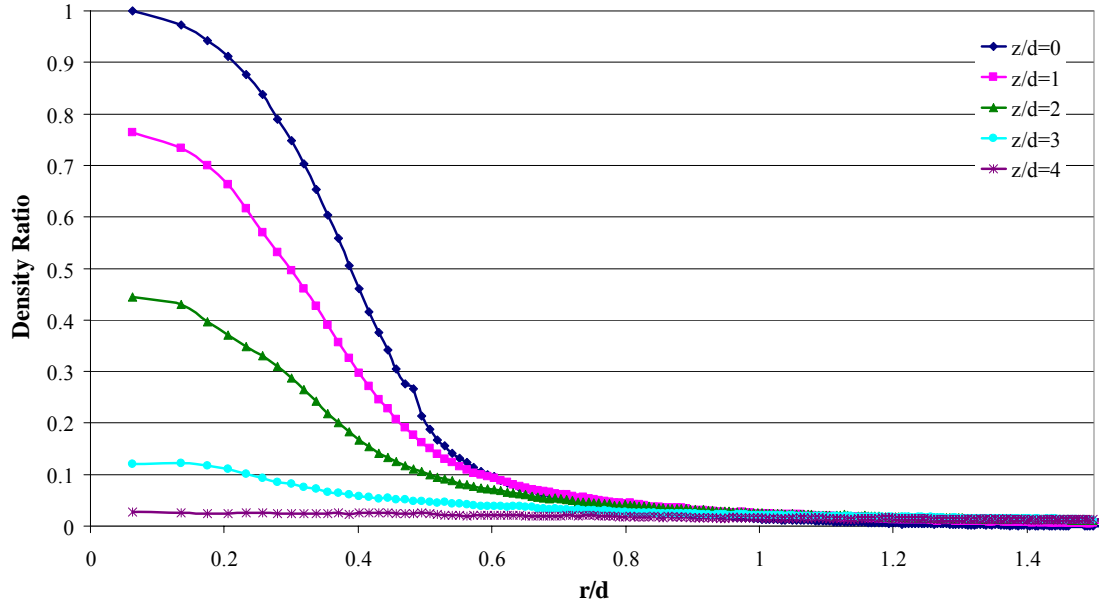


Figure 37. Radial Density Profile at 1.0 ns, $U_o = 0$ m/s, Acoustic Free Model

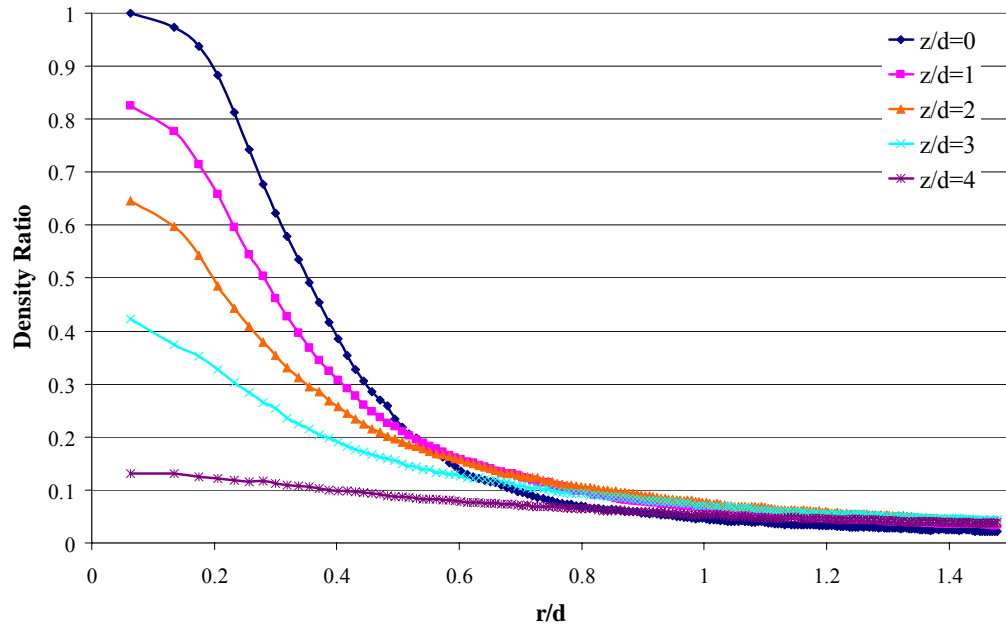


Figure 38. Radial Density Profile at 2.0 ns, $U_o = 0$ m/s, Acoustic Free Model

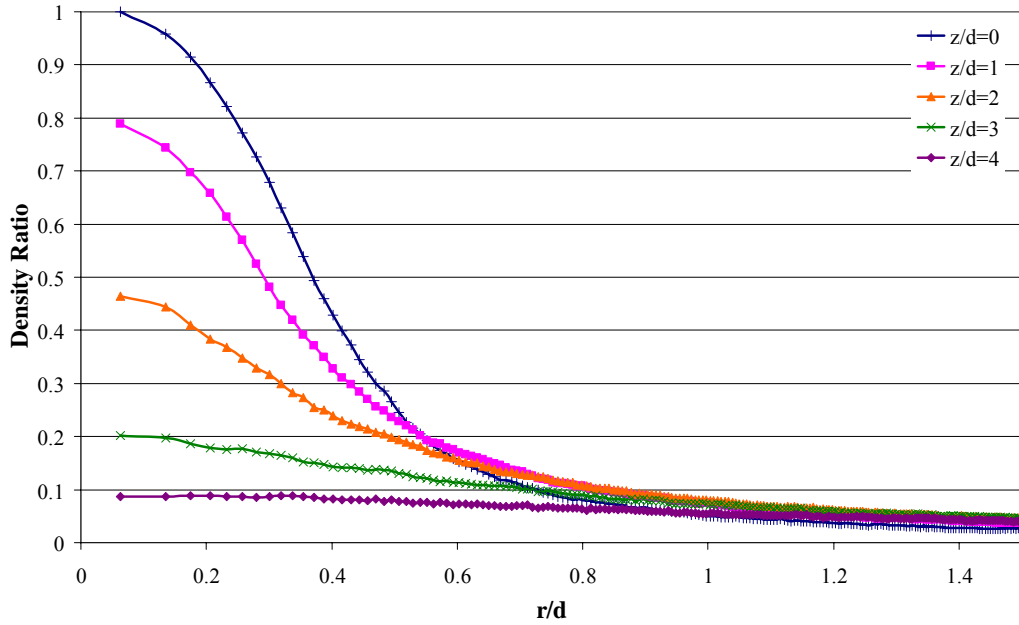


Figure 39. Radial Density Profile at 3.0 ns, $U_o = 0$ m/s, Acoustic Free Model

The time development of the density ratio follows the results in the velocity profiles and mass fraction charts. Figures 40, 41, and 42 show the time progression of density at $z/d = 0, 1$, and 2 respectively. The time progression shows an initial large influx of particles into the chamber for the first 1.0 ns, with a decline to a steady state in the times thereafter. The mass fraction time profile is similar, with mixing ramping to large levels in the first 1.0 ns and then decreasing before leveling off around 3.0 ns. There is also some correlation with the velocity profile. The flow seems to have some initial acceleration in the tube but the flow begins to decelerate until it reaches a velocity close to the theoretical velocity.

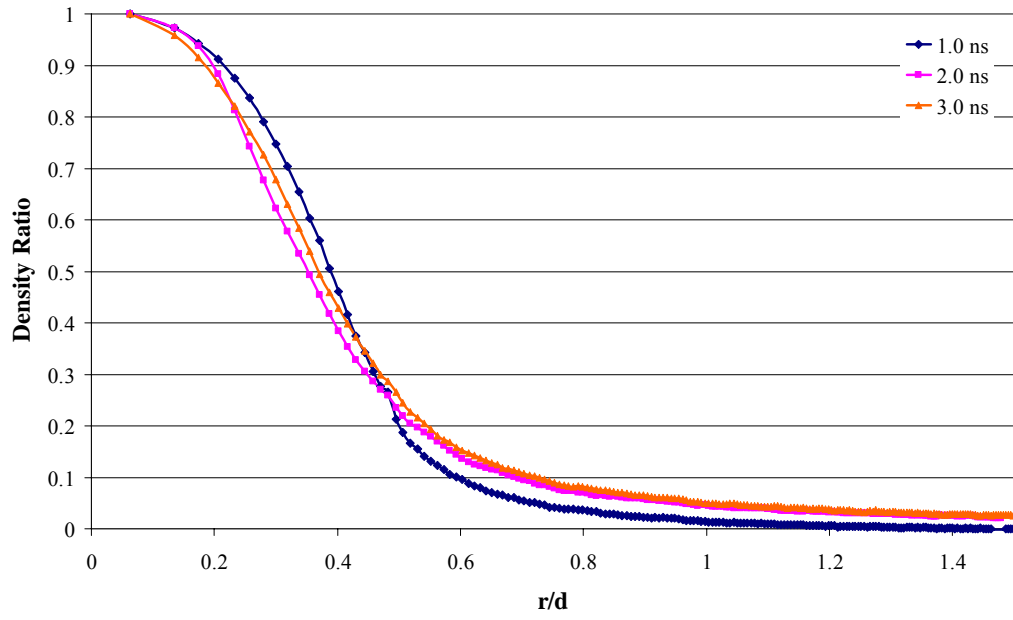


Figure 40. Radial Density Profile at $z/d = 0$, $U_0 = 0$ m/s, Acoustic Free Model

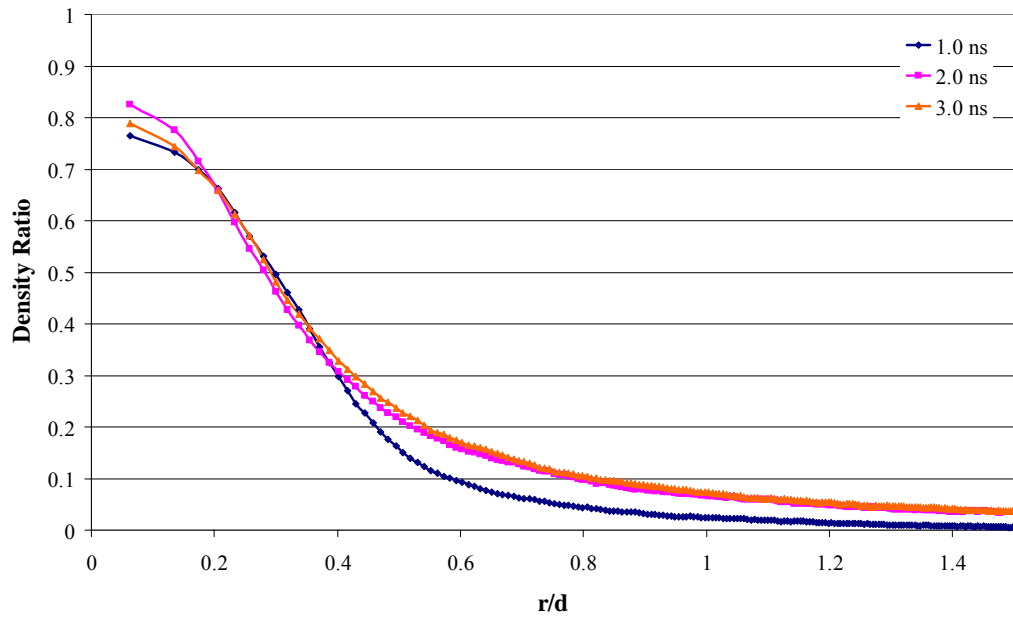


Figure 41. Radial Density Profile at $z/d = 1$, $U_0 = 0$ m/s, Acoustic Free Model

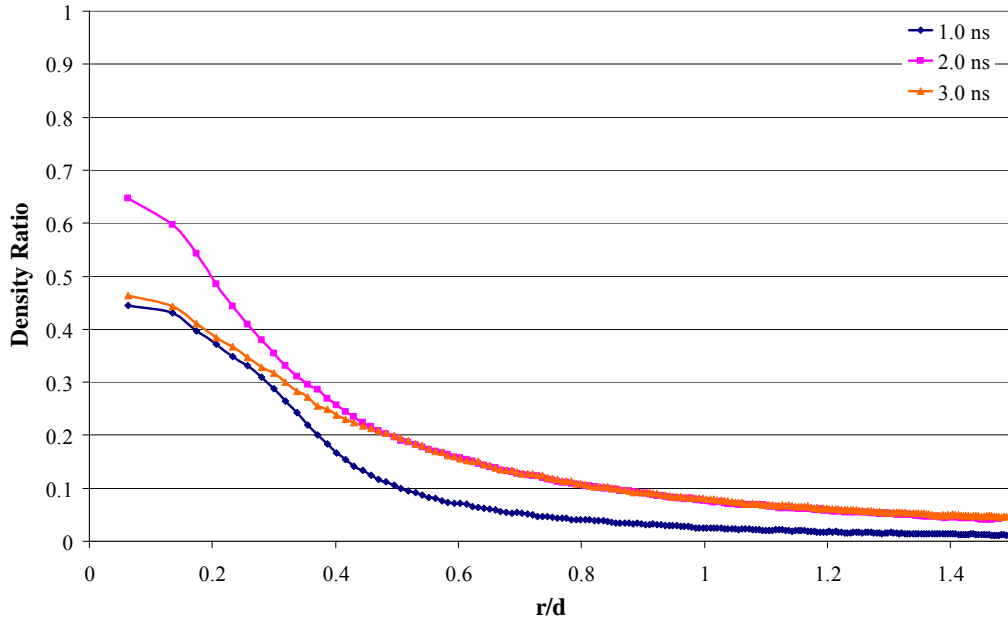


Figure 42. Radial Density Profile at $z/d = 2$, $U_o = 0$ m/s, Acoustic Free Model

Looking at the acoustic interference case for $U_o = 0$ m/s, similar trends can be seen.

Figure 43 shows the density progression at 1.0 ns. The acoustic interference model does have higher density ratios than the acoustic free model further into the chamber. Figures 43, 44, and 45 represent 1.0, 2.0 and 3.0 ns after the start of the flow simulation. The radial density for the acoustic interference model follows the same time progression as seen in the acoustic free model. The biggest observable difference is the higher density ratios at each section of the chamber exhibited with the acoustic interference model.

Figures 46 and 47 represent time progression at $z/d = 0$ and $z/d = 3$ in the chamber. The progression follows closely to the acoustic free model. Again, the density ratio increases as time grows to approximately 2.0 ns. At this point, the density ratio begins to decrease until it begins to approach a steady state flow at 3.0 ns.

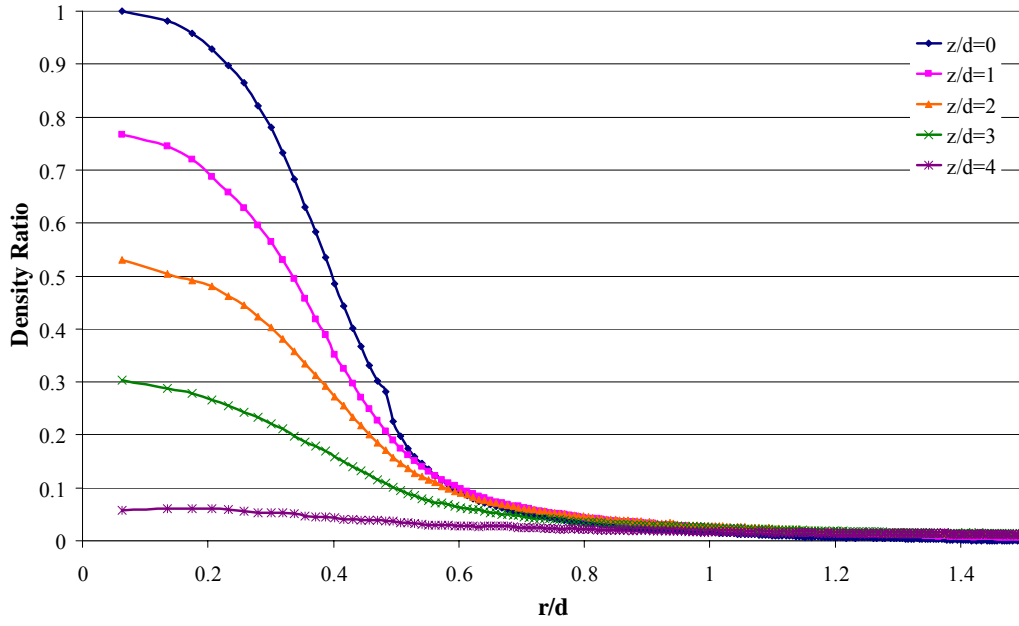


Figure 43. Radial Density Profile at 1.0 ns, $U_0 = 0$ m/s, Acoustic Interference Model

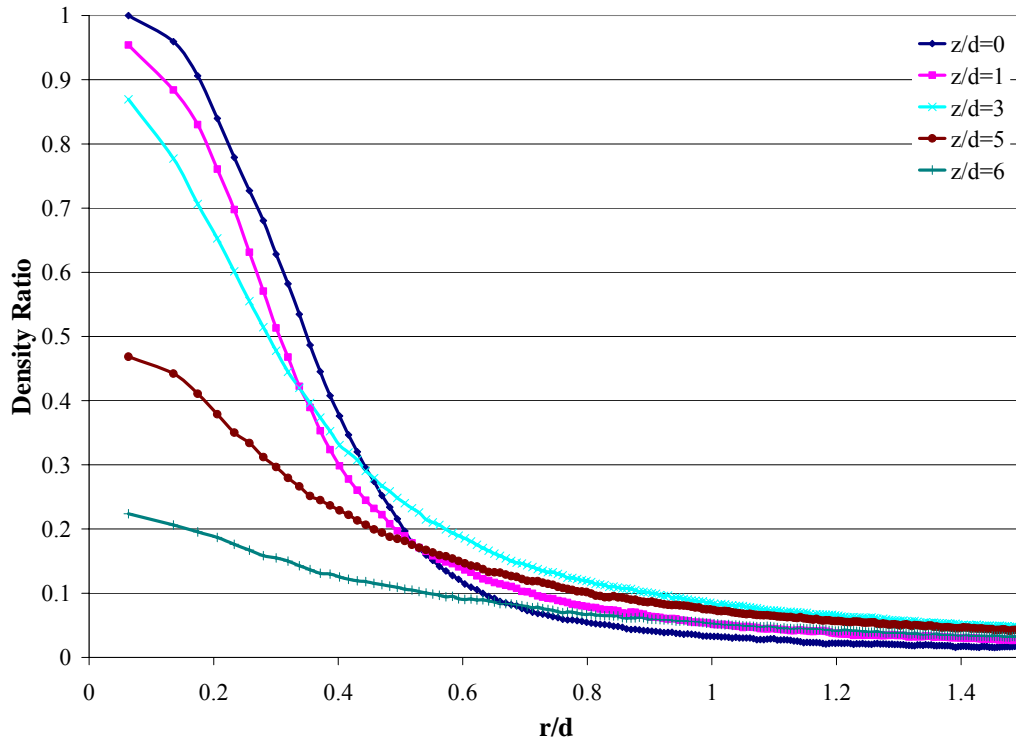


Figure 44. Radial Density Profile at 2.0 ns, $U_0 = 0$ m/s, Acoustic Interference Model

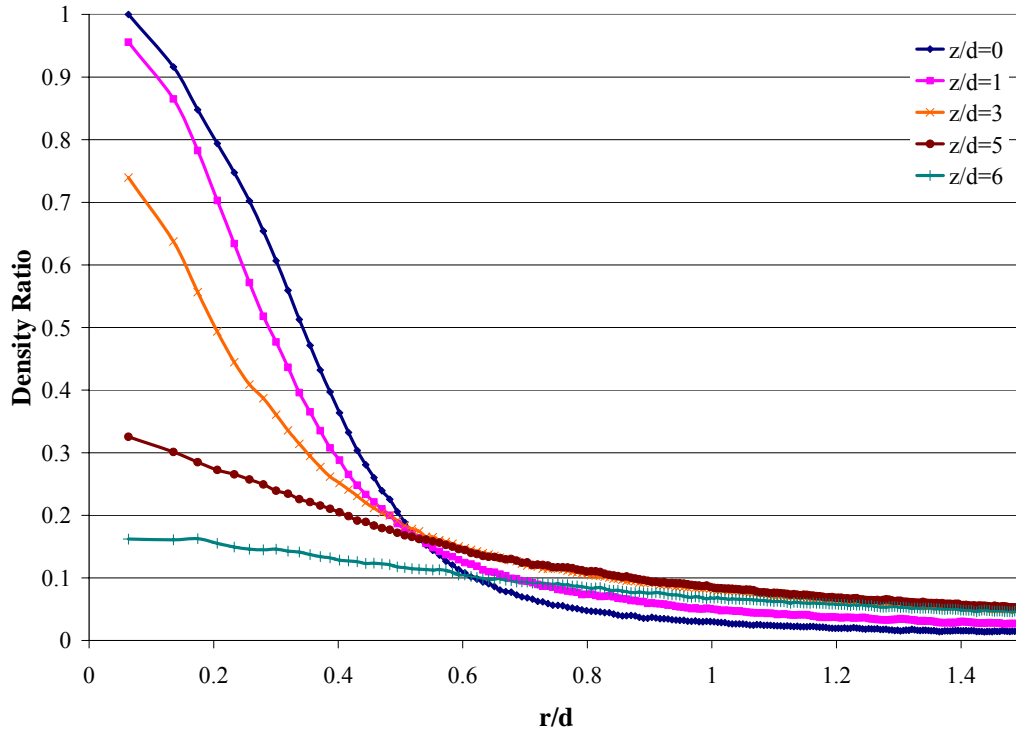


Figure 45. Radial Density Profile at 3.0 ns, $U_o = 0$ m/s, Acoustic Interference Model

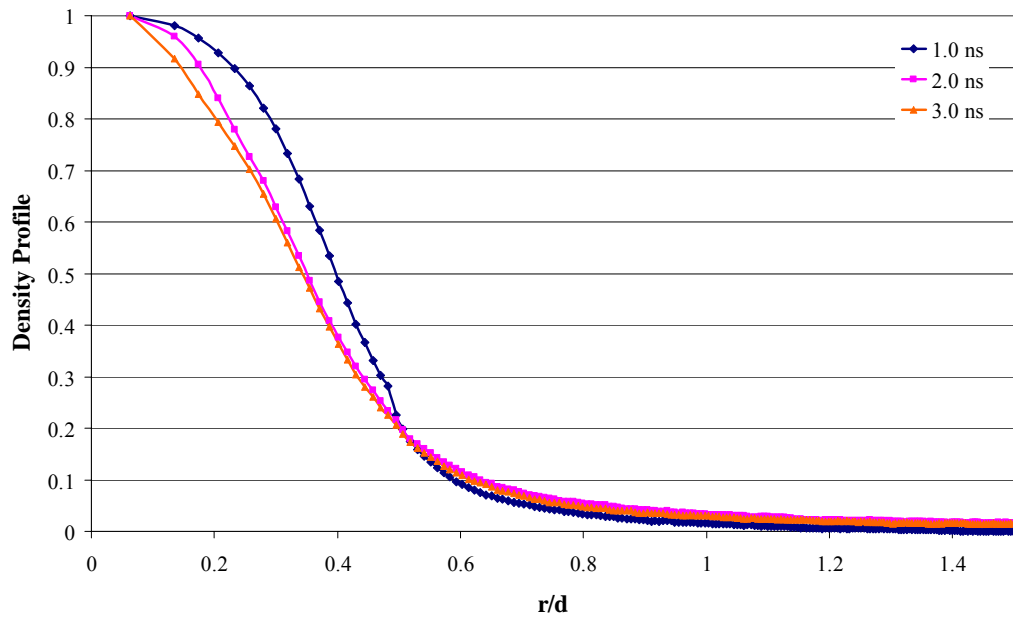


Figure 46. Radial Density Profile at $z/d=0$, $U_o = 0$ m/s, Acoustic Interference Model

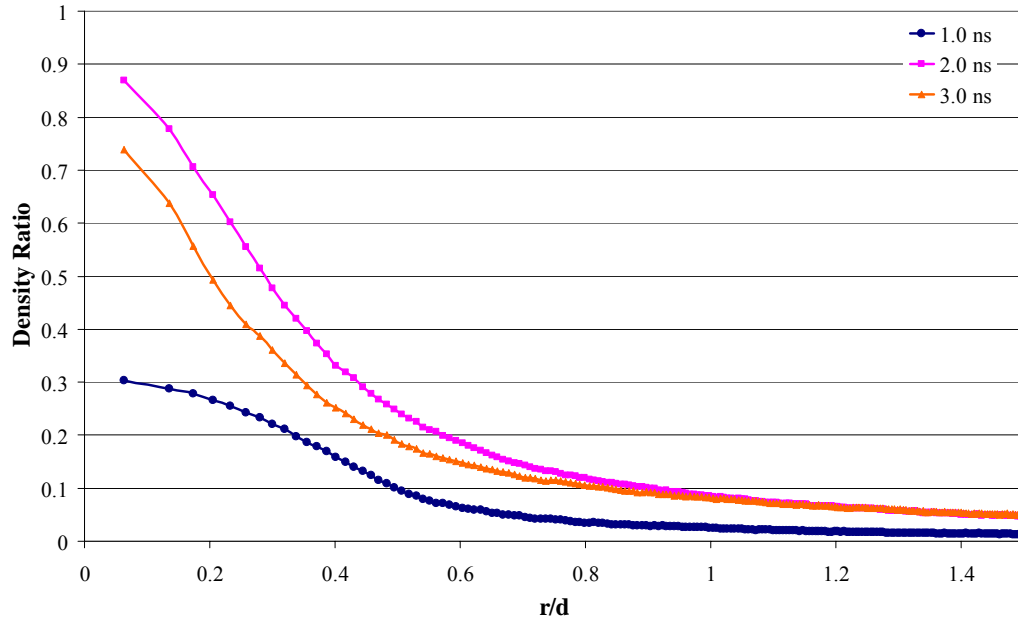


Figure 47. Radial Density Profile at $z/d=3$, $U_o = 0$ m/s, Acoustic Interference Model

Examining the affects of the acoustic interference on the shape of the jet requires side-by-side comparisons of each model to determine what part acoustic interference plays in the jet shape. Figures 48 to 50 show head-to-head comparisons of the single jet flow at 1.0, 2.0, and 3.0 ns respectively. At each period, the acoustic interference model shows higher density ratios. Looking at the work of Davis (2006:94), close comparisons can be visually drawn. Figure 51 shows experimental work studying the effects of acoustic interference on a coaxial jet. Looking at the first column in Figure 51, the jet in frame ‘a’ has no acoustic interference and maintains the shape expected. Frame ‘e’ shows the same jet with acoustic interference added. The first observation is the jet has become radially thicker. The jet also has become more unstable and does not hold its shape as well as the acoustic free jet. The experimental results suggest wider density profiles at lower values when acoustic interference is present. The acoustic interference simulations are showing higher density ratios in the radial axis. The density ratios for the acoustic interference

simulations also show higher density ratios than the acoustic free model further into the chamber. These results do not seem to match the experimental results seen but are most likely explainable by the jet shape and discrete particle models not operating within the physics of the problem.

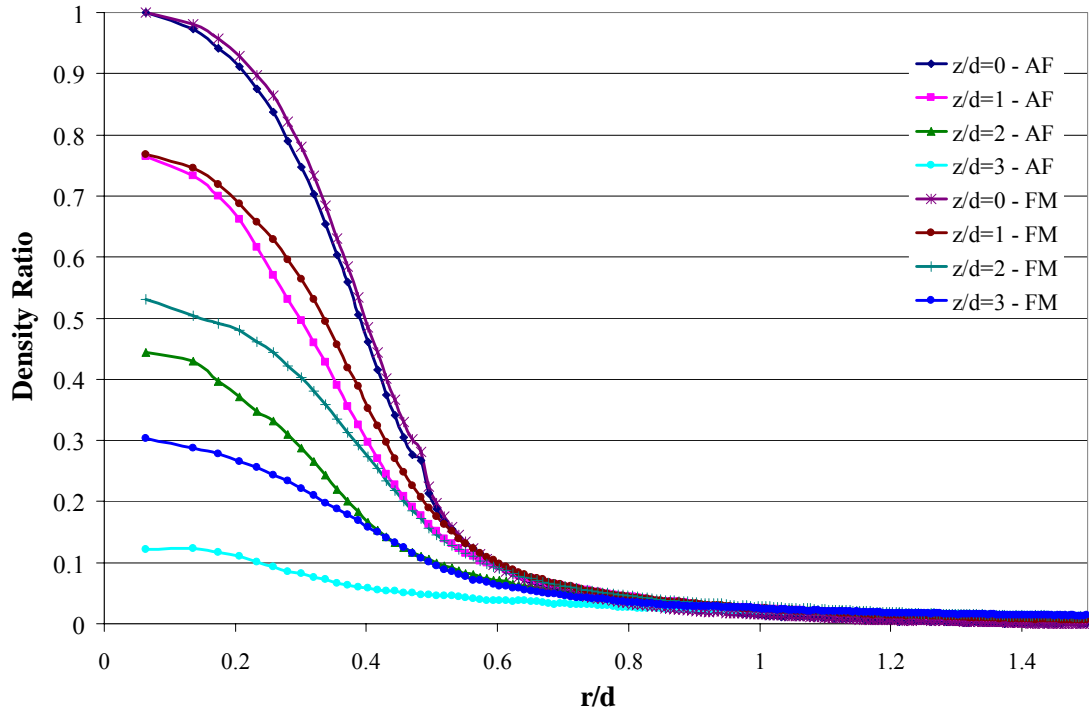


Figure 48. Radial Density Profile Comparison, $U_o = 0$ m/s, 1.0 ns, Acoustic Free (AF) Model and Acoustic Interference Model

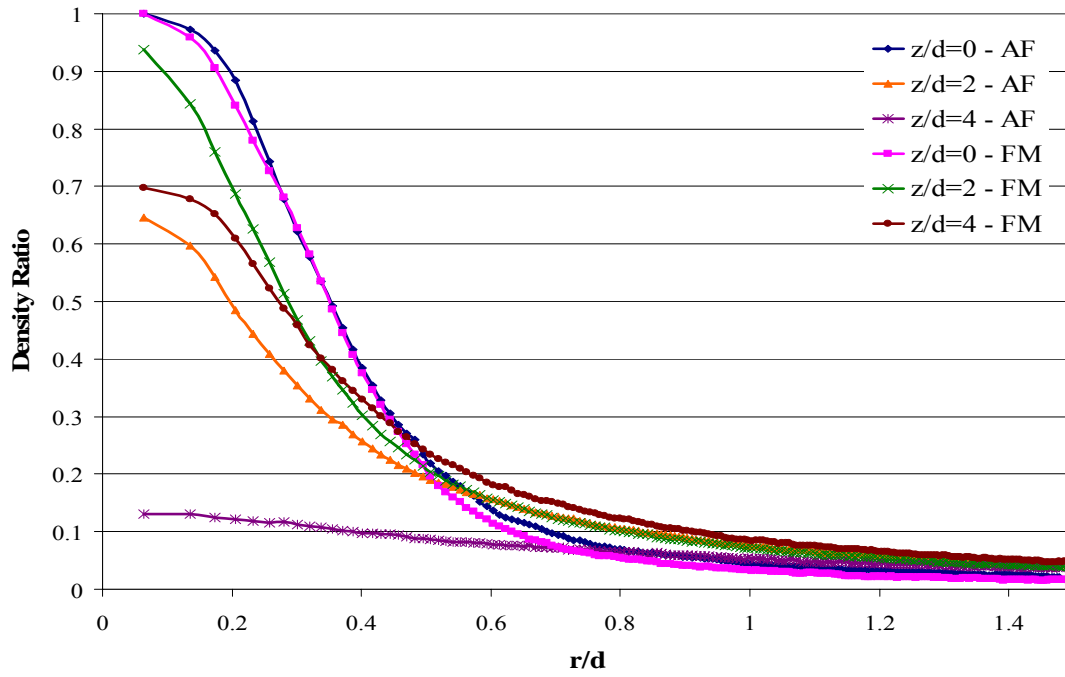


Figure 49. Radial Density Profile Comparison, $U_o = 0$ m/s, 2.0 ns, Acoustic Free (AF) Model and Acoustic Interference Model

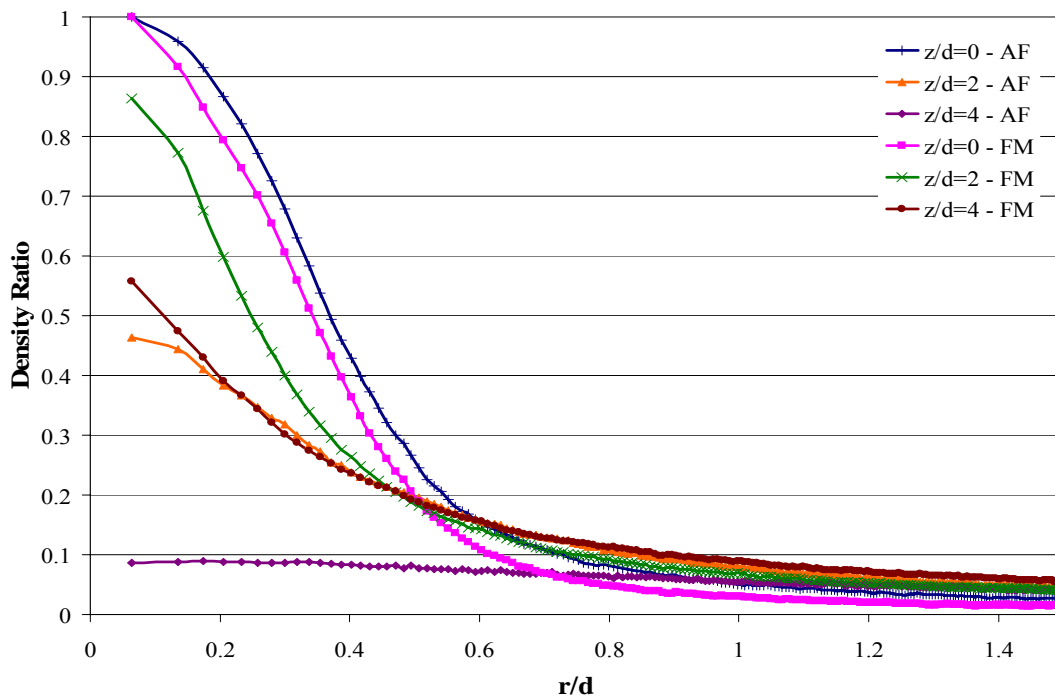


Figure 50. Radial Density Profile Comparison, $U_o = 0$ m/s, 3.0 ns, Acoustic Free (AF) Model and Acoustic Interference Model

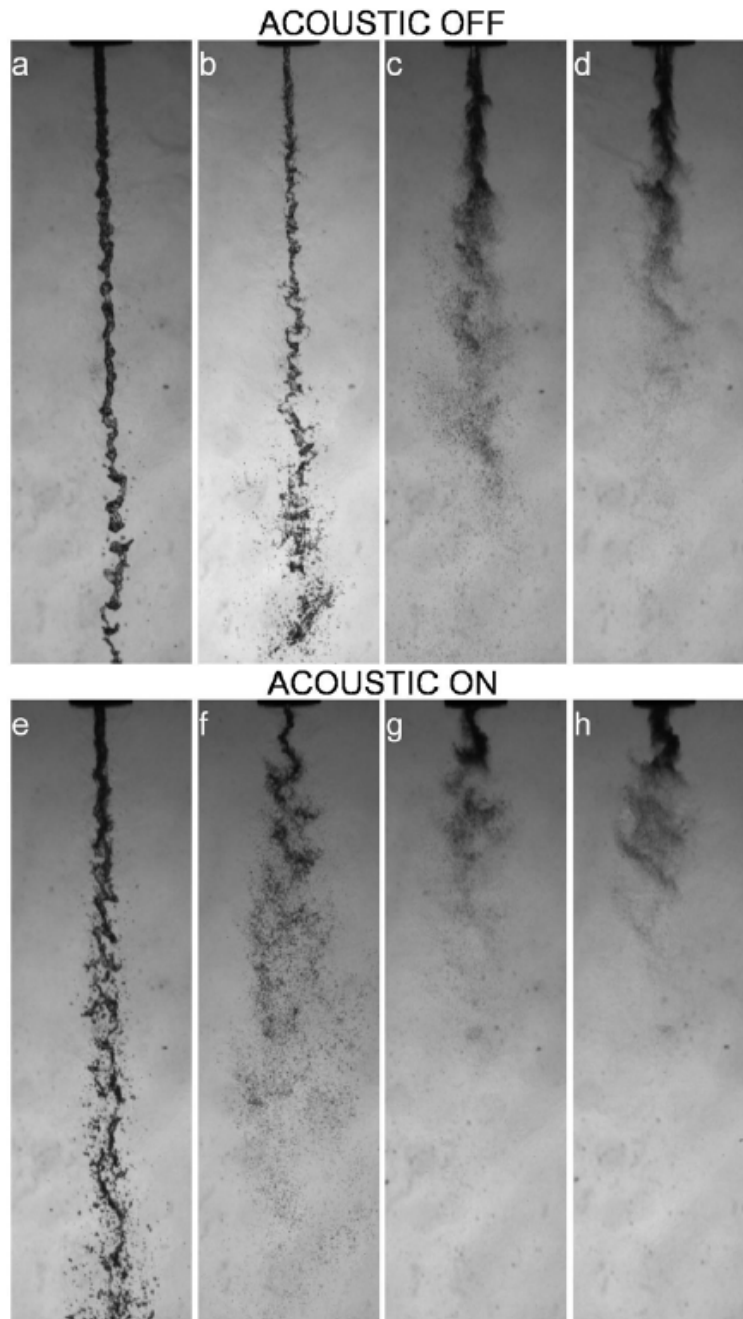


Figure 51. Shadowgraph images of coaxial jet at subcritical chamber pressure ($\sim 1.5\text{MPa}$) and at the high outer-jet temperature ($\sim 190\text{K}$) corresponding to cases 1 – 4 ($U_o/U_i = \sim 1$, ~ 2.5 , ~ 5 , and ~ 6.5). The acoustic driver is off for images in the top row and on for the bottom row at $\sim 3\text{ KHz}$. The velocity ratio is the same for each column and increases from left to right. (Davis, 2006:94)

Figure 52 shows the density profiles for the $U_0 = 50$ m/s with acoustics turned off. The development matches closely what is seen in the previous case. Again, the data collected are very preliminary for this case and speaking to the development of the acoustic free case is not feasible. Some comparisons can be made between the acoustic free and acoustic interference cases early in the flow. These results follow later in this section.

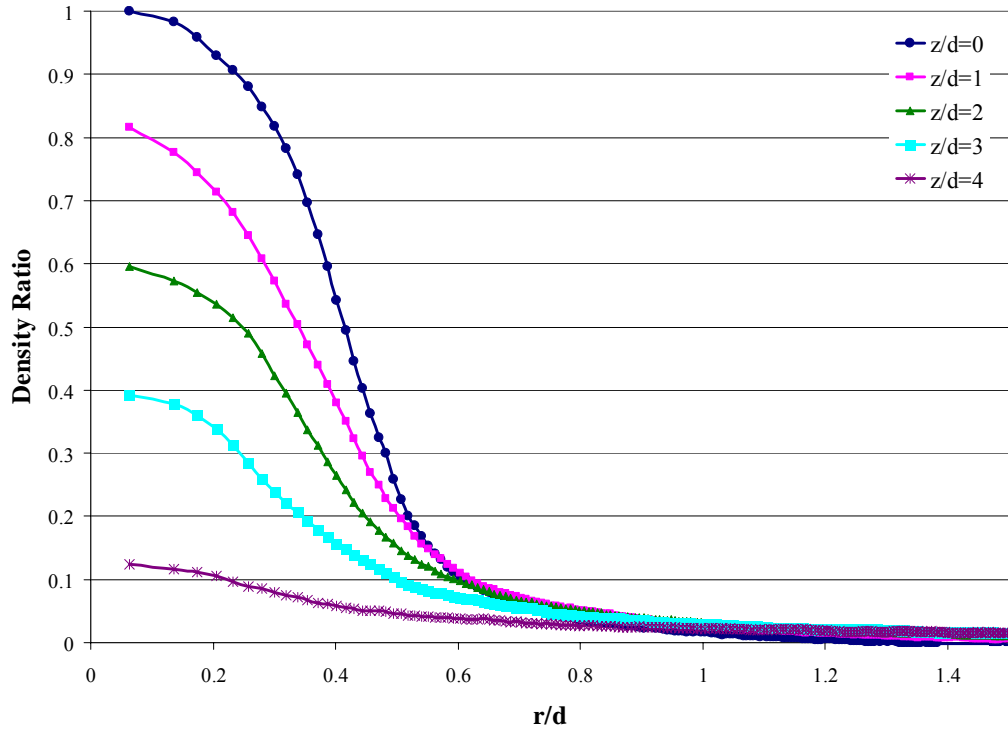


Figure 52. Radial Density Profile, 1.0 ns, $U_0 = 50$ m/s, Acoustic Free Model

Figures 53 and 54 show density ratio development of the acoustic interference case for $U_0 = 50$ m/s. The density ratio is developing similar to what was seen in the $U_0 = 0$ m/s case. The density ratios are increasing up to 2.0 ns and the flow is moving further into the chamber. Figure 53 shows a data point that doesn't follow a smooth trend for the $z/d = 0$ line. The data point, at a value of $r/d = 0.5$, is most likely due to a data collection

error since the point does not exist in similar charts at different velocity ratios. More data is necessary to assure that the flow is moving towards a steady state.

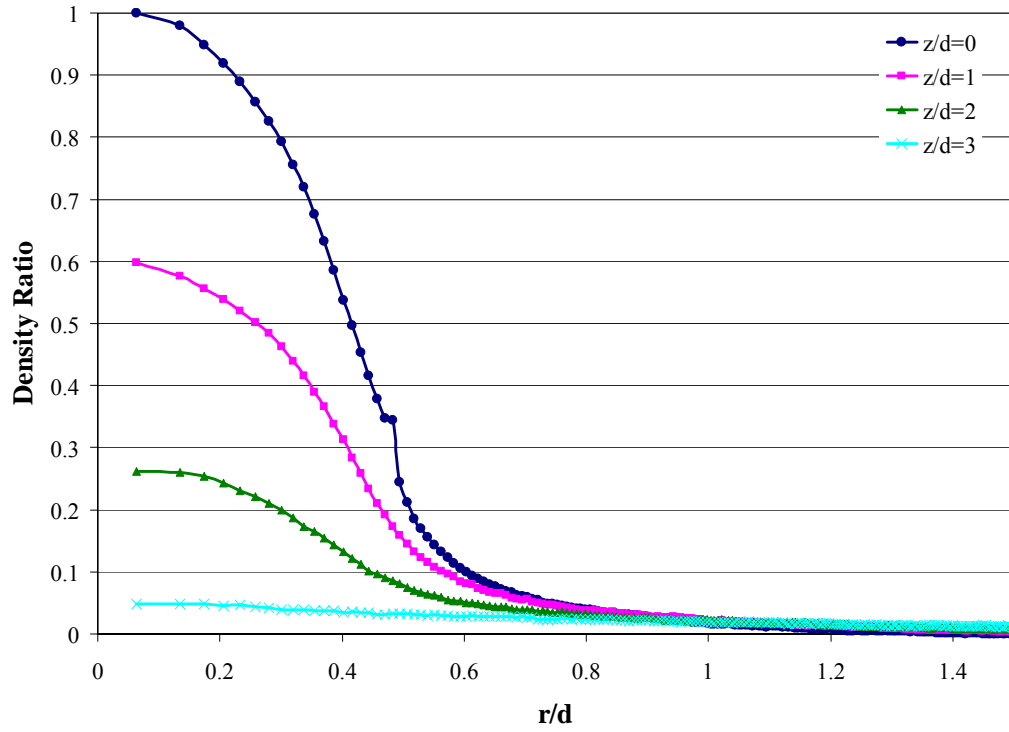


Figure 53. Radial Density Profile, 1.0 ns, $U_o = 50$ m/s, Acoustic Interference Model

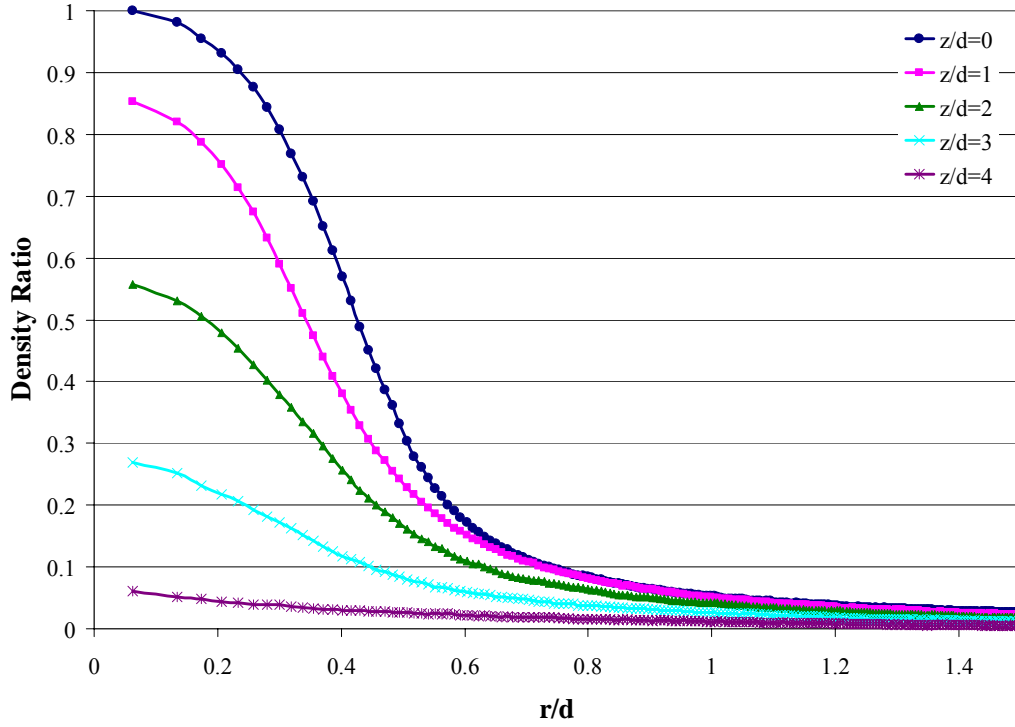


Figure 54. Radial Density Profile, 2.0 ns, $U_o = 50$ m/s, Acoustic Interference Model

Figures 55, 56, and 57 show development at $z/d = 0, 1$, and 2 respectively. Each chart shows higher density ratios at 2.0 ns showing a growing jet up to this time. Figure 58 shows the comparisons of the acoustic free and acoustic interference cases for the $U_o = 50$ m/s case at 1.0 ns. These results match what is seen in the mass fraction charts. This case shows higher density ratios for the acoustic free case which is a departure from what is seen in the $U_o = 0$ m/s case.

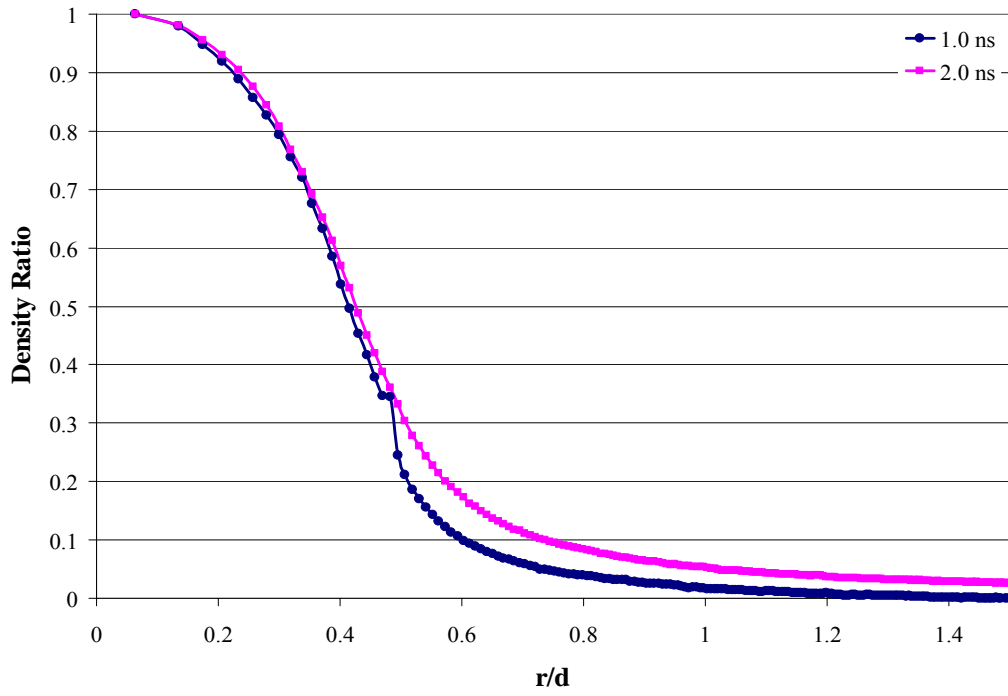


Figure 55. Radial Density Profile, $z/d=0$, $U_o = 50$ m/s, Acoustic Interference Model

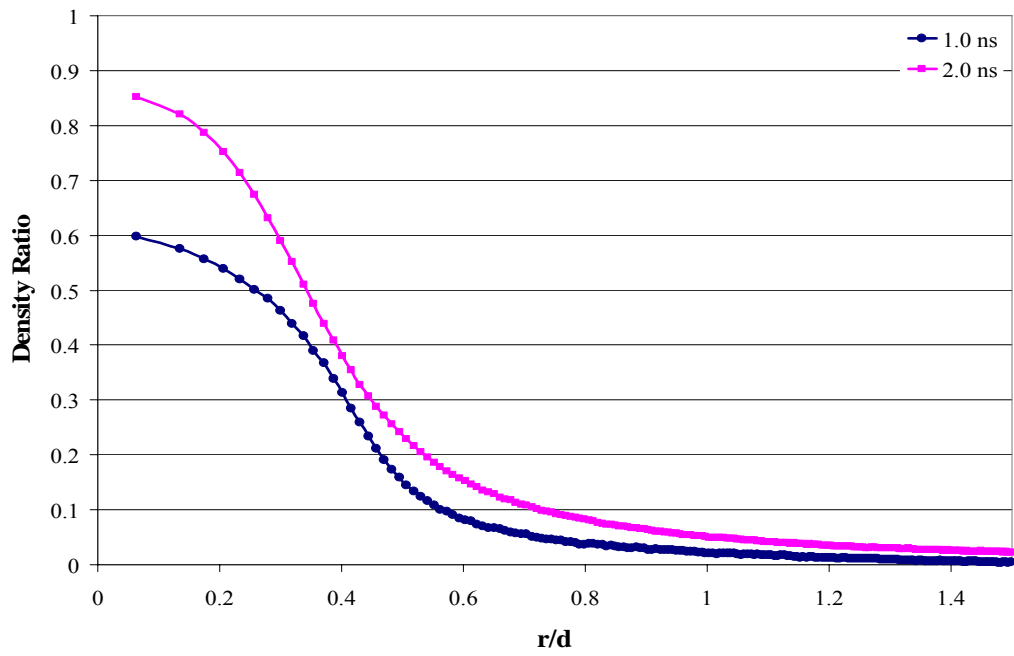


Figure 56. Radial Density Profile, $z/d=1$, $U_o = 50$ m/s, Acoustic Interference Model

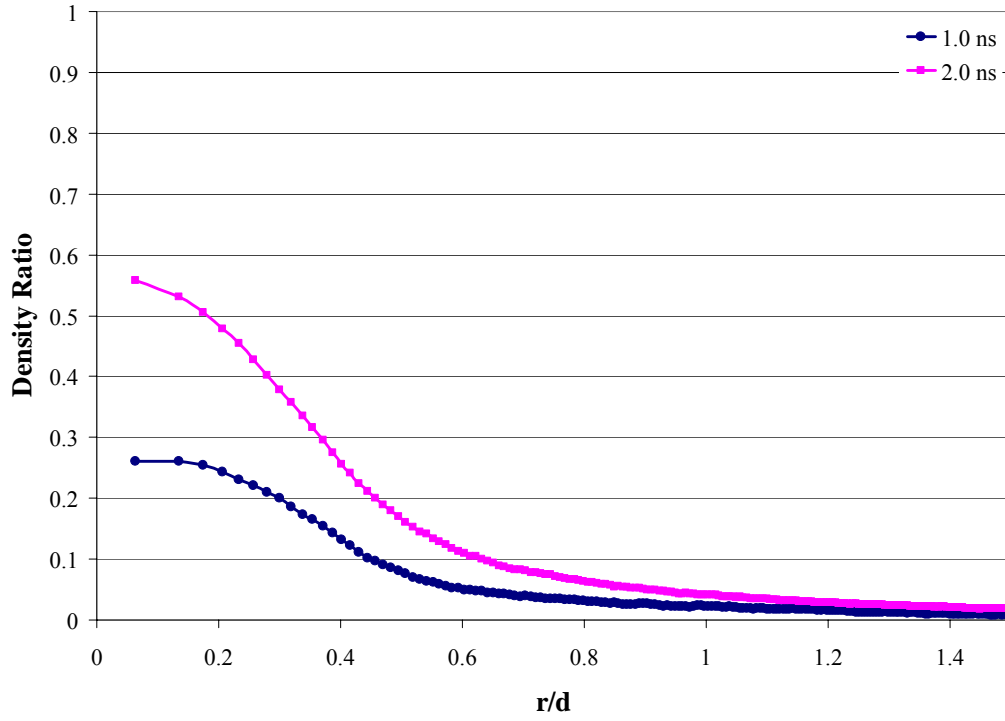


Figure 57. Radial Density Profile, $z/d=2$, $U_o = 50$ m/s, Acoustic Interference Model

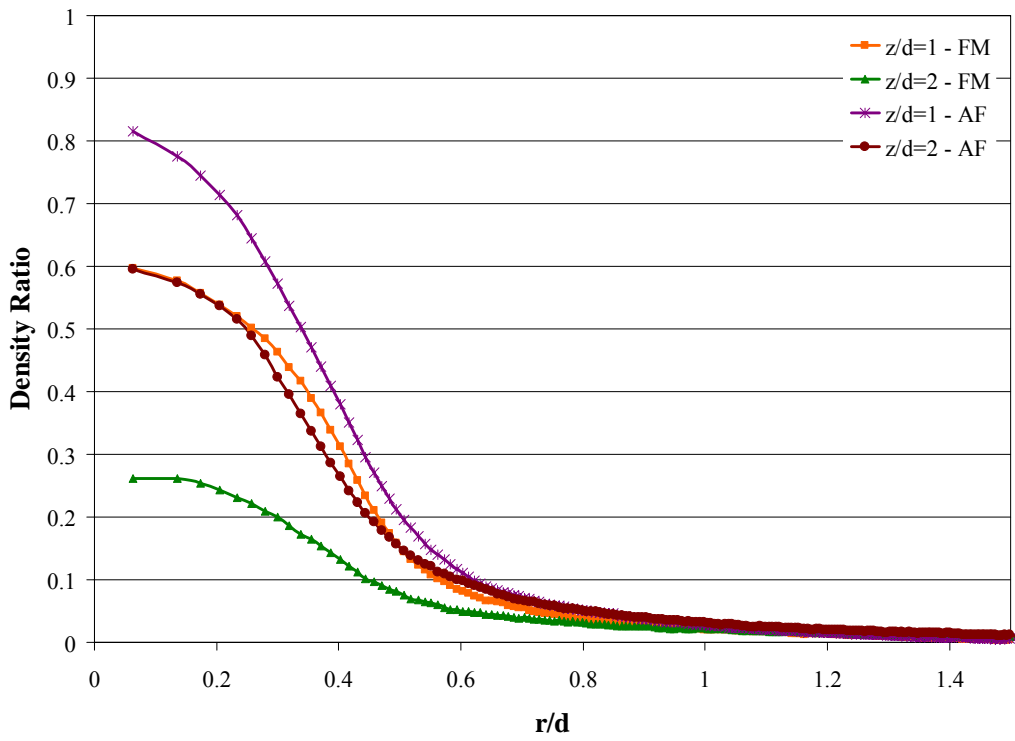


Figure 58. Radial Density Profile Comparison, $U_o = 50$ m/s, 1.0 ns, Acoustic Free (AF) Model and Acoustic Interference Model

For the velocity ratio $U_o/U_i = 6$, there are similar results. The density ratio profiles for the acoustic free case seen in Figures 59 to 64 and the acoustic interference models in Figures 65 to 70 seem to follow the same density progression seen in the $U_o = 0$ m/s cases. The acoustic free density ratios for $U_o = 300$ m/s are slightly higher than those for the $U_o = 0$ m/s cases. The density ratios for the acoustic interference model also favors the $U_o = 300$ m/s cases, as these cases see higher density ratios than the $U_o = 0$ m/s cases. For the $U_o = 0$ m/s case, the acoustic interference jet is wider than the acoustic free jet and the data receives some validation from Figure 51. Figures 71, 72, and 73 show the acoustic interference jet for $U_o = 300$ m/s is not as wide as the acoustic free jet. The acoustic free jet has a slightly wider radial spread than does the acoustic interference jet. No difference is apparent in the axial issuance of the jet into the chamber for either model. The radial data is not a great departure from previous experimentation. The acoustic free cases present a slightly wider jet in the radial axis with little difference in the axial length of the jet. Figure 74 shows shadowgraphs from the experimental research operating at higher chamber pressures and higher velocity ratios and small differences can be seen in the radial width of the acoustic free and acoustic interference jets while differences in the axial lengths of the jets is fairly indiscernible.

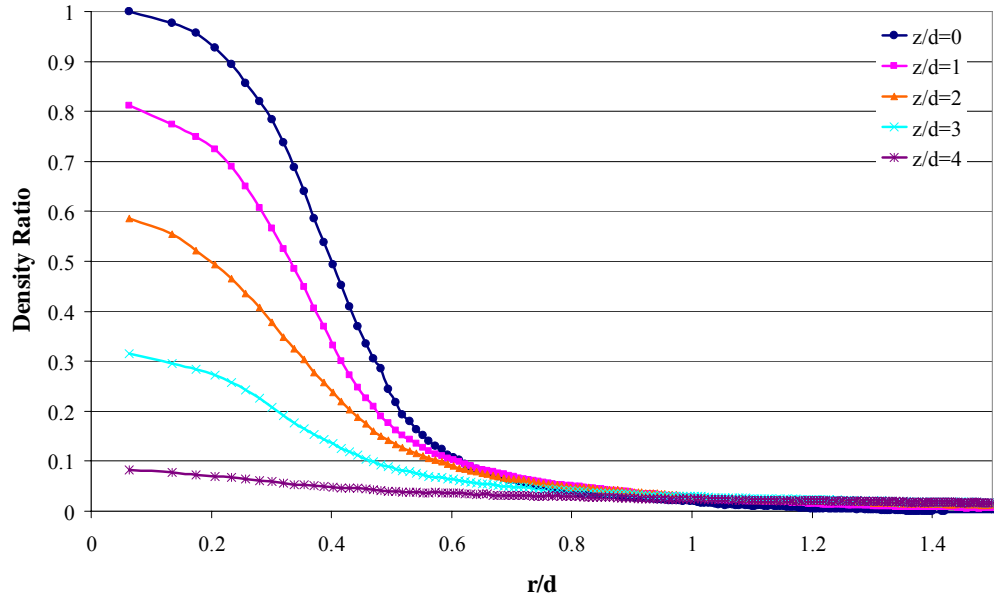


Figure 59. Radial Density Profile at 1.0 ns, $U_0 = 300$ m/s, Acoustic Free Model

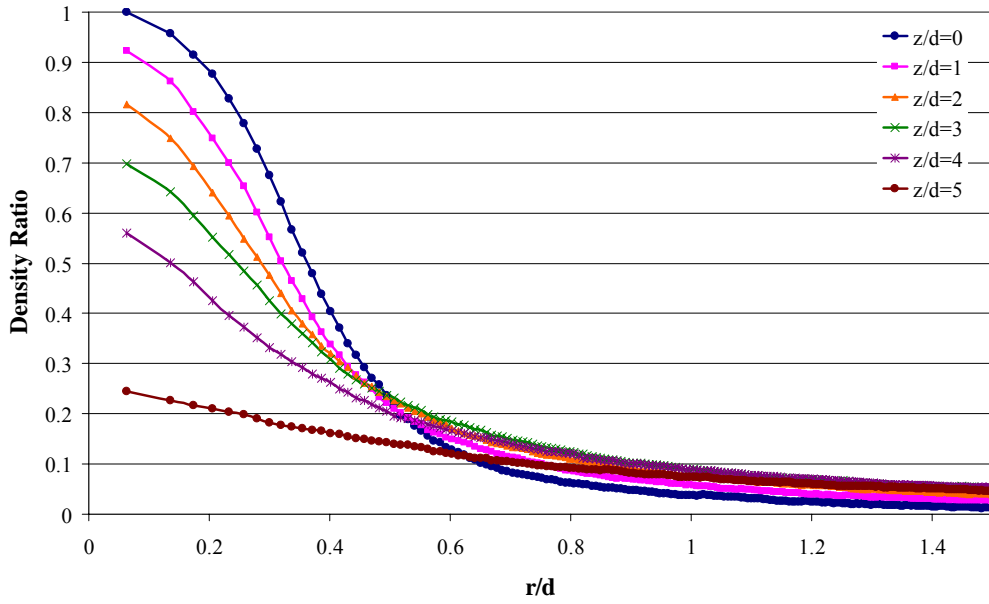


Figure 60. Radial Density Profile at 2.0 ns, $U_0 = 300$ m/s, Acoustic Free Model

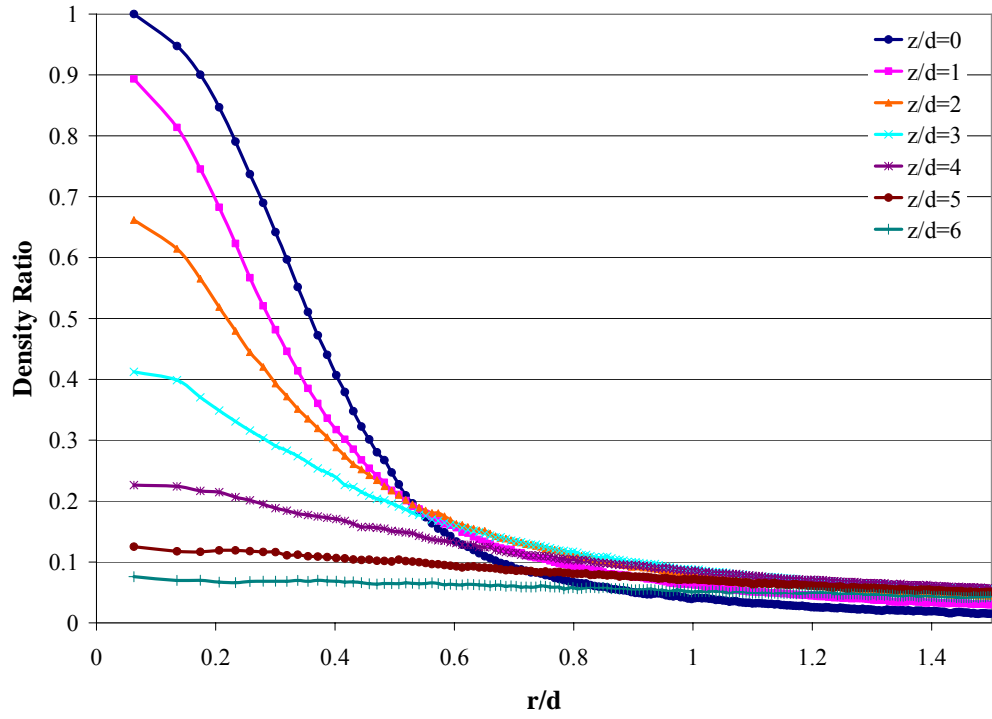


Figure 61. Radial Density Profile at 3.0 ns, $U_0 = 300$ m/s, Acoustic Free Model

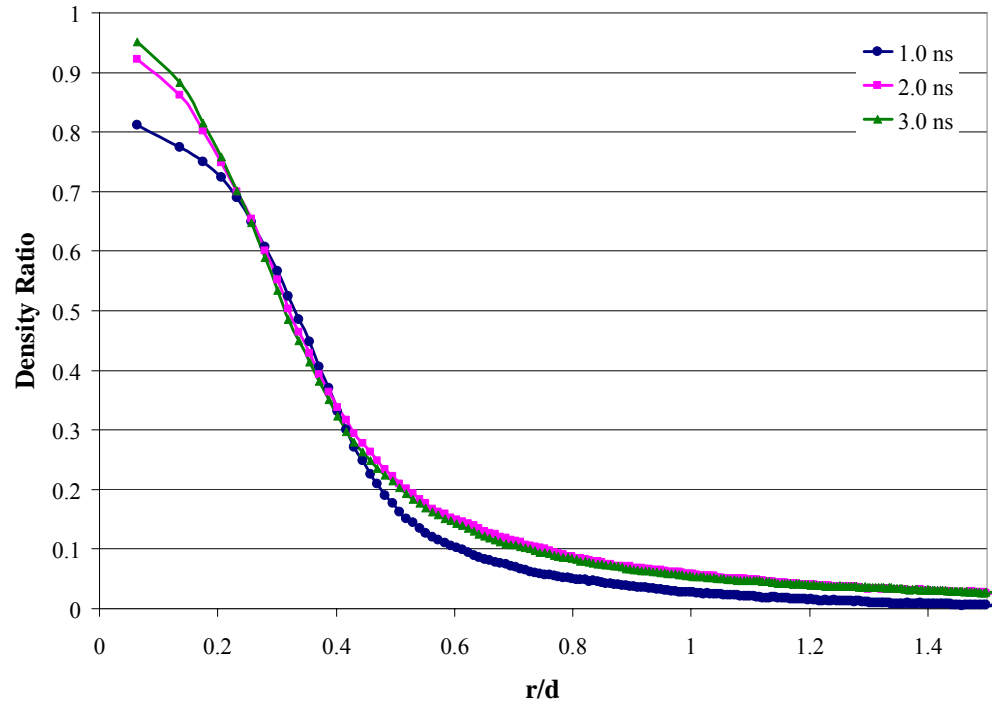


Figure 62. Radial Density Profile at $z/d=1$, $U_0=300$ m/s, Acoustic Free Case

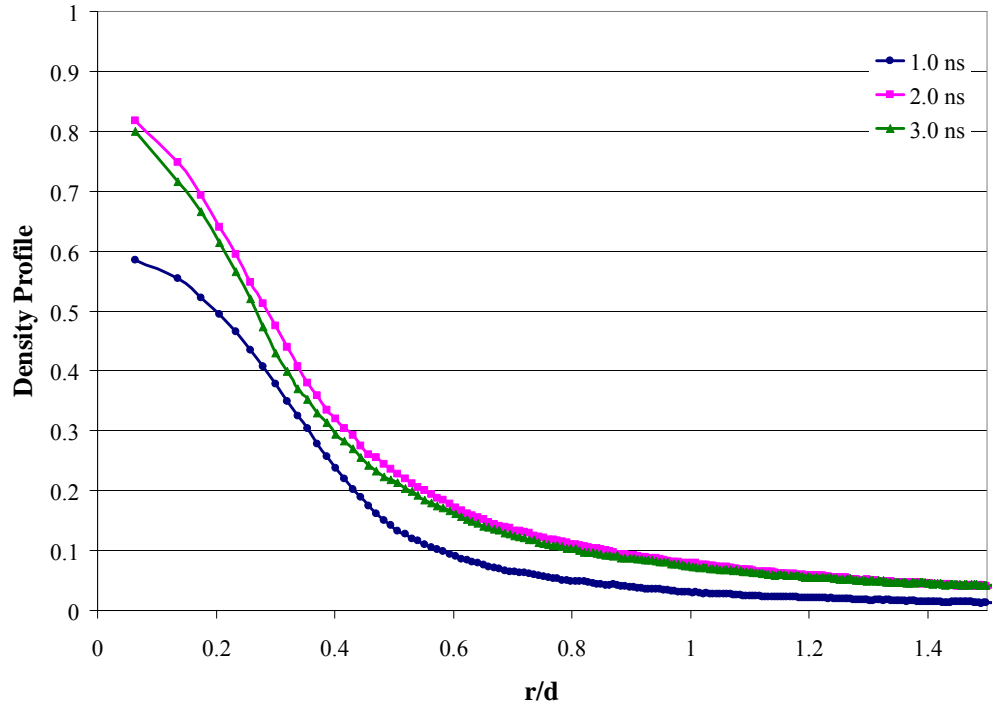


Figure 63. Radial Density Profile at $z/d=2$, $U_o=300$ m/s, Acoustic Free Case

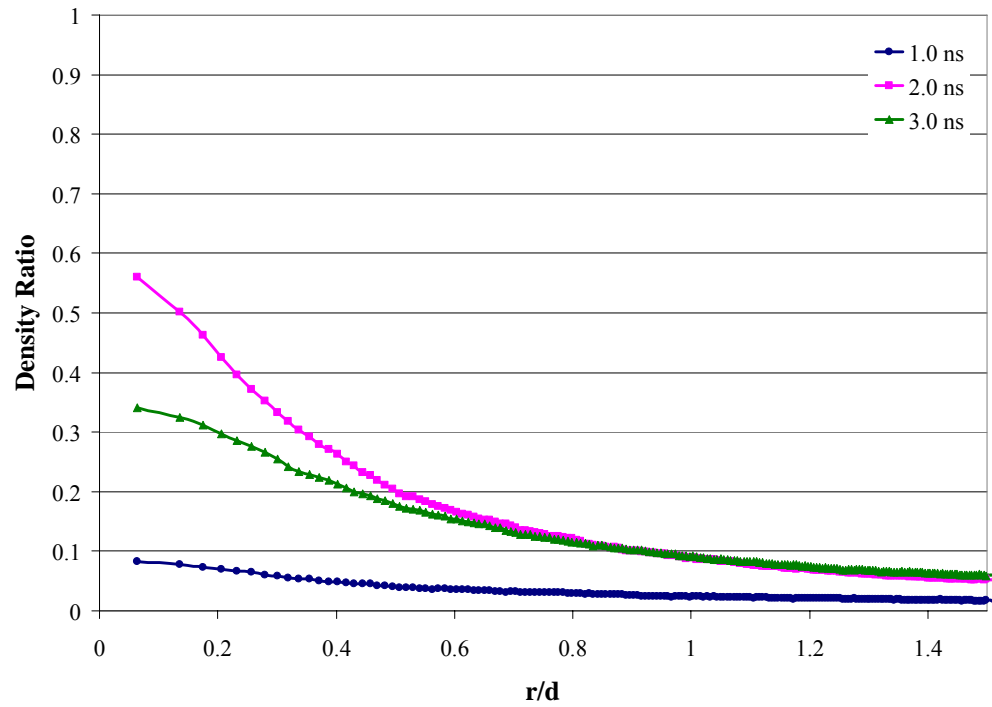


Figure 64. Radial Density Profile at $z/d=4$, $U_o=300$ m/s, Acoustic Free Case

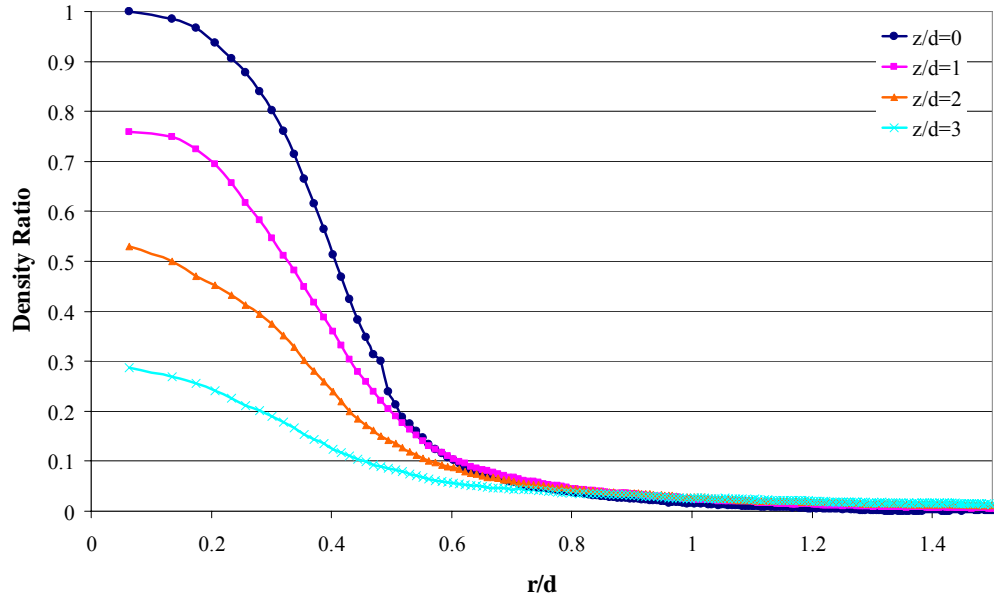


Figure 65. Radial Density Profile at 1.0 ns, $U_0 = 300$ m/s, Acoustic Interference Model

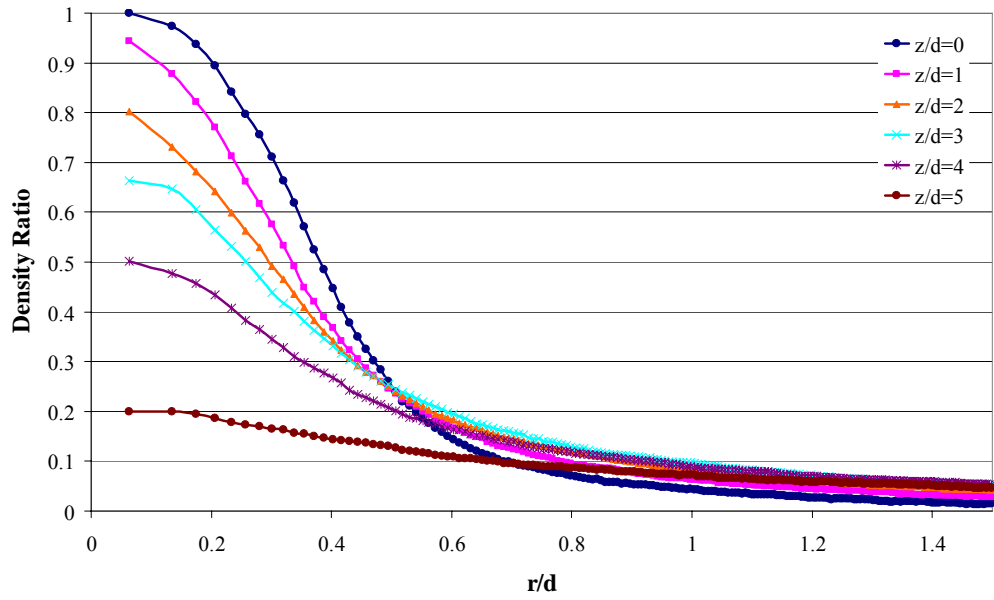


Figure 66. Radial Density Profile at 2.0 ns, $U_0 = 300$ m/s, Acoustic Interference Model

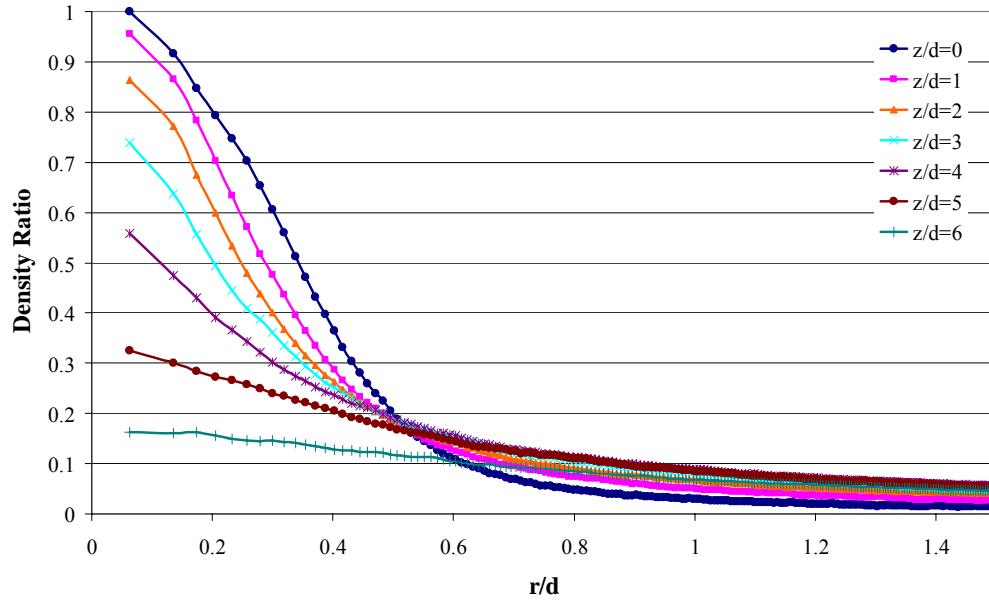


Figure 67. Radial Density Profile at 3.0 ns, $U_o = 300$ m/s, Acoustic Interference Model

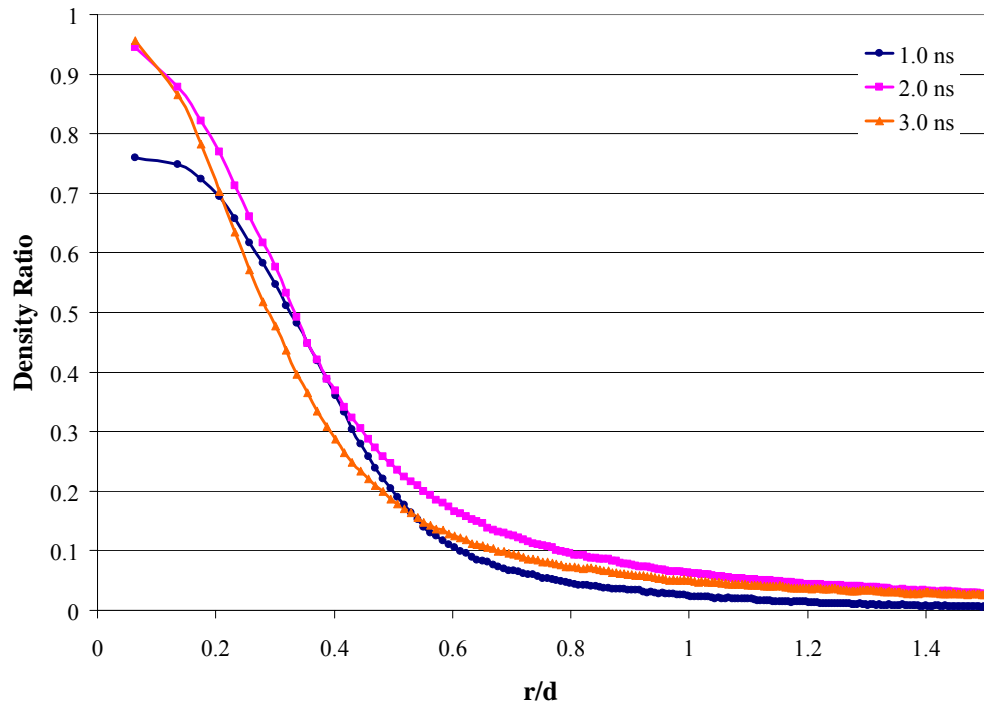


Figure 68. Radial Density Profile at $z/d=1$, $U_o=300$ m/s, Acoustic Interference Model

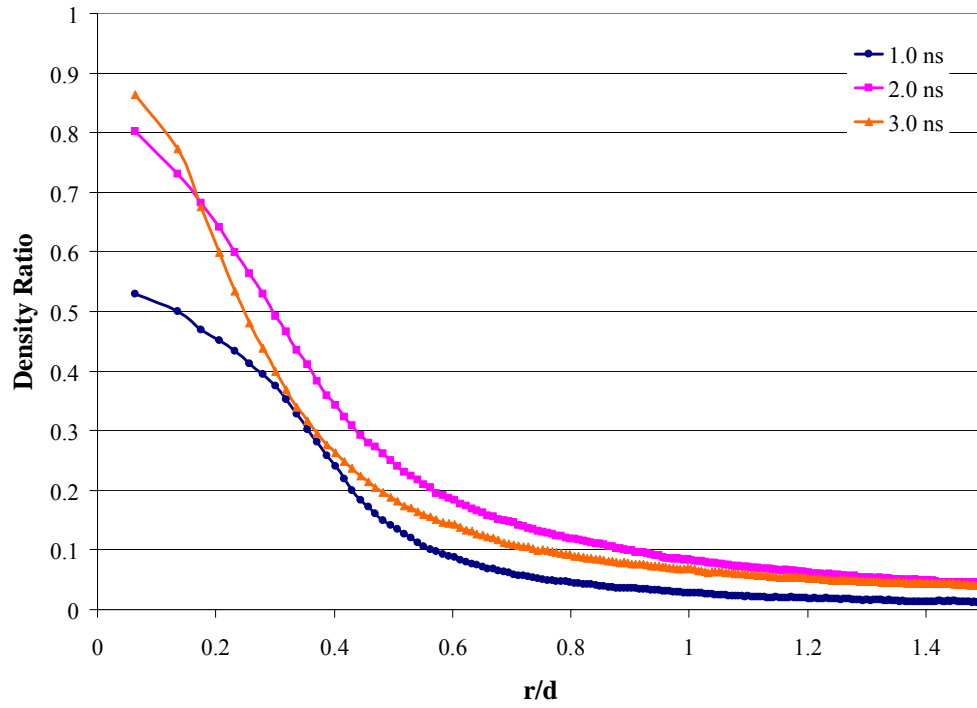


Figure 69. Radial Density Profile at $z/d=2$, $U_o=300$ m/s, Acoustic Interference Model

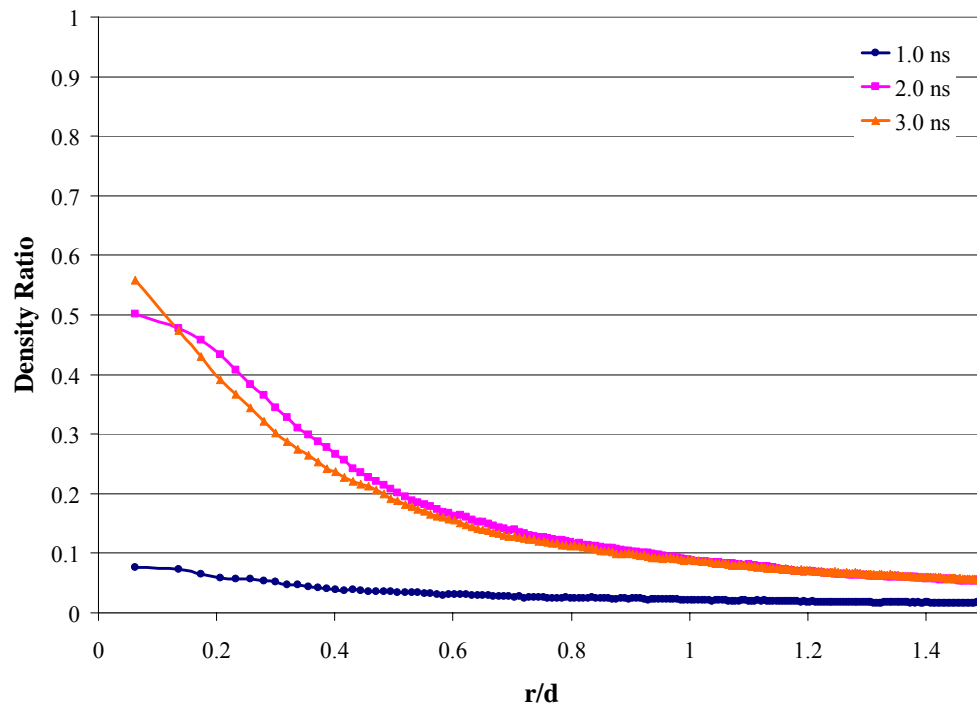


Figure 70. Radial Density Profile at $z/d=4$, $U_o=300$ m/s, Acoustic Interference Model

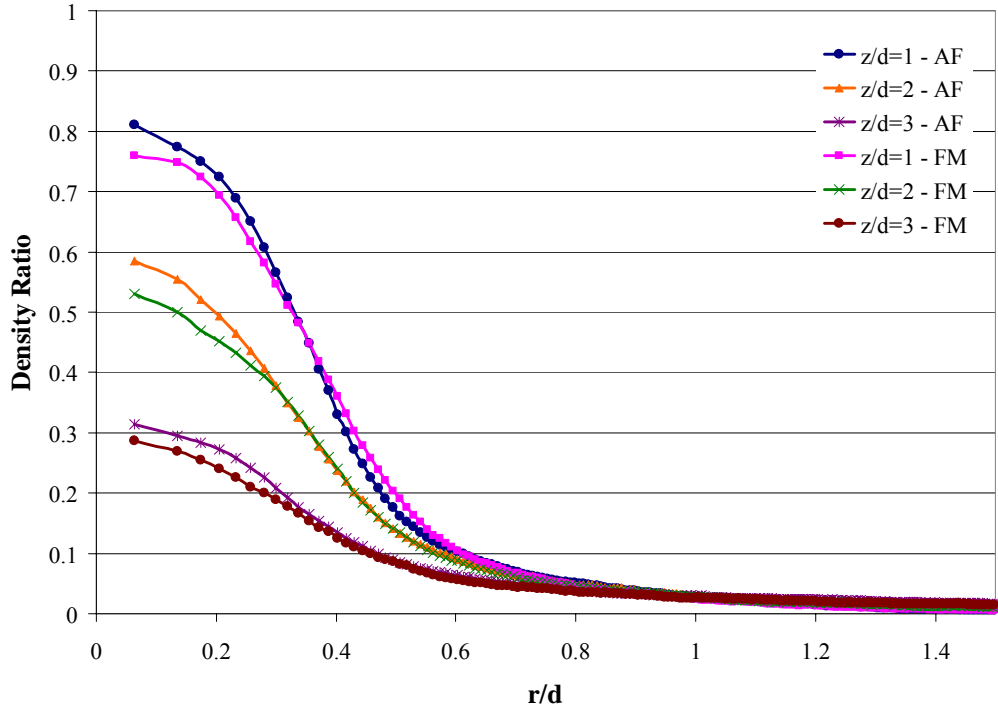


Figure 71. Radial Density Comparison, $U_0 = 300$ m/s, 1.0 ns, Acoustic Free (AF) Model and Acoustic Interference Model

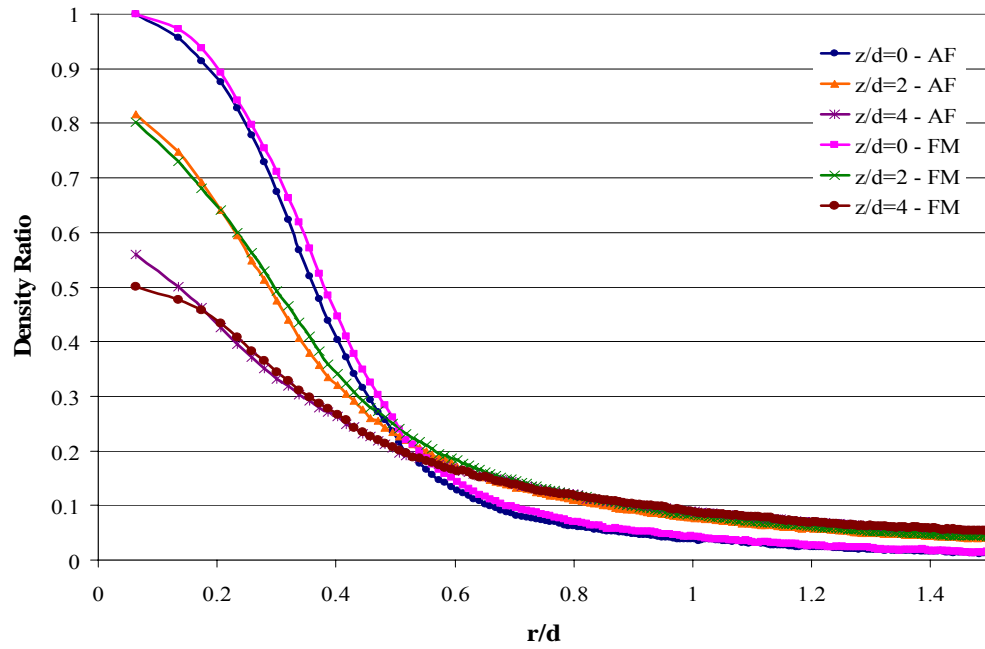


Figure 72. Radial Density Comparison, $U_0 = 300$ m/s, 2.0 ns, Acoustic Free (AF) Model and Acoustic Interference Model

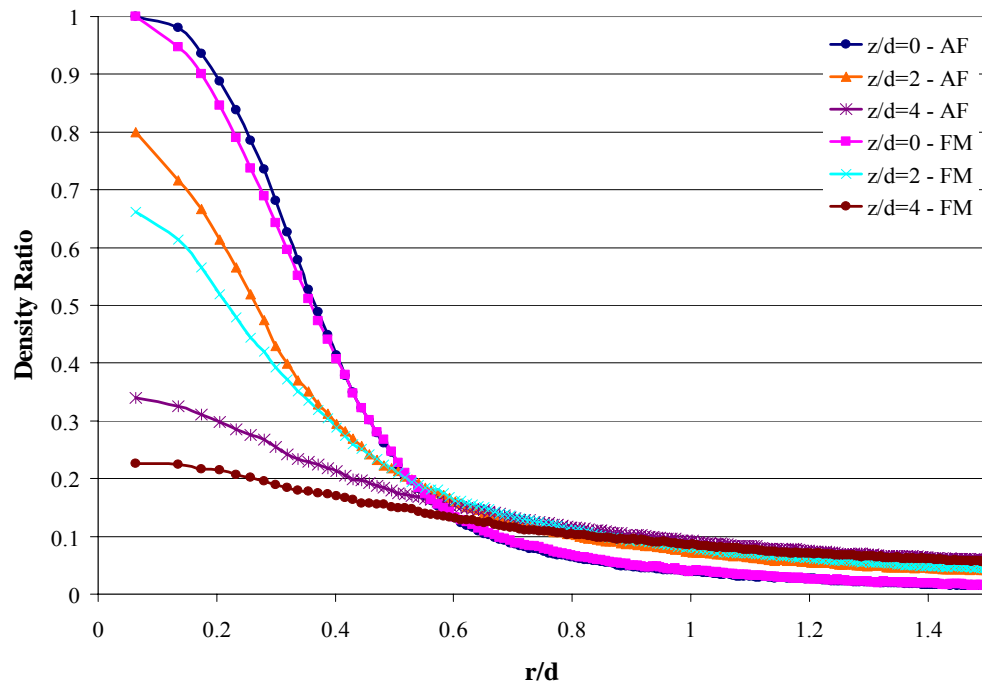


Figure 73. Radial Density Comparison, $U_o = 300$ m/s, 3.0 ns, Acoustic Free (AF) Model and Acoustic Interference Model

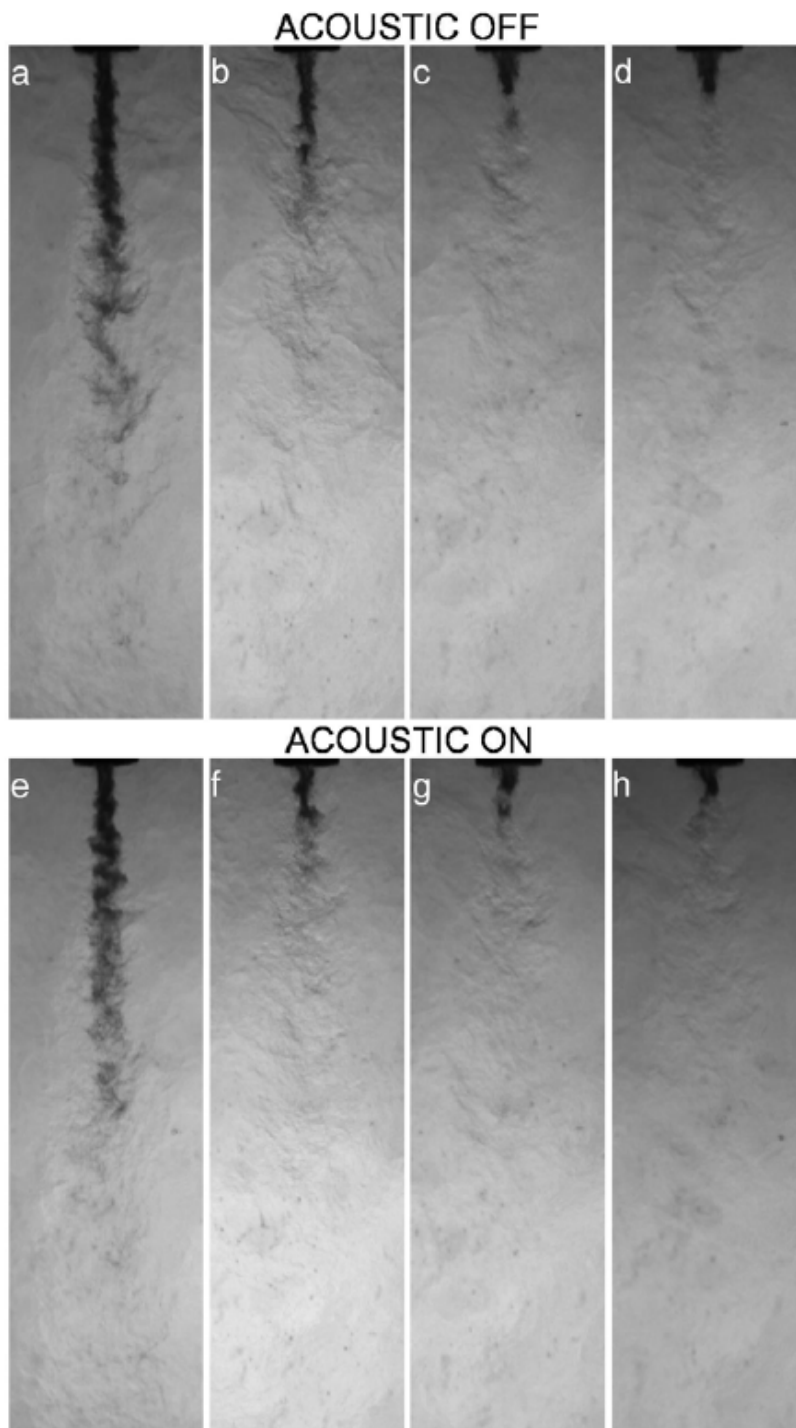


Figure 74. Shadowgraph images of coaxial jet at nearcritical chamber pressure ($\sim 3.5\text{MPa}$) and at the high outer-jet temperature ($\sim 190\text{K}$) corresponding to cases 5–8 ($U_o/U_i = \sim 2.5, \sim 7, \sim 11$, and ~ 13.5). The acoustic driver is off for images in the top row and on for the bottom row at $\sim 3\text{ KHz}$. The velocity ratio increases from left to right. (Davis, 2006:96)

V. Conclusions and Recommendations

Conclusions

The molecular dynamic simulation tool used for this research initially studied single jet injector flow. This research required changes be made to the simulation code. Coaxial flow and acoustic interference were incorporated into the code. The new code has provided simulation data for single and coaxial jet flows, with and without acoustic interference comparable to previous experimental data. Multiple velocity ratios were examined and their results were compared with previous experimental data.

The original coaxial geometry was modified to provide geometry able to run within the present computer resource limitations. The coaxial geometry provided some valuable data, but there were some trends seen in velocity and density profiles that suggest the geometry may not be ideal. The velocity profiles showed acceleration in the coaxial inner and outer tube as the flow began. The coaxial velocity profiles did not match the theoretical velocity curves. The outer velocity curves for acoustic free and acoustic interference models did have the same shape, pointing to the coaxial tube geometry as the reason for the velocity data curves obtained. Acceleration was also seen in the single jet case when the acoustic interference was applied. The effects acoustic interference exert on the simulated coaxial jet are most pronounced in the mass fraction charts, a strong indication of mixing.

Of the two acoustic interference models available in the molecular dynamic tool, only the force model provided expected results. The discrete particle model could not provide any interference due to the size of the simulations. The model can not be truly validated

unless simulation size is increased in future efforts. Each of the three outer to inner jet velocity ratios studied provided initial data used to validate the molecular dynamic simulations. The single jet case showed less mixing when acoustic interference was present. The acoustic interference case for the single jet trailed behind the mixing of the acoustic free case. The results for the cases with a coaxial component showed improved mixing when the acoustic interference was applied. Chamber mixing for acoustic interference models exceeded those of the acoustic free case. Compared to previous experimental data, there was correlation showing qualitative agreement. The radial density profiles showed results that matched experimental data. Density curves for acoustic interference cases showed less steep declines when compared to acoustic free cases. The research is in the early stages and shows progress in the goal of providing simulations modeling desired coaxial and acoustic effects.

Recommendations for Future Research

Future endeavors into molecular dynamic simulation with the existing code should lead to increased testing of the coaxial jet with acoustic effects. More variations to the coaxial jet ratio of D_o/D_i , as well as to the velocity ratios for the outer and inner jets need to be considered. Presently, the simulation takes advantage of the simplicity of modeling argon and nitrogen. The next step should include the simulation of more complex fluids through the injectors. As the simulations become more involved, the required computing capability will increase. The simulation runs for this research pushed the computing envelope and required modifications in order to be completed successfully. The simulation code will have to be modified to create an environment maximizing parallel

computing efficiency. Simplified calculation algorithms may also aid in decreasing calculation times for simulations. The use of shared memory machines will reduce the wall run times by 50% using the current code.

The accelerations out of the tube into the chamber are a nano-hydrodynamic effect coupled with the mass addition subroutine in the code. There is a net pressure caused by the size of the tube. These problems must be addressed in future code modifications.

Possible random acoustic interference along with mechanics to deal with possible acoustic reflections from chamber walls could add much to the value of the molecular dynamic code.

Bibliography

1. Allen, M.P. and D.J. Tildesley. *Computer Simulation of Liquid*. New York: Oxford University Press., 1987
2. Andersen, Hans C. "Rattle: A "Velocity" Version of the Shake Algorithm for Molecular Dynamics Calculations," *Journal of Computational Physics*, 52: 24-34 (1983)
3. Au, H. and N.W.M Ko. "Coaxial Jets of Different Mean Velocity Ratios, Part 2," *Journal of Sound and Vibration*, 116: 427-443 (1987)
4. Branam, Richard D. *Molecular Dynamics Simulation of Supercritical Fluids*. PhD. Dissertation. The Pennsylvania State University, University Park PA, August 2005
5. Branam, R., G. Schneider, J. Telaar, and W. Mayer. *Length Scales in Cryogenic Injection at Supercritical Pressure*. *Experiments in Fluids*, 33:22-428 (2002)
6. Champagne, F. H. and I. J. Wygnanski. "An Experimental Investigation of Coaxial Turbulent Jet," *Int. Journal of Heat Mass Transfer*, 14: 1445-1464 (1971)
7. Danforth-Hanford, Amanda, P. D. O'Connor, L. N. Long, and J. B. Anderson. *Molecular Relaxation Simulations in Nonlinear Acoustics using Direct Simulation Monte Carlo*. 17th International Symposium of Nonlinear Acoustics, State College, PA, July 2005.
8. Danforth, Amanda and Lyle N. Long. "Nonlinear acoustic simulations using direct simulation Monte Carlo," *Journal of Acoustic Society of America*, 116: 1948-1955 (2004)
9. Davis, Dustin Wayne. *On the Behavior of a Shear-Coaxial Jet, Spanning Sub- to Supercritical Pressures, with and without an Externally Imposed Transverse Acoustic Field*. PhD. Dissertation. The Pennsylvania State University, University Park PA, May 2006
10. Davis, Dustin W. and Bruce Chehroudi. *Measurements in an Acoustically-Driven Coaxial Jet under Sub-, Near, and Supercritical Conditions*. Engineering Research Consultants, Inc., Edwards AFB CA,
11. Davis, Dustin and Bruce Chehroudi. *The Effects of Pressure and Acoustic Field on a Cryogenic Coaxial Jet*. Engineering Research Consultants, Inc., Edwards AFB CA,

12. Haile, J.M. *Molecular Dynamics Simulation: Elementary Methods*. John Wiley & Sons, Inc., 1992
13. Hadjiconstantinou, Nicolas G. and Alejandro L. Garcia. "Molecular simulations of sound wave propagation in simple gases," *Physics of Fluids*, 13: 1040-1046 (2001)
14. Karniadakis, George, Ali Beskok, Nayaran Aluru, *Microflows and Nanoflows: Fundamentals and Simulation.*, Springer Science+Business Media, Inc., 2005
15. Ko, N. W. M. and H Au. "Coaxial Jets of Different Mean Velocity Ratios," *Journal of Sound and Vibration*, 100: 211-232 (1985)
16. Ludwig, A. "Molecular Model and Basic Physical Variables" Excerpt from unpublished article. n. pag.
http://www.silcom.com/~aludwig/Physics/Main/Molecular_model.html
17. Ludwig, A. "Basic Differential Equations" Excerpt from unpublished article. n. pag. http://www.silcom.com/~aludwig/Physics/Main/Differential_equations.html
18. Ludwig, A. "Acoustic Equations" Excerpt from unpublished article. n. pag.
http://www.silcom.com/~aludwig/Physics/Main/Acoustic_equations.html
19. Ludwig, A. "Plane Waves" Excerpt from unpublished article. n. pag.
http://www.silcom.com/~aludwig/Physics/Main/Plane_waves.html
20. Ludwig, A. "Coupling Power out of a Plane Wave" Excerpt from unpublished article. n. pag.
http://www.silcom.com/~aludwig/Physics/Main/Coupling_power.html
21. Mayer, W., J. Tellar, R. Branam, and G. Schneider. *Characterization of Cryogenic Injection at Supercritical Pressure*. AIAA 2001-3275, 37th AIAA/ASME/ASEE Joint Propulsion Conference and Exhibit, Salt Lake City, UT, July 2001
22. Morton, B.R. "Coaxial Turbulent Jets," *International Journal of Heat Mass Transfer*, 5: 955-965 (1962)
23. Rapaport, D.C., *The Art of Molecular Dynamics Simulation*. Cambridge University Press, 1995
24. Schetz, J. A., *Injection and Mixing in Turbulent Flow*. New York: American Institute of Aeronautics and Astronautics, 1980.

25. Strakey, P.A., D.G. Talley and J.J. Hutt. "Mixing Characteristics of Coaxial Injectors at High Gas/Liquid Momentum Ratios," *Journal of Propulsion and Power*, 17: 402-410 (2001)
26. Villiermaux, Emmanuel. "Mixing and Spray Formation in Coaxial Jets," *Journal of Propulsion and Power*, 14: 807-816 (1998)
27. White, Frank M., *Viscous Fluid Flow.*, McGraw-Hill, Inc., 1974
28. Wilcox, David C., *Turbulent Modeling for CFD.*, DCW Industries., 2006
29. Wochner, Mark S., Anthony A. Atchley and Victor W. Sparrow. "Numerical simulation of finite amplitude wave propagation in air using a realistic atmospheric absorption model," *Journal of Acoustic Society of America*, 118: 2891-2898 (2005)
30. "Decibel Scales: Sound Pressure Level and Sound Intensity Level" Excerpt from unpublished article. n. pag. http://physics.mtsu.edu/~wmr/log_3.htm

Vita

Captain Jermaine Sailsman graduated from Westtown High School in Westtown, Pennsylvania. He entered undergraduate studies at the Georgia Institute of Technology in Atlanta, Georgia where he graduated with a Bachelor of Science degree in Aerospace Engineering in May 2000. He received his commissioned through Officer Training School in Montgomery, Alabama in August 2002.

His first assignment was as an aircraft data engineer at the National Air and Space Intelligence Center at Wright-Patterson AFB. In August 2005, he completed his Master in Business Administration from Wright State University with a dual concentration in Marketing and International Business. In August 2005, he entered the Graduate School of Engineering and Management, Air Force Institute of Technology. Upon graduation, he will be assigned to Air Force Research Lab, Kirtland AFB.

REPORT DOCUMENTATION PAGE				Form Approved OMB No. 074-0188	
<p>The public reporting burden for this collection of information is estimated to average 1 hour per response, including the time for reviewing instructions, searching existing data sources, gathering and maintaining the data needed, and completing and reviewing the collection of information. Send comments regarding this burden estimate or any other aspect of the collection of information, including suggestions for reducing this burden to Department of Defense, Washington Headquarters Services, Directorate for Information Operations and Reports (0704-0188), 1215 Jefferson Davis Highway, Suite 1204, Arlington, VA 22202-4302. Respondents should be aware that notwithstanding any other provision of law, no person shall be subject to a penalty for failing to comply with a collection of information if it does not display a currently valid OMB control number.</p> <p>PLEASE DO NOT RETURN YOUR FORM TO THE ABOVE ADDRESS.</p>					
1. REPORT DATE (DD-MM-YYYY) 22-03-2007		2. REPORT TYPE Master's Thesis		3. DATES COVERED (From – To) August 2005 – March 2007	
4. TITLE AND SUBTITLE Modeling Acoustic Effects on Shear Coaxial Jet Flow Utilizing Molecular Dynamic Simulation				5a. CONTRACT NUMBER	
				5b. GRANT NUMBER	
				5c. PROGRAM ELEMENT NUMBER	
6. AUTHOR(S) Sailsman, Jermaine S., Captain, USAF				5d. PROJECT NUMBER	
				5e. TASK NUMBER	
				5f. WORK UNIT NUMBER	
7. PERFORMING ORGANIZATION NAMES(S) AND ADDRESS(S) Air Force Institute of Technology Graduate School of Engineering and Management (AFIT/EN) 2950 Hobson Way WPAFB OH 45433-7765				8. PERFORMING ORGANIZATION REPORT NUMBER AFIT/GA/ENY/07-M16	
9. SPONSORING/MONITORING AGENCY NAME(S) AND ADDRESS(ES) AFRL/AFOSR Attn: Dr. Mitat Birkan 875 North Randolph Street Arlington, VA 22203 Commercial:703-696-7234				10. SPONSOR/MONITOR'S ACRONYM(S)	
				11. SPONSOR/MONITOR'S REPORT NUMBER(S)	
12. DISTRIBUTION/AVAILABILITY STATEMENT APPROVED FOR PUBLIC RELEASE; DISTRIBUTION UNLIMITED.					
13. SUPPLEMENTARY NOTES					
14. ABSTRACT The purpose of this research is to determine if acoustical effects on a coaxial shear injection jet flow can be modeled through the use of molecular dynamic simulation. Molecular dynamic simulations model flows as a group of interacting particles. The flow in this research was simulated using nitrogen molecules. The initial task involved achieving effective geometry for a simulated coaxial jet. The coaxial jet geometry was driven by the desire for simulations to operate in the continuum regime, which requires very low Knudsen numbers. Three outer to inner jet ratios of 0.0, 1.0, and 6.0 were examined with the inner jet velocity maintained constant at 50 m/s. Velocity profiles in the coaxial component need to be controlled in order to validate the continuum flow. Acoustic interference is introduced into the simulation, and mixing and density profiles provide valuable information into the how the flow is affected by the acoustic interference. Radial density profiles also provide information about the shape the jet with and without acoustic interference as it exits the injector. The affects of acoustic interference for most cases showed good agreement with the previous experimental data. Results showed good validation of the simulation and warrants more in-depth study.					
15. SUBJECT TERMS Acoustics, Fluid Flow, Molecular Dynamics, Coaxial, Interference					
16. SECURITY CLASSIFICATION OF:			17. LIMITATION OF ABSTRACT	18. NUMBER OF PAGES	19a. NAME OF RESPONSIBLE PERSON
a. REPORT	b. ABSTRACT	c. THIS PAGE			Richard D. Branam, Maj, USAF
U	U	U	UU	113	19b. TELEPHONE NUMBER (Include area code) (937) 255-3636, ext 7485 (Richard.Branam@afit.edu)

Standard Form 298 (Rev. 8-98)